Characterization of Formability and Friction during Hot Stamping of Al-Si Coated Press Hardened Steel

by
Ruijian He

A thesis
presented to the University of Waterloo
in fulfilment of the
thesis requirement for the degree of
Master of Applied Science
in
Mechanical and Mechatronics Engineering

Waterloo, Ontario, Canada, 2023

Author's Declaration

I hereby declare that I am the sole author of this thesis. This is a true copy of the thesis, including any required final revisions, as accepted by my examiners.

I understand that my thesis may be made electronically available to the public.

Abstract

This thesis investigates the friction and formability characteristics of Al-Si coated press hardened steels (PHS) during direct hot stamping. The PHS grades examined were PHS1800 and PHS1500, with nominal ultimate tensile strengths after hot stamping of 1800 and 1500 MPa, respectively. Both grades were received with a coating weight of 150 g/m^2, designated PHS1800-AS150 and PHS1500-AS150, while a coating weight of 80 g/m^2 was also tested for the PHS1500, designated PHS1500-AS80. Testing was done under conditions representative of hot stamping.

Friction characterization using the twist compression test (TCT) was performed considering sliding speeds in the range 10 to 38 mm/s and contact pressures of 5 to 30 MPa. Sliding speed did not have a significant impact on the coefficient of friction (CoF). The average CoF of PHS1800 increased from 0.3 to 0.4 over the range of contact pressure considered. At a constant sliding speed of 20 mm/s and a contact pressure of 30 MPa, the PHS variants ranked in increasing order of average CoF were PHS1800 at 0.41, PHS1500-AS150 at 0.46, and PHS1500-AS80 at 0.48. The effect of tooling wear was examined by repeating ten friction tests using the same friction cup with new PHS specimens. No significant change in the tooling surface roughness and CoF was recorded for the limited number of repeat tests considered.

Formability characterization was performed using a hemispherical Nakazima punch, as well as flat Marciniak and Hybrid punches, which both employed a carrier blank. The Nakazima punch resulted in faster cooling at the center of the blanks (relative to the periphery) leading to failure

near the die entry radius under plane strain conditions for all sample geometries and lubrication conditions. The Marciniak and Hybrid cup tests avoided direct contact between the blank center and punch, resulting in central failures with linear strain paths spanning from uniaxial to equibiaxial strain conditions. All of the formability tests achieved necking limit strains with major strain values above 0.35.

In the Marciniak test, the PHS1500 exhibited higher limit strains than PHS1800 with both PHS1500 coating variants having similar limit strains. Among all PHS sample gage widths, the strain rate at the center increased while the cooling rate remained relatively constant and varied from 21.8 to 24.5°C/s.

LS-DYNA, a commercial finite element solver used to model the hot stamping process, predicted the deformation behavior of PHS1800 sample geometries in Nakazima, Marciniak, and Hybrid formability tests. The coupled thermomechanical model featured an isothermal heating phase followed by a formability phase with deformation and quenching occurring simultaneously to accurately represent hot stamping conditions. The numerical results predicted the necking locations and strain paths for each formability test, including the effect of local cooling rate.

Acknowledgements

I thank God for giving me the wisdom and courage to carry through my MASc degree.

I am profoundly grateful to Professor Michael Worswick for accepting me in his research group and for giving me the opportunity to work on this project. Back in December 2019, he generously let me choose my favorite project among several solid mechanics topics.

I am also highly thankful to my co-supervisor Professor Cliff Butcher who provided me with invaluable advice on problem solving engineering challenges encountered during my research. Without his support and knowledge on formability, this research would not have been able to progress so far.

The success of my tests would not have been possible without the tremendous support provided by our laboratory technicians. Eckhard Budziarek came up with the most effective thermal measurement solution for the twist compression test (TCT) by inserting the thermocouples directly into the sample thickness. He ensured my safety during each test day and always kept my experimental supplies plentiful. He was a pleasure to work with.

Ryan George taught me everything about how to operate the TCT apparatus for friction characterization and the forming press for formability characterization. He custom designed several control protocols to fit my testing needs. During formability tests, we worked as a well coordinated team to fit the high quantity of tests into the busy schedule of the forming press with great efficiency.

I would like to thank Dr. José Imbert for helping me with camera imaging and speckling, Neil Griffett for programming a custom TCT control protocol, Mark Kuntz for grinding all my TCT

cups, Tom Gawel for helping me locate various supplies, and Richard Gordon for providing me with mechanical design advice.

The post-docs and graduate students in Prof. Worswick's and Prof. Butcher's research group, in particular Dr. Pedram Samadian, have provided me with excellent advice on engineering techniques. Dr. Samadian's guidance on data processing, formability principles, and overall graduate school experience have made my engineering research journey much easier. His exceptional sense of humour is also a relief in challenging times.

Several foundational aspects of my research come from findings done by graduate student colleagues, such as Stan Lu, Sante DiCecco, Kaab Omer, and Claire Bourque. My research would not have been possible without their support and previous work.

It is thanks to my old friend Zi Meng, whom I consider as a brother, that this thesis exists and is not lost in a computer mishap. He was always there to support me no matter the time and situation.

In addition, this research would neither be possible without funding from this project's sponsors: Ford Motor Company, Magna International, Promatek Research Centre, Natural Sciences and Engineering Research Council of Canada (NSERC), and Ontario Contres of Excellence.

Dedication

For my family

Table of Contents

List of Figures

List of Tables

List of Abbreviations

BIW: body-in-white

AHSS: advanced high strength steel

PHS: press hardened steel

TCT: twist compression test

CoF: coefficient of friction

UHSS: ultra-high-strength steel

DIC: digital image correlation

FLC: forming limit curve

FLD: forming limit diagram

BCC: body-centered cubic

FCC: face-centered cubic

DAQ: data acquisition system

HER: hole expansion ratio

DOF: degree-of-freedom

VSG: virtual strain gage

FEM: finite element method

LBF: linear best fit

1. Background

The internal structure of an automobile, known as the body-in-white (BIW), must support loads on the vehicle and protect its occupants during a crash event [1]. It can be designed as a monocoque, in which all members are load-bearing components and integrated together, or as a body-on-frame, in which the frame is the primary load-bearing component, and the body is mounted on the frame. In a typical passenger car, the BIW consists of about 27% of the total mass as shown in Figure 1 [2]. A key strategy to reduce vehicle fuel consumption and emissions is to decrease the total mass of the vehicle while maintaining its mechanical properties [3]. Since the BIW is among the largest fractions of the total mass, along with the powertrain and chassis, a decrease in BIW mass is one of the most effective ways to improve fuel efficiency and reduce emissions.

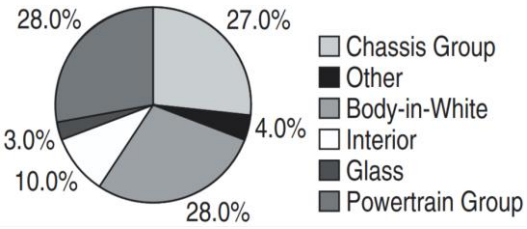

Figure 1: Typical mass distribution in a passenger car by Kelkar et al. [2]

Among mass-produced vehicles, steel and aluminum alloys are the main constituents of the BIW [4]. Advances in both types of materials have increased their strength-to-weight ratio, which allows vehicle lightweighting. The selected material for production must also provide sufficient

formability to create complex shapes and be economical to minimize production cost. Although aluminum alloys offer superior strength-to-weight ratio over steel, they are currently not as economically viable as steel for mass production according to Kelkar *et al.* [2] and illustrated in Figure 2. The purchase price for aluminum alloys can be five times more expensive than steel by weight. Springback is also a challenge in aluminum components due to their lower elastic modulus compared to steel [2].

Similar to aluminum alloys, cold formed advanced high strength steels (AHSS) can also feature high springback during the forming process [5]. Since an increase in strength generally coincides with a decrease in formability and increased springback, the applications for 980 MPa and higher strength steels become limited. These formability limitations of aluminum alloys and AHSS create a need for hot stamping of press-hardened steel (PHS).

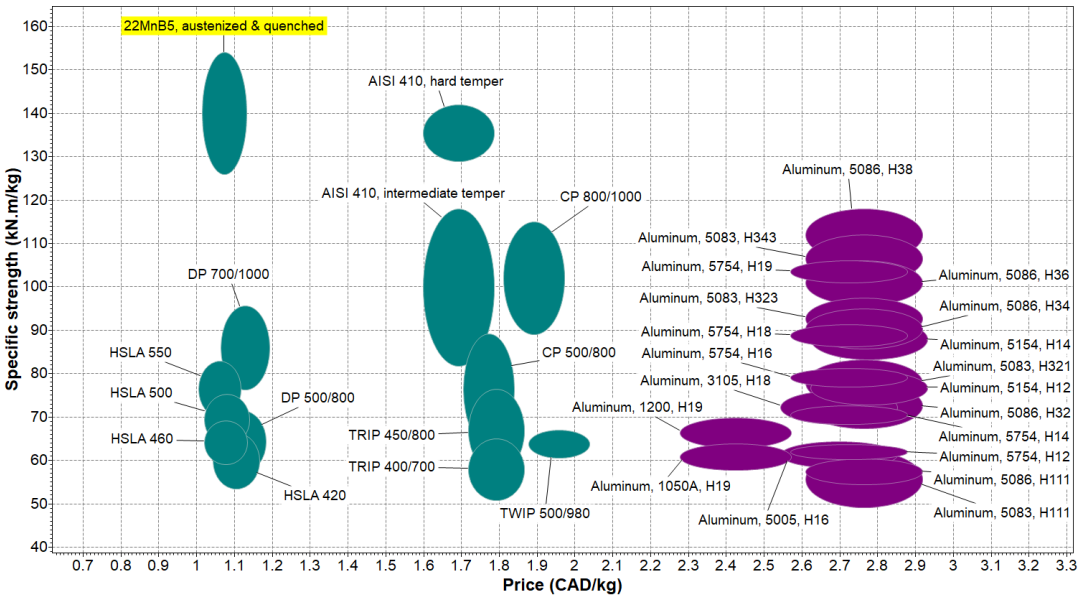

Figure 2: Cost of material strength for steel and aluminum alloys (Granta CES 2021)

1.1. Press Hardened Steel in Hot Stamping

To provide intrusion resistance in automotive applications, martensitic press hardened steels, such as 22MnB5 (herein designated PHS1500 with a nominal tensile strength of 1,500 MPa), were deployed extensively to reinforce structural components [6]. PHS1800 is a 37MnB5 ultra-high-strength steel (UHSS) that features a nominal tensile strength of 1,800 MPa after hot stamping [7]. This tensile strength was obtained through its fully martensitic microstructure after quenching with water-cooled tooling in the forming press, according to Naderi *et al.* [8]. PHS1500 and PHS1800 are used in anti-intrusion applications such as bumper beams, B-pillars, and door rings (Figure 3) [9], [10], [11].

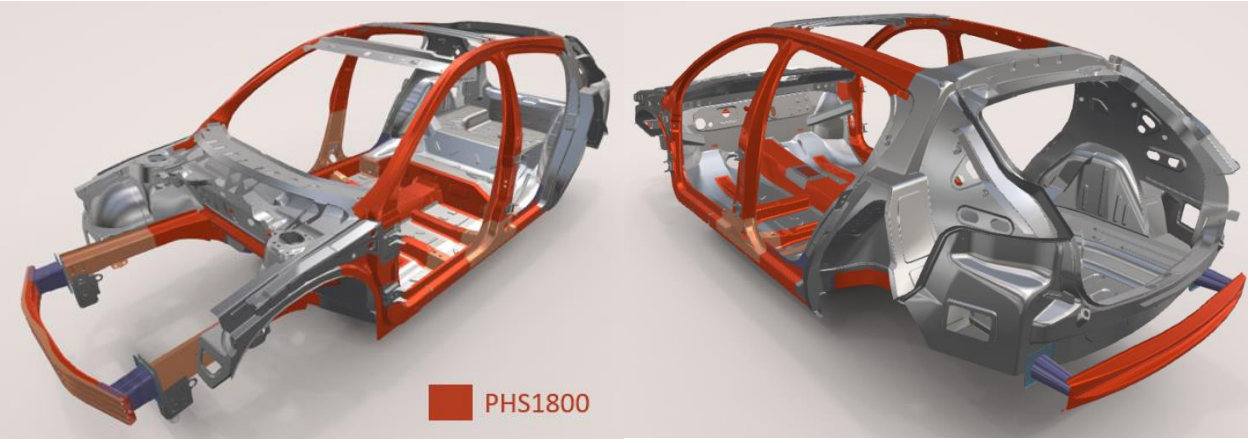

Figure 3: Typical body-in-white structure of a passenger car with PHS1800 deployed for crash-resistant components [10]

Although bainite and ferrite have better ductility than martensite, their ultimate tensile strengths are not as high as that of martensite [11]–[14]. Since PHS is intended for high-strength deformation resistant structural components, a fully martensitic microstructure is desired. The PHS1800 analyzed in this paper was coated with Al-Si at a concentration of 150 g/m^2. To support accurate

simulation of the hot stamping of this material, its friction characteristics must be accurately determined [15].

1.2. Direct Hot Stamping Process

In direct hot stamping, the room temperature blank is austenitized in a furnace then quickly transferred to the forming press for simultaneous forming and quenching to produce a martensitic microstructure (Figure 4) [7].

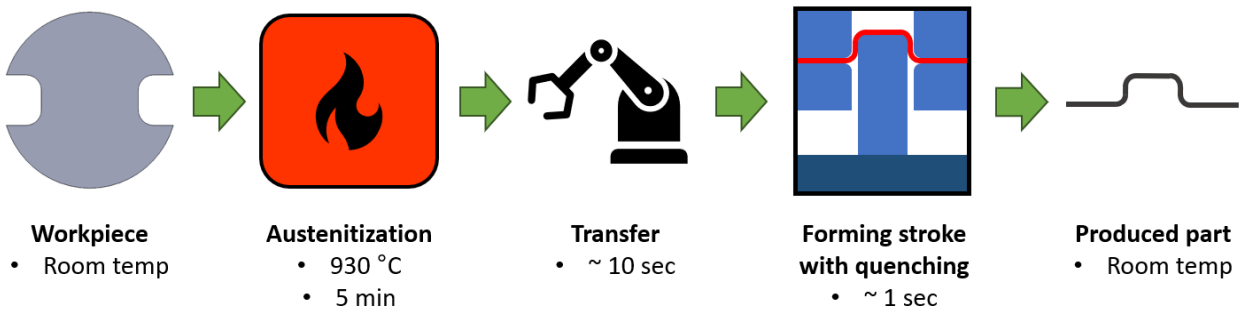

Figure 4: Typical direct hot stamping process in an industrial setting

As the temperature of PHS increases, its ductility increases due to its decreased flow stress as determined by Lu *et al.* [16]. This increased ductility enables the PHS to extensively deform without fracture and be shaped into complex geometries. When the PHS is in the temperature range between 650°C and 850°C, its high formability allows the formation of complex geometries in a single forming stroke [17]. A cooling rate above 27°C/s for PHS1500 from the austenitization temperature to below 400°C enabled the formation of a martensitic microstructure (Figure 5) to produce high tensile strength and stiffness, according to Merklein *et al.* [6], [18]. This high cooling

rate prevented formation of softer equilibrium phases in the microstructure, which resulted in the formation of martensite according to Hosford and Caddell [19]. Due to the forming at elevated temperature and the phase change from austenite to martensite, internal stresses are minimized within the component reducing springback compared to cold-formed parts [6], [20]–[22]. The minor springback in hot stamping is determined by the blank clamping force, clearance between the punch and the die, and die radius according to Xing *et al.* [23]. The direct hot stamping process incorporates these advantages to produce UHSS sheet metal parts.

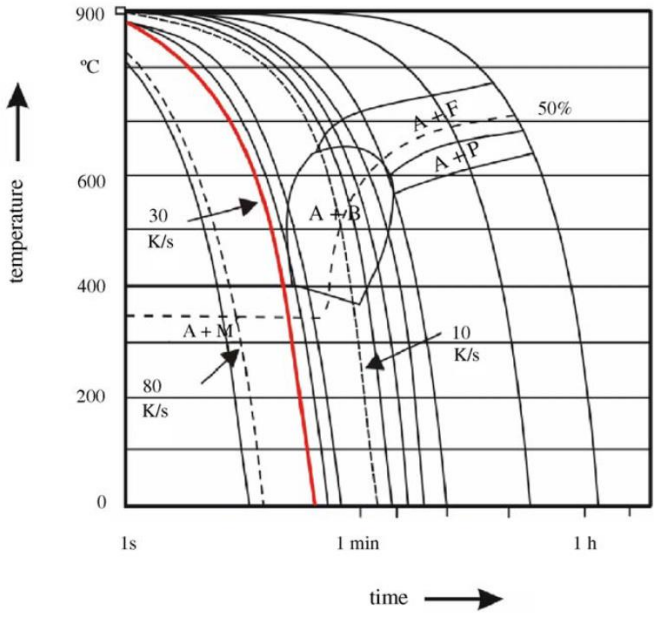

Figure 5: Typical continuous time temperature transformation (TTT) diagram of PHS by Merklein and Lechler [6].

1.3. Formability of Press Hardened Steel During Hot Stamping

Marciniak testing is employed to characterize formability under in-plane deformation without bending and to minimize the effect of friction between the specimen and punch using a carrier

blank with a central hole. This allows necking and fracture to occur at the apex of the blank according to Noder and Butcher [24]. For the test to be valid, localization must occur in the blank within the central hole of the carrier blank. Otherwise, the Marciniak test would be invalid. In addition, edge fracture must not occur at the carrier blank center hole prior to the blank fracture.

While the formability of PHS during hot stamping is relatively high, it remains a limiting factor for parts with high degrees of geometrical complexity. Forming limit curves (FLC) are used in sheet metal forming to define the maximum major and minor strains achievable by a material during deformation. Several test methods exist to measure the limit strains of a material during hot stamping such as the Nakazima and Marciniak tests (Figure 6), as prescribed by the ISO 12004-2 standard [25]. Both feature a binder that clamps the sample against a die to prevent drawing and a punch that deforms the sample against the die through a linear motion.

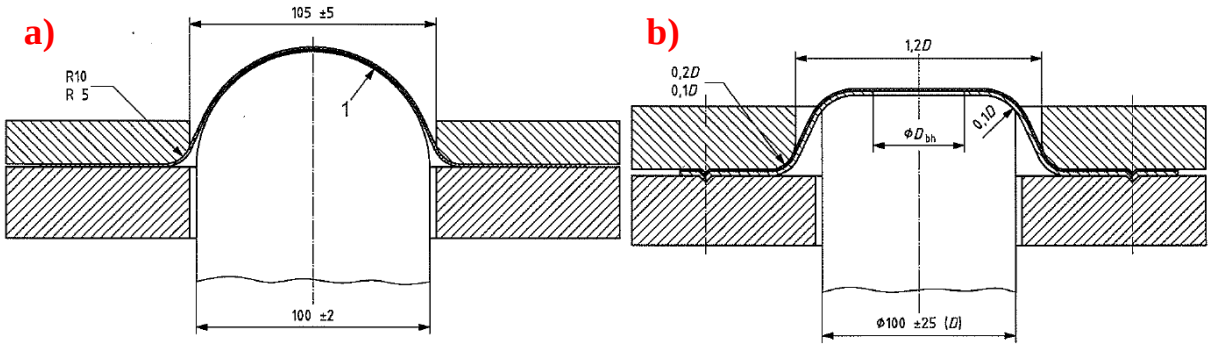

Figure 6: Cross sections of ISO12004-2 [25] tooling geometry for: a) Nakazima hemispherical punch, b) Marciniak flat punch. All dimensions are in millimeters.

In these formability tests, narrower sample gage widths produce a uniaxial stretch (or draw state) with positive major strains and negative minor strain values related to contraction of the width. Wider gage widths produce biaxial stretching with positive major and minor strains.

There are several methods to detect the onset of necking such as the time-dependent strain rate method of Volk and Hora [26] that monitors the thinning strain rate as well as curvature-based methods of DiCecco *et al.* [27] and Min *et al.* [28]. Curvature-based methods monitor the local curvature to detect the formation of an acute neck which corresponds to a negative curvature relative to the punch geometry. The ISO12004-2 standard uses curve fits of the major strain distribution at the image frame prior to fracture to detect the necking limit strains [25].

1.3.1. Nakazima Testing in Hot Stamping

Formability characterization at elevated temperatures is particularly challenging. Li *et al.* [29] used Nakazima tests on uncoated UHSS using specimen gage widths of 20 mm to 180 mm at an interval of 20 mm under hot stamping conditions. The surface of each sample was photochemically etched with circle grids to measure the strains after forming. FLCs were produced for sample thicknesses of 1.4, 1.6, and 1.8 mm (Figure 7). They were modelled using the Logan-Hosford yield criterion and Oh's ductile fracture criterion [30]. With data gathered from the Nakazima tests, the formability of simulated B-pillars was shown to decrease as thickness increased, because a thicker sheet metal had a lower cooling rate than a thinner one. Li *et al.* [29] showed that hot formability was significantly affected by sheet thickness, because thicker sheets had a lower cooling rate and thus higher limit strains.

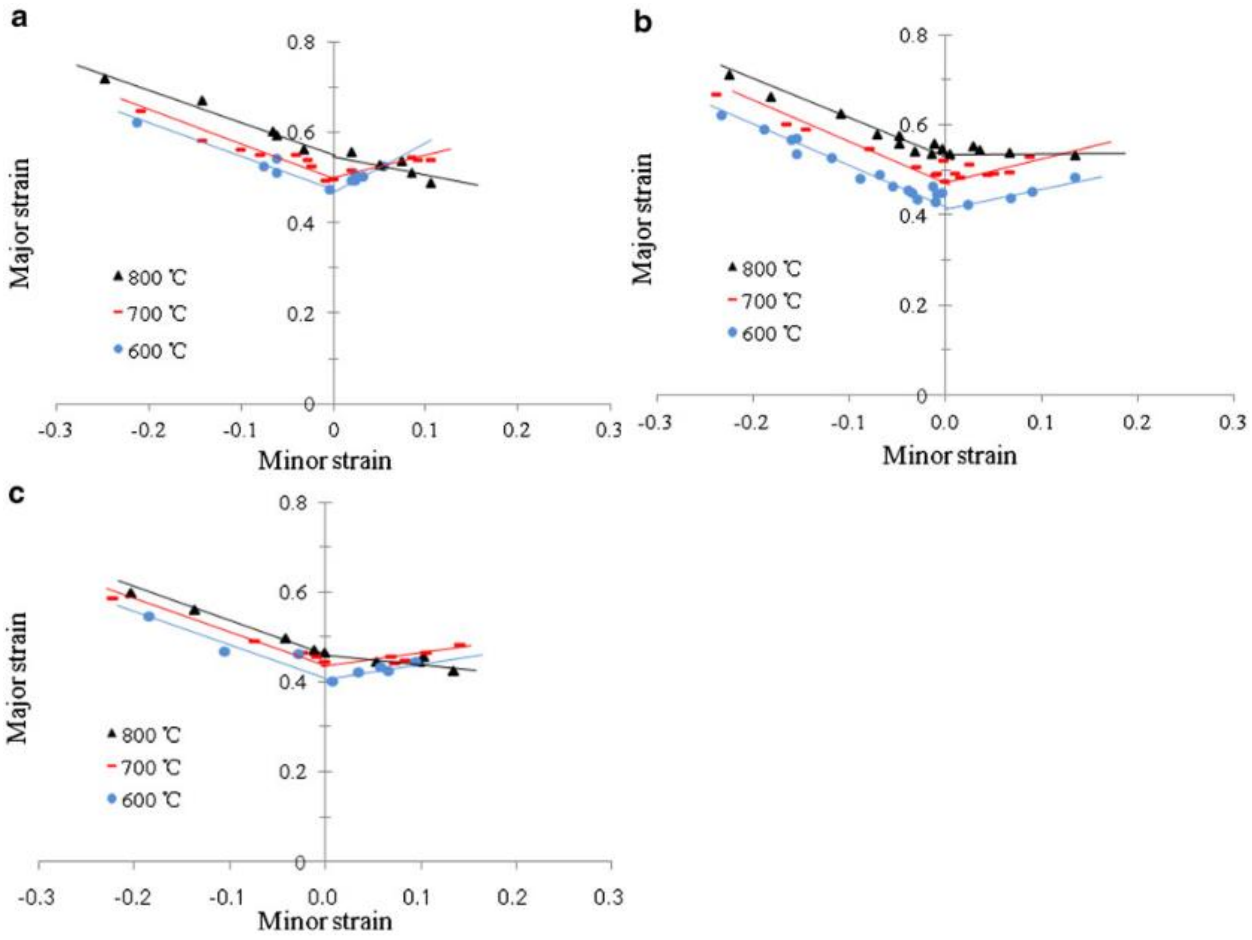

Figure 7: Forming limit diagrams (FLD) of 22MnB5 at various temperatures and thicknesses (a) 1.8 mm, (b) 1.6 mm, and (c) 1.4 mm by Li et al. [29]

Dahan et al. [31] reported the maximum major strain of about 0.4 in plane strain for axisymmetric circular blanks using a Nakazima test with hot stamping conditions. By decreasing the sample gage width (Figure 9), the strain path shifted from plane strain closer to uniaxial tensile strain, as shown in Figure 8. Each sample geometry featured a uniform width throughout its length unlike ISO12004-2 geometries.

Dahan et al. [31] have shown that all their fracture locations were ductile. In Nakazima tests, a narrower width enabled a higher punch displacement at necking. In addition, the strain paths of a narrower width produced more negative minor strains and higher major strains at necking/fracture. However, even the widest samples were unable to produce equibiaxial deformation due to friction and relatively low temperature at the sample center. A higher initial temperature of the sample improved formability.

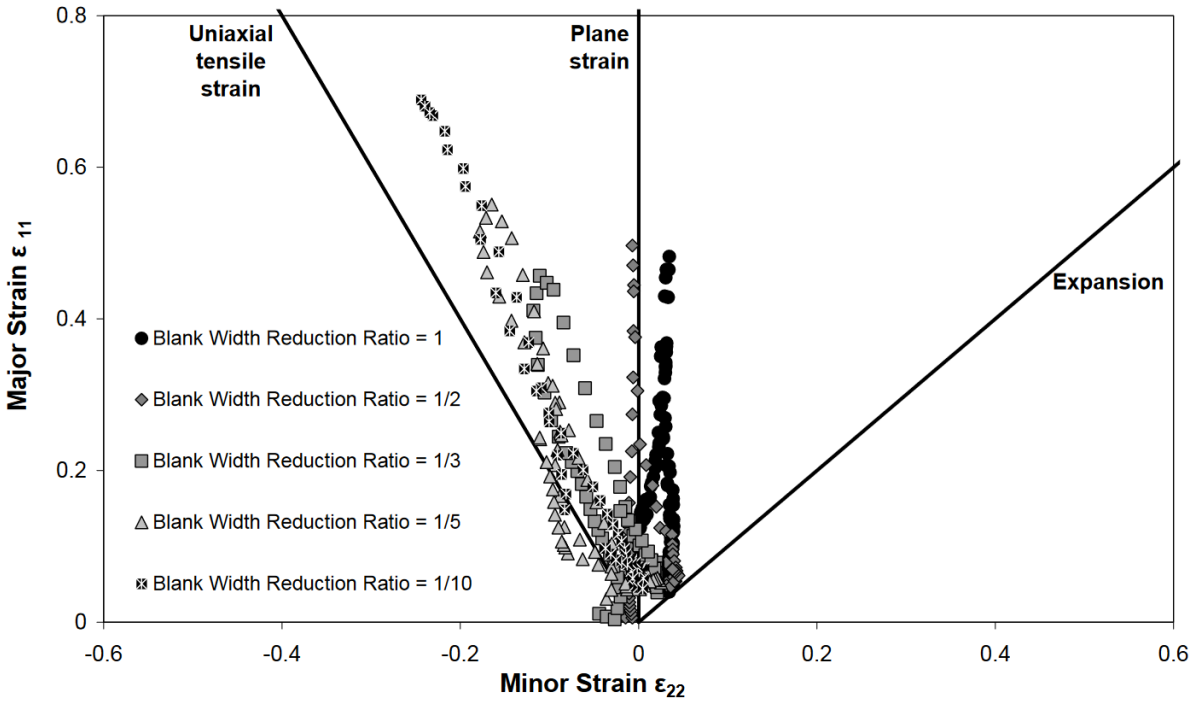

Figure 8: Forming limit diagram (FLD) of Usibor 1500P® using a modified Nakazima test by Dahan et al. [31]

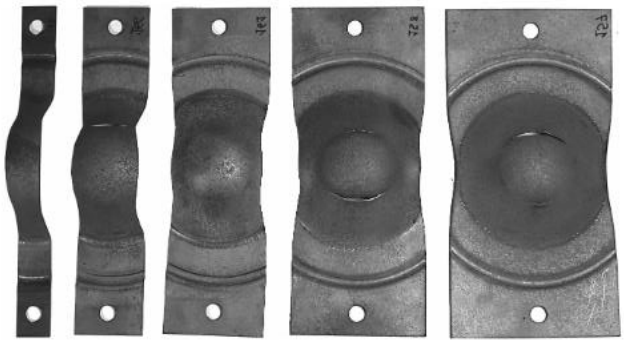

Figure 9: Nakazima test samples with various gage widths that are the same as the remaining sample width by Dahan et al. [31]

Bariani *et al.* [32] investigated the formability limits of Al-Si coated Usibor 1500 using Nakazima tests. The blank was maintained at an isothermal temperature of 600°C by a 30 kW inductive heating system. A K-type thermocouple spot welded at the center of the sample controlled the sample temperature through a feedback loop. A forming stroke speed of 10 mm/s was adopted to approach hot stamping speeds. A 0.10 mm thick graphite foil lubricated the sliding motion between the punch and blank. Usibor 1500 has shown high sensitivity to strain rate at this forming temperature. The resulting forming limit diagram (FLD) with necking limit strains determined using the ISO12004-2 method [25] spanned a limited range of minor strains from -0.1 to 0.25 (Figure 10).

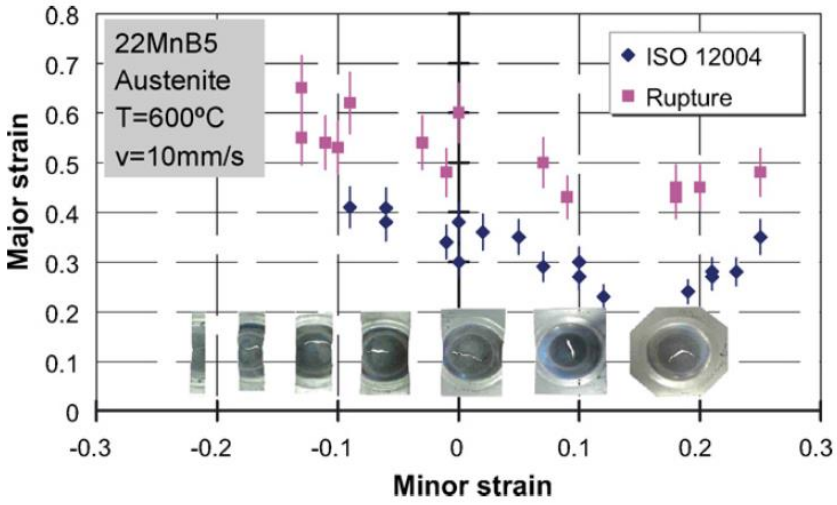

Figure 10: Forming limit diagram (FLD) of 22MnB5 metastable austenite at an isothermal temperature distribution of 600°C by Bariani et. al. [32]. Necking limit strains are determined using the ISO method [25].

Since the apex of the Nakazima dome punch first contacted the center of the blank, the high cooling rate from thermal conduction from blank to punch caused the center of the blank to have the lowest temperature within the blank. Combined with high friction between the punch and blank at the center, necking and fracture occurred at the exit of the punch radius, where the blank separated from the punch according to Kusumi *et al.* [22] and Dahan *et al.* [31].

To produce a temperature dependent thermal forming limit diagram, Shi *et al.* [33] used 2 mm thick hot stamping UHSS with sample widths varying from 20 mm to 180 mm and a lubricant composed of graphite and molybdenum disulfide. Figure 11 shows the experimental FLD of the UHSS obtained with the Nakazima test at a temperature of 800°C and at a constant punch speed of 8.33 mm/s. As shown in Figure 12, the necking and fracture locations occurred away from the sample center.

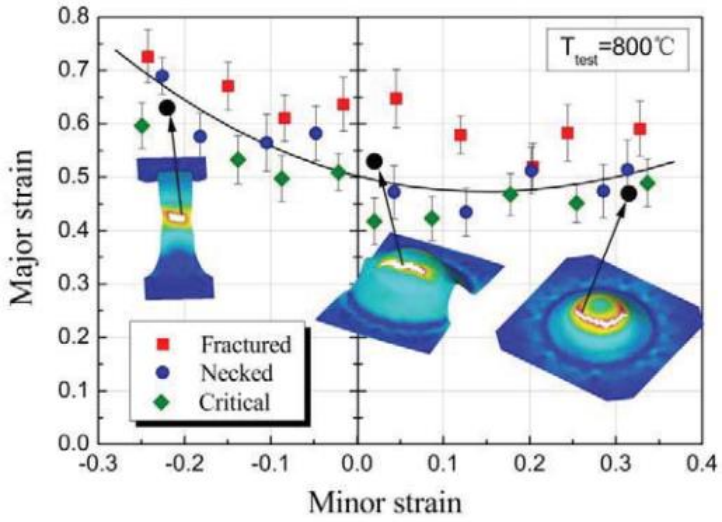

Figure 11: Experimental forming limit diagram (FLD) of 22MnB5 UHSS produced using the Nakazima test by Shi et al. [34]. Temperature: 800°C. Punch speed: 500 mm/min.

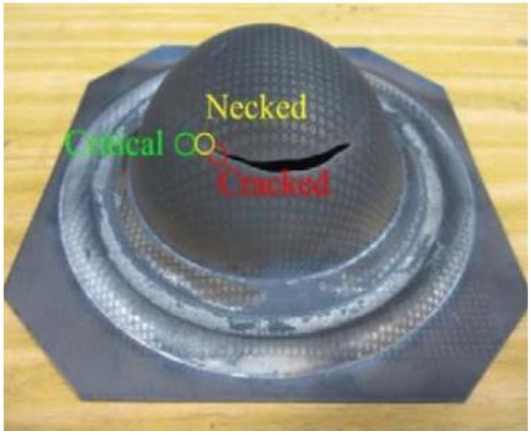

Figure 12: Fractured 22MnB5 UHSS 180 x 180 mm sample after Nakazima testing by Shi et al. [34]

Shi *et al.* [33] have also shown that a higher initial sample temperature enabled higher plane strain formability (Figure 13). This was apparent in the plane strain increase when initial sample temperature increased from room temperature to 800°C (Figure 13a).

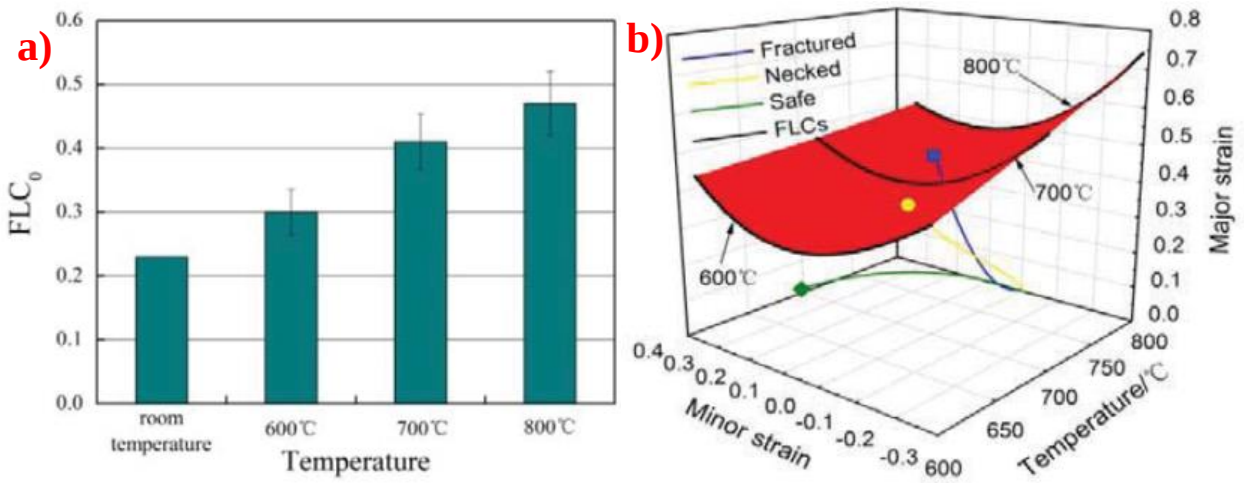

Figure 13: Nakazima dome testing by Shi et al. [34]: a) FLC0 of 22MnB5 UHSS at various initial sample temperatures. B) 3D FLD for 22MnB5 UHSS

1.3.2. Hot Formability Characterization using Cruciform Testing

Zhang *et al.* [35] proposed a biaxial cruciform test method (Figure 14) to characterize formability in hot stamping conditions. The sample was austenitized using direct resistance heating in a Gleeble thermal-mechanical simulator. To maintain temperature accuracy at the specimen center, a user subroutine UAMP in ABAQUS developed by Kardoulaki *et al.* [36] controlled the instantaneous specimen center temperature through feedback control of its surface current. This method predicted the thermal field of the area of interest through its electrical current input. The samples had a reduced thickness in the central region to promote localization where the temperature difference was less than 45°C.

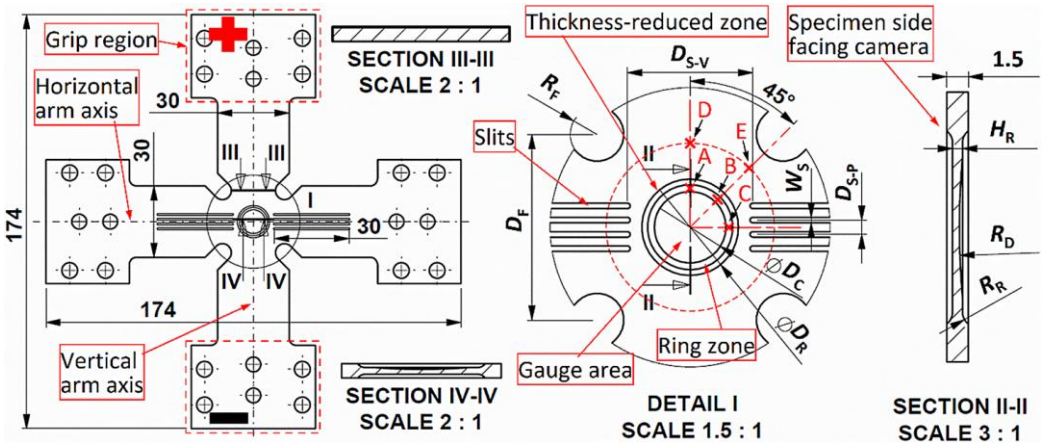

Figure 14: Biaxial cruciform test sample developed by Zhang et. al. [35] for hot stamping formability study on 22MnB5 steel

Using the biaxial cruciform tensile system shown in Figure 14, Zhang et. al. [35] characterized the formability of zinc-coated boron steel 22MnB5 at hot stamping temperatures and strain rates, as shown in Figure 15. The necking and fracture FLDs were obtained at a temperature range from 750°C to 850°C and at a strain rate range from 0.02 s^{-1} to 0.5 s^{-1}.

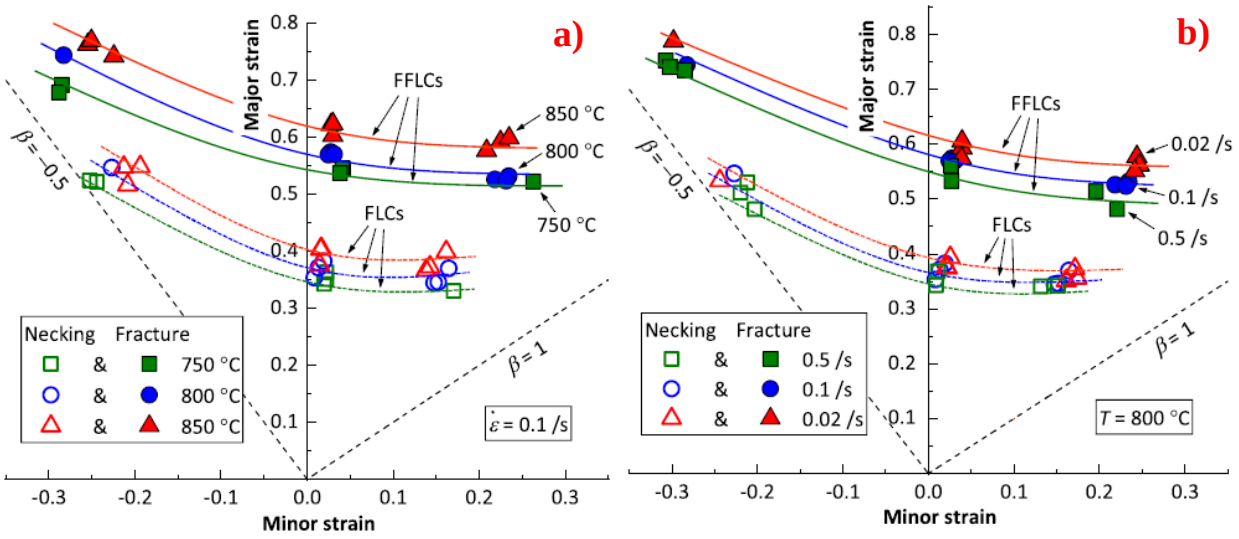

Figure 15: Necking and fracture forming limit diagrams (FLD) for zinc-coated boron steel at hot stamping temperatures obtained with a biaxial cruciform tensile system by Zhang et al. [35]: a) Temperature range from 750°C to 850°C at a constant strain rate of 0.1 s^{-1}. b) Strain rate range from 0.02 s^{-1} to 0.5 s^{-1} at a constant temperature of 800°C

1.3.3. Application of Hot Forming FLC Data

The use of high temperature FLC data within finite element simulations of hot forming operations has been limited, largely due to the difficulty in incorporating temperature and rate dependent FLC data in existing software, as well as the lack of available data. Kusumi and Nomura [22] used LS-DYNA to model deformation behaviour of a hot stamped B-pillar using a coupled structural-thermal simulation. The deformed component was represented with elastic-plastic shell elements, and the tooling with rigid shell elements. The coefficient of friction (CoF) was obtained with a drawing test for heated samples and ranged from 0.5 to 0.6 in the simulation. Heat transfer coefficients (HTC) were obtained through continuous temperature measurement using thermography. Although the hot stamping simulation by Kusumi and Nomura [22] did not produce any FLC, the fracture location of a B-pillar was accurately predicted using their model. Similarly, Li *et. al.* [29] used Autoform with the Logan-Hosford yield criterion and Oh's ductile fracture criterion [30] to predict the formability characteristics of a 22MnB5 steel B-pillar in hot stamping. Dahan *et al.* [31] used a combination of Forge2®, Forge3®, and Abaqus finite-element software to perform thermo-mechanical simulations of Nakazima testing in hot stamping with the numerical strain distribution of circular PHS1500 samples shown in Figure 16.

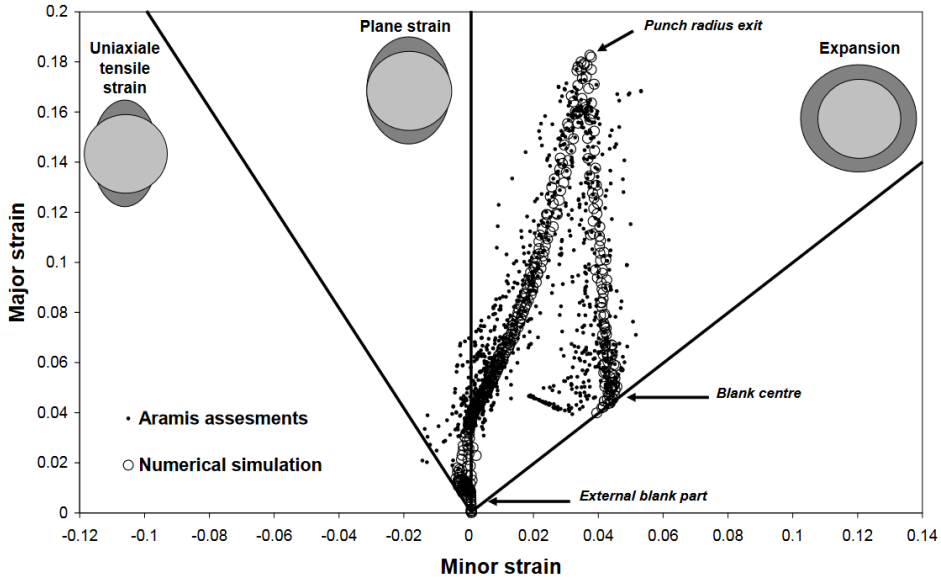

Figure 16: Numerical strain distribution of circular Usibor 1500 samples in Nakazima testing under hot stamping conditions by Dahan et al. [31]. Punch stroke: 20 mm. Punch velocity: 30 mm/s. Blank thickness: 1,5 mm. Blank initial temperature: 780°C

1.4. Friction Characteristics of Press Hardened Steel

Friction is a key boundary condition between the sheet metal and tooling, particularly in hot stamping since lubrication is difficult at such high temperatures. The effect of friction is critical in Nakazima formability tests under hot stamping conditions because it promotes plane strain localization away from the punch apex. Several previous studies have characterized the friction operative under hot stamping conditions.

Hardell *et al.* [3] used an Optimol SRV reciprocating friction and wear test machine (Figure 17) to characterize the CoF for a high strength boron steel.

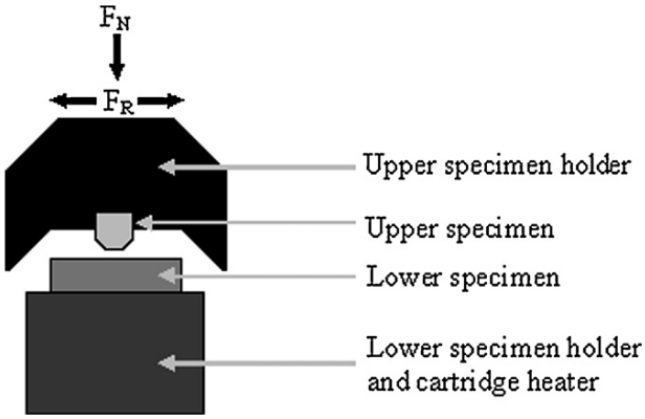

Figure 17: Schematic diagram of the Optimol SRV reciprocating friction and wear test machine used by Hardell et al. [3]

The two test specimen variants were uncoated and coated with Al-Si. Three tool steels with and without plasma nitriding were used as the tooling material in the SRV tests. The specimens were heated to constant test temperatures of 500°C, 600°C, and 800°C. Hardell *et al.* [3] determined that sliding speed had a marginal effect on CoF, while an increase in contact pressure led to a decrease in CoF. Due to the high temperature of the blank in hot stamping, lubricant was not usually applied prior to forming. Therefore, asperities on the tooling surface and blank were in direct contact without any lubricant separation. At lower test temperatures of 500°C and 600°C, the initial CoF was high and oscillated through the test. At 800°C, the test produced more constant CoF values as shown in Figure 18.

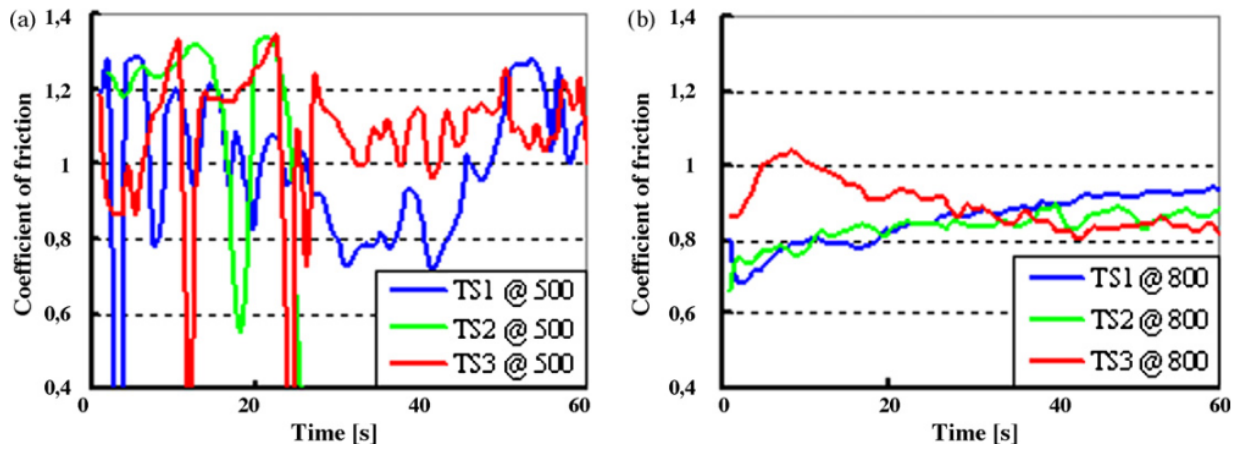

Figure 18: CoF of Al-Si coated boron steel against three plasma nitride tool steels in Optimol SRV friction testing for specimen temperatures of a) 500°C and b) 800°C. Load: 20 N. Stroke: 2 mm. Frequency: 50 Hz.

The friction mechanisms involved were mainly adhesion and ploughing for Al-Si coated boron steel according to Hardell *et al.* [37]. The characteristics of adhesion were affected by the interfacial shear strengths of the materials, their real contact area, and their hardness values. Ploughing was determined by the surface roughness of the blank and its tooling.

Venema *et al.* [38] determined that the CoF of Al-Si coated PHS against uncoated tool steel was dependent on the blank temperature in strip drawing tests. When the specimen was tested against a tooling surface in new condition, the CoF was found to be temperature dependent during initial sliding. However, consecutive tests using new specimens on the same tooling surface showed a lower dependency on temperature. Nonetheless, specimen temperature determined the wear mechanism, where adhesive wear was dominant below 600°C while abrasive wear with compaction galling became dominant above 600°C.

Yanagida *et al.* [39] also found that the mean CoF increased with increasing temperature in strip drawing tests for aluminum coated 22MnB5 steel against SKD61 steel tooling material. The main friction mechanism changed from abrasive wear between 650°C and 750°C to adhesive wear below 600°C in unlubricated conditions [38]. This dependence became less sensitive when layers of adhered material were built-up on the tooling surface [38]. When a lubricant was sprayed on the dies, the CoF decreased significantly compared to its unlubricated condition at specimen temperatures of 600°C, 720°C, and 800°C.

Although initial tooling surface conditions affected the CoF, the CoF became constant after an initial running-in for untreated tooling surface [37]. This stabilization of the CoF was caused by material transfer from the Al-Si coating to the tooling surface, which maintained a consistent surface profile through wear [37]. The tooling surface could also transfer its constituents to the Al-Si coating and create a layer of oxidized wear debris above the coating according to Pelcastre *et al.* [40]. This protective layer reduced material transfer by decreasing tooling surface contact with the Al-Si coating underneath.

Various tribological test methods have been used to characterize the friction of UHSS in hot stamping, such as the pin-on-disk test (Figure 19), in which a cylindrical pin made of hot work tooling material contacted a flat rotating disk made of UHSS [40]. The advantages of the pin-on-disk consisted of easily adjustable test conditions and the prevention of repeated contact area by moving the pin radially on the disk. Although contact conditions in pin-on-disk tests could be easily modified, they deviated from those in a hot stamping process. The contact surface was small

and could cause excessive ploughing at the contact point due to material build-up in front of the pin that overestimated the CoF [41].

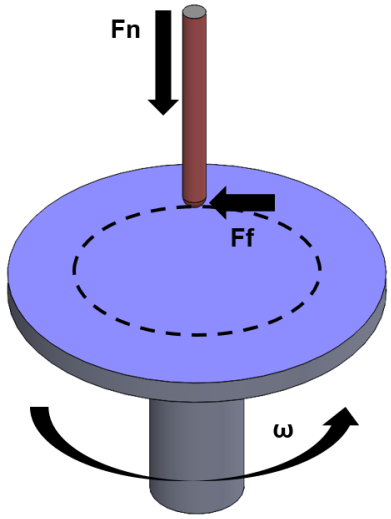

Figure 19: Pin on disk friction characterization method

A tribosimulator apparatus for flat drawing developed by Yanagida *et al.* [39] (Figure 20) has also been used to replicate friction conditions in hot stamping. A pair of flat clamps made of tooling material contacted a strip of UHSS, which was pulled through a pair of clamps at a constant speed. As the continuous UHSS strip exited the austenitization furnace, it directly entered the clamps. The advantages of the flat drawing test consisted of a large contact area similar to hot stamping and no repeated contact with the same surface area of the blank. However, the representation of the transfer process from the furnace to the stamping press was limited by the drawing speed.

The study by Yanagida *et al.* [39] showed that water-based lubricants sprayed on the tooling surface could significantly decrease the CoF under hot stamping conditions. Kusumi and Nomura

[22] also used a strip drawing test without lubrication for aluminized steel sheet in hot stamping conditions. The resulting CoF was determined to be between 0.5 and 0.6.

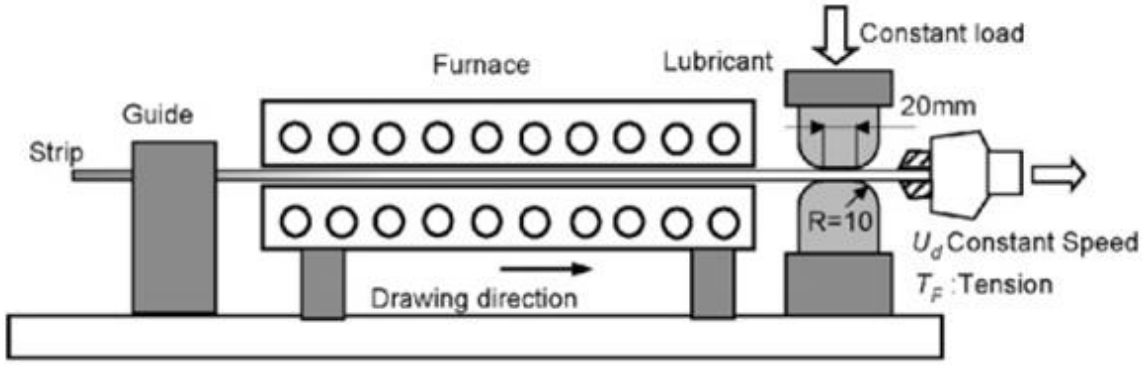

Figure 20: Flat drawing tribosimulator friction characterization method developed by Yanagida et al. [39]

1.5. Proposed Work

Past Nakazima tests have been performed to determine the formability of 22MnB5 PHS under hot stamping conditions. However, necking and fracture locations occurred away from the dome apex. The fracture locations do not appear to comply with the ISO12004-2 criterion of fracture occurring within a distance of 15% of the punch diameter away from the apex [25]. There has been considerable work on modelling deformation of PHS in hot stamping, but the characterization of formability has been given limited attention. Cruciform testing is promising but is prohibitive due to its complexity and requirement of custom test fixtures and control systems. Marciniak testing at high temperature appears to be overlooked within the literature. It could be further explored to characterize formability without the influence of friction and out-of-plane deformation due to bending and tool contact. Marciniak and hybrid Nakazima-Marciniak formability tests [35] have never been done on PHS with hot stamping conditions.

Strip drawing and pin on disk friction characterization tests have been performed in previous works on uncoated and coated PHS at high temperatures. However, the twist compression test (TCT) has not been performed on Al-Si coated PHS and can represent friction from tooling contact in hot stamping.

The current work used the TCT developed by Schey [42] to determine the CoF for Al-Si coated PHS1800 and PHS1500 under various values of sliding speed, contact pressure, and sliding distance. Since the TCT samples followed the same direct hot stamping process as the formability characterization samples, the TCT could assess the frictional behavior of hot stamped components during the forming/quenching phase.

As the TCT cup rotates on the surface of the sample, the results are independent of the sample's material anisotropy due to the axisymmetric geometry of the TCT cup. In addition, the TCT's ability to continuously rotate against the sample enables an unlimited sliding distance on the same sample.

The current study examines the formability of Al-Si coated PHS1800 and PHS1500 during a direct hot stamping process. The determined FLCs of these materials enable designers to prevent structural weak points caused by necking in hot stamped parts. By understanding their mechanical behaviors during the forming stroke, part failure can be prevented with adequate manufacturing process and tooling geometry. The numerical model developed for the hot stamping process can predict the strain field and temperature distribution within the hot stamped part throughout the

forming stroke. As a result, the tooling geometry, motion, and temperature can be adjusted to create the desired outcome in the hot stamped parts without a need for extensive physical experimentation. The cycle time, production costs, and part quality can be optimized according to the formability and friction characteristics of PHS1800 and PHS1500.

This thesis is organized as follows. Chapter 2 provides the experimental methods to determine the formability and friction characteristics of Al-Si coated PHS under unlubricated hot stamping conditions. Chapter 3 describes the numerical modelling of Nakazima, Marciniak, and hybrid Nakazima-Marciniak formability tests deployed the current work. Chapter 4 shows friction characterization results obtained with TCT and surface roughness measurements. Chapter 5 analyzes the experimental formability results. Chapter 6 analyzes the numerical simulation results for each formability test performed in this work.

2. Experimental Methodology

Friction and formability characterization tests were performed on two hot stamping steel grades, PHS1800 and PHS1500. To study the impact of hot stamping conditions on the CoF, the TCT was used to replicate friction between the tooling and test sample. Standard formability characterization tests, such as Nakazima and Marciniak, were then modified for hot stamping conditions. This chapter provides a description of the test equipment and experimental procedures.

2.1. Al-Si Press Hardened Steel (PHS) Variants

The PHS1500 is a boron steel of nominal composition 22MnB5, with a nominal ultimate tensile strength of 1500 MPa after hot stamping. The microstructure will be fully martensitic if the cooling rate during quenching is greater than 27°C/s [15] [43]. The composition of the PHS1500 steel, reported by ArcelorMittal [44], is shown in Table 1. The PHS1500 sheets were coated with Al-Si on both sides to prevent against oxidation, decarburization, and hydrogen embrittlement during austenitization [9]. Two nominal Al-Si coating thicknesses were considered for the PHS1500: AS150 at 150 g/m^3 and AS80 at 80 g/m^3. The AS150 coating thickness has seen greater usage in industry, while the lighter AS80 coating thickness has been introduced as a lower cost option [45].

The second steel considered is a newer development of PHS of nominal composition 37MnB5 [46] with a nominal ultimate tensile strength of 1800 MPa. It is designated PHS1800. The PHS1800 sheet is also coated with Al-Si at 150 g/m^3. The results from the chemical analysis of PHS1800

base metal are shown in Table 1. All PHS sheet used in this thesis have an as-received nominal thickness of 1.6 mm which includes the thickness of the Al-Si coating.

Table 1: Chemical composition of PHS1500 and PHS1800 base metal in weight percent obtained from chemical analysis using inductively-coupled plasma atomic emission spectroscopy [47] (ASTM D1976-20 [48]), and by combustion and inert gas fusion techniques (ASTM E1019-18 [49]). The Al-Si coating was milled off from the base metal prior to chemical analysis. PHS1500 composition taken from [50].

	C (%)	Si (%)	Mn (%)	P (%)	Al (%)	Cr (%)	Ti (%)	B (%)
PHS 1500	0.22	0.26	1.17	0.013	0.031	0.17	0.034	0.003
PHS 1800	0.33	0.57	0.60	0.012	0.045	0.31	0.021	0.002

2.2. Friction Characterization Experimental Methodology

This section describes the TCT apparatus used to perform high temperature friction characterization.

2.2.1. Test Equipment

The TCT apparatus involves a hollow cylindrical friction cup rotating against the surface of a stationary test specimen, which was supported by a gimballed holder, as shown in Figure 21 [51]. The TCT was developed at the University of Waterloo by Schey [52], and later significantly modified by George [53] to perform high temperature friction tests [51]. Figure 21 shows the main components that constituted the TCT apparatus. Cartridge heaters and embedded thermocouples were used to heat the friction cup and specimen holder and maintained a constant temperature for each. The temperature was set to 80°C to represent the temperature of the hot stamping tooling in a production environment. To maintain a solid grip on the friction cup while allowing easy

replacement, a machine screw was inserted into a dedicated groove on the side of the friction cup that pressed it against the heated friction cup holder. This created a large contact surface between the friction cup and its holder, thus allowing the friction cup to heat up rapidly with good thermal conduction.

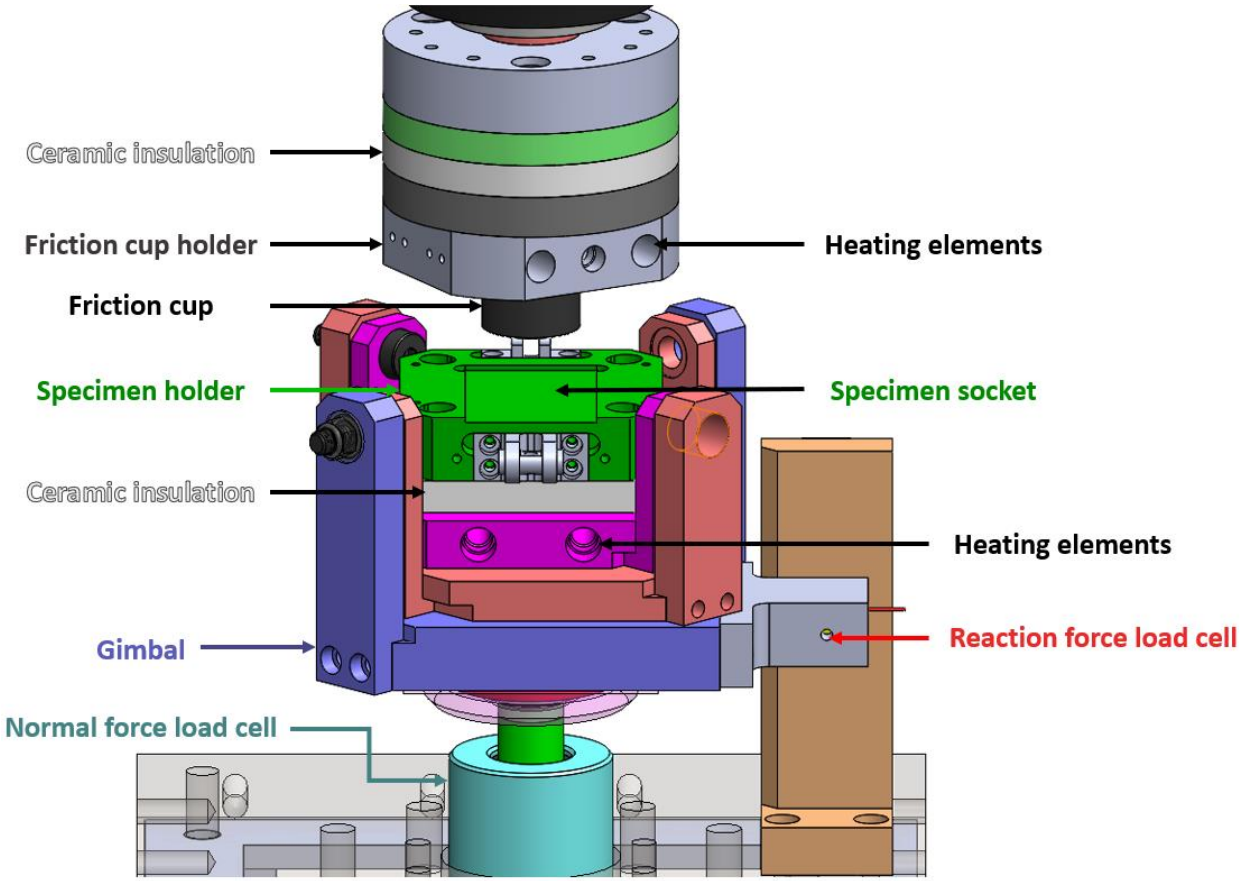

Figure 21: CAD Schematic of TCT apparatus

The TCT measured the CoF with a hollow axisymmetric friction cup that rotated against the surface of the test specimen. By applying a known normal force between the friction cup and specimen, the CoF could be calculated through reaction force measurements from the reaction

torque through equation (1). As the friction cup rotated, sliding distance increased and the corresponding CoF was measured.

$$\mathrm{CoF} = \frac{\mathrm{F_f}}{\mathrm{N}} = \frac{\mathrm{T}}{\mathrm{r_m N}} = \frac{\mathrm{F_a r_a}}{\mathrm{r_m N}} \tag{1}$$

F_f is friction force; N is applied normal force from the specimen holder; T is reaction torque from the specimen holder due to friction; r_m is the centerline cup radius (22.225 mm), which corresponds to the reaction torque arm length formed by the average between the outer radius (25.4 mm) and the inner radius (19.05 mm) of the contact area as shown in Figure 22b; F_a is the measured reaction force from the torque arm of the specimen holder; r_a is the radius formed between the torque arm load cell and the center of rotation.

To apply the nominal normal force N, a double-acting hydraulic linear actuator was vertically connected to the specimen holder through a load cell. Since the load cell was connected in series to the actuator shaft, it measured the applied force on the specimen to provide feedback to an MTS 407 servo-hydraulic controller operating in a closed feedback loop.

Another load cell installed at the torque arm end of the specimen holder prevented the holder from rotating and measured CoF according to the Coulomb model of friction through equation (1). This load cell measured the reaction force F_a created by friction resistance from which the reaction torque can be determined based on the torque arm.

The friction cup holder was driven by a hydraulic motor, whose rotational motion was measured by a string potentiometer which provided feedback to the controller. As the friction cup rotated against the specimen, the specimen holder had a 50.8 X 50.8 mm square groove that acted as a socket for the specimen. To maintain a uniform contact pressure against the friction cup, the specimen holder was mounted on a gimbal to establish a parallel position with the friction cup regardless of any geometric imperfections.

The friction cup was made of Uddeholm Dievar tool steel hardened to 53 HRC that was commonly used for hot stamping tooling. Its contact surface featured a concentric cylindrical profile, as shown in Figure 22b. To achieve a smooth surface similar to production hot stamping tooling, the surface of the cup friction surface was lapped prior to testing. Since the friction sliding motion was circular, the measured CoF was independent of sheet rolling direction.

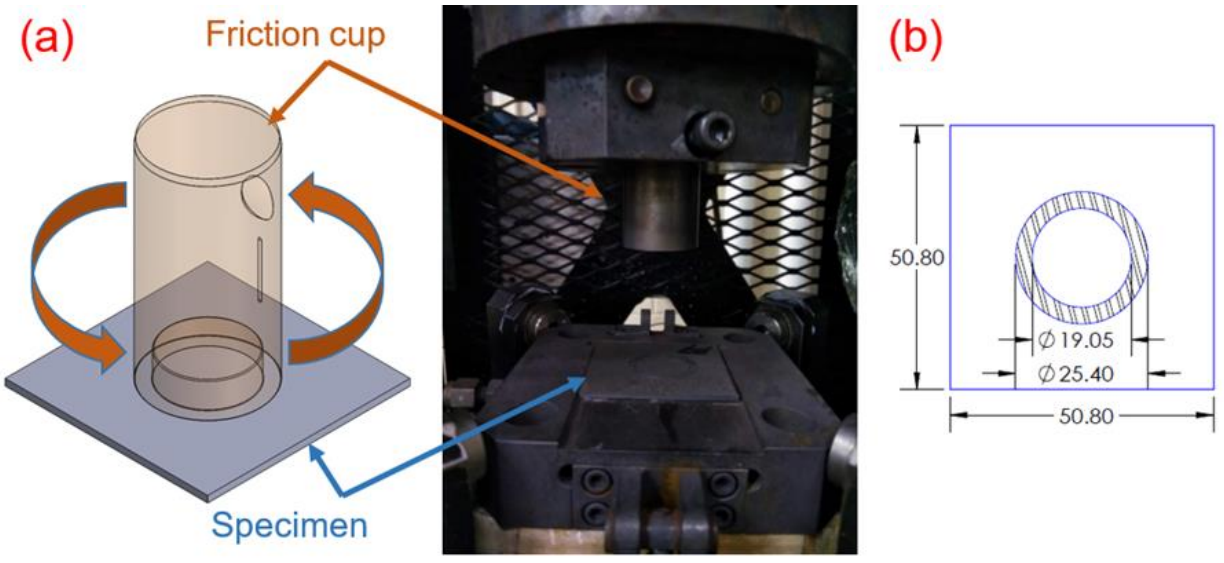

Figure 22: (a) Rotating friction cup made of Uddeholm Dievar hot work tool steel. The PHS1800 test specimen is located below on a stationary holder. (b) The concentric contact profile of the friction cup has an outer diameter of 25.4 mm, and an inner diameter of 19.05 mm. Contact occurs on a square and flat test specimen.

To compensate for thermal expansion of the specimen after austenitization and to facilitate its transfer into the TCT apparatus, the specimen geometry must be smaller than the 50.8 X 50.8 mm square groove but not by too much to prevent excessive movement at the start of rotation. According to Cao *et al.* [54], the thermal expansion coefficient α_T of PHS was estimated at $12.2 \times 10^{-6}/K$. Cao *et al.* [54] did not specify whether this α_T value accounted for the steel lattice structure transformation from body-centered cubic (BCC) to face-centered cubic (FCC). Using equation (2), the initial length of each side l_0 was calculated at 50.2 mm when the final allowable length l_f was 50.8 mm with an increase in temperature ΔT from room temperature, 25°C, to austenitization temperature, 930°C. For ease of specimen manufacturing and ease of transfer process, each square specimen side was limited to a maximum length of 50 mm.

$$\alpha_T = \frac{\epsilon}{\Delta T} = \frac{\Delta l}{l_0 \times \Delta T} = \frac{l_f - l_0}{l_0 \times \Delta T} \leftrightarrow l_0 = \frac{l_f}{\alpha_T \times \Delta T + 1} \tag{2}$$

A ZIRCAL-95 ceramic plate was installed between the specimen holder and the gimbal for thermal insulation. To provide additional thermal protection, a continuously circulating cold water pipe was installed below the ceramic plate to remove excess heat.

Due to hardware and software limitations, the minimum applicable pressure by the friction cup on the specimen was 5 MPa, which was sufficient to maintain alignment of the gimballed specimen holder. To avoid overloading the gimbal and drive mechanisms, the maximum applicable pressure

was limited to 30 MPa. Since a hot stamped PHS specimen could be subjected to higher values of contact pressure, the friction characteristics in that scenario must be extrapolated from existing measurements.

A total sliding distance of 100 mm was maintained for all tests. According to George [51], the CoF data became too noisy for any significant analysis when the sliding speed was below 10 mm/s. Thus, the minimum nominal sliding speed was set to 10 mm/s. The maximum sliding speed achievable was 38 mm/s.

The Carbolite chamber furnace was used for austenitization of the TCT samples, as shown in Figure 23. After austenitization, the specimen was manually transferred from the furnace to the TCT apparatus.

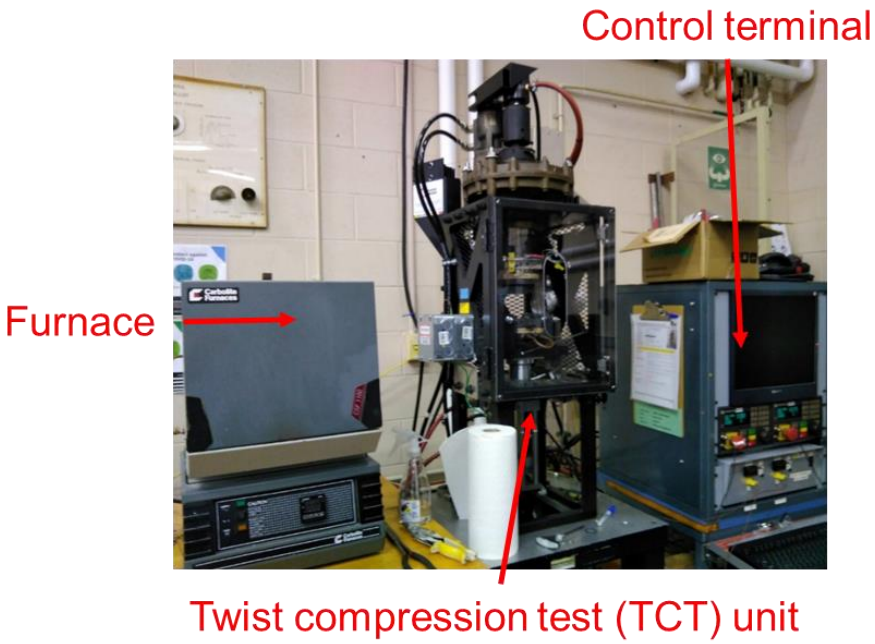

Figure 23: TCT apparatus setup showing furnace located adjacent to apparatus. The control terminal is connected to the TCT unit for all motion and heating parameters.

2.2.2. TCT Test Conditions

Prior to testing, all friction cups and PHS1800 specimens were cleaned in soapy water, rinsed with acetone, and dried with a paper towel to remove surface contaminants. The blanks were austenitized at a nominal temperature of 930°C and a hold time of 5 minutes. The manual transfer from the furnace to the TCT frame and start of the test occurred over a period of approximately 10 seconds. The applied contact pressure increased linearly to its nominal value over a sliding distance of 10 mm. The measured CoF data was recorded using a custom script written in LabView software.

After each test, the blank and friction cup were replaced with a new set to prevent excessive wear on the same surface. Each set of test conditions involved five repeats for statistical significance. Before inserting a new specimen into the furnace, the interior must be reheated to the nominal austenitization temperature of 930°C.

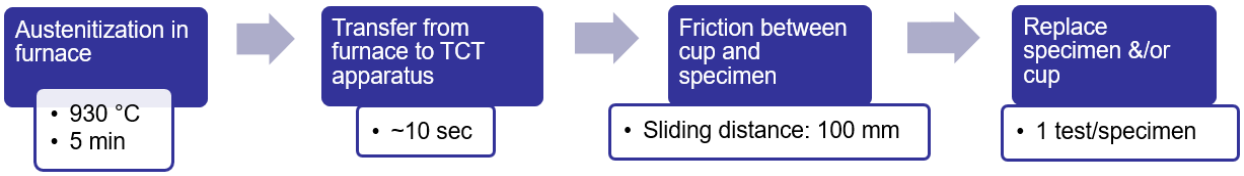

Figure 24: TCT test process

To measure the impact of sliding speed on CoF, four sliding speeds, shown in Table 2, were selected between 10 and 38 mm/s with a constant contact pressure of 15 MPa.

The influence of contact pressure on CoF was evaluated with four contact pressures between the limits of 5 to 30 MPa, given in Table 2. To achieve a significant sliding distance within the 1 second time frame relevant to hot stamping forming stroke, a constant sliding speed of 20 mm/s was selected.

Table 2: Test matrix with contact pressures from 5 MPa to 30 MPa and sliding speeds from 10 mm/s to 38 mm/s. Each case has 5 repeat tests.

Sliding speed / Contact pressure	10 mm /s	20 mm/s	30 mm/s	38 mm/s
5 MPa				
15 MPa				
25 MPa				
30 MPa				

Additional tests were also performed to examine the effect of tool wear on CoF. In this set of tests, only the specimen was replaced after each test while the same friction cup was used for ten consecutive tests. Five sets of tool wear sequences using five different friction cups were completed for a total of 50 friction tests. These tests utilized a relatively high contact pressure of 30 MPa to promote higher levels of wear.

2.2.3. Surface Roughness Measurement

The surface roughness of the cups was measured at five different locations using a Taylor-Hobson contact profilometer (shown in Figure 25) over a distance of 2 mm. The precision of the contact profilometer was 0.02 μm Ra.

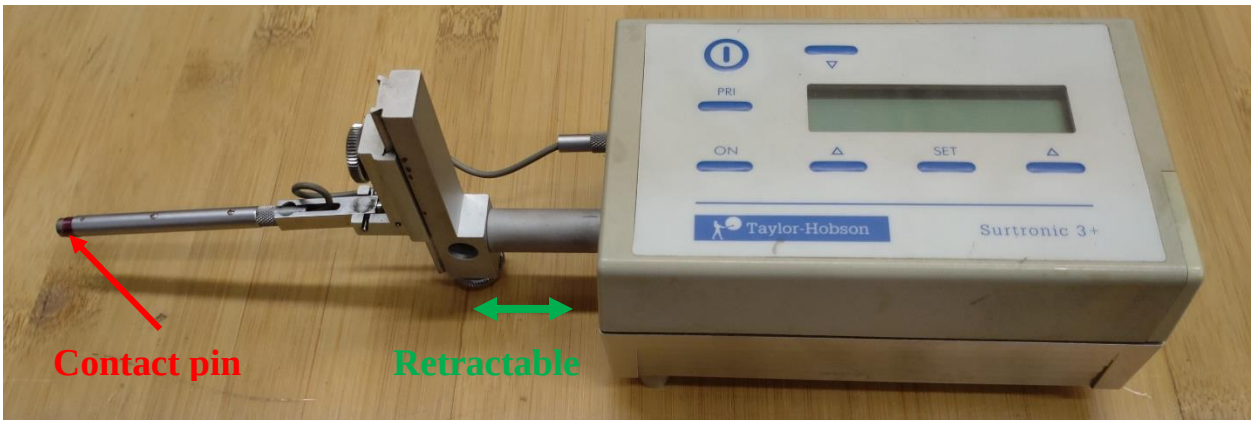

Figure 25: Taylor-Hobson contact profilometer. The contact pin is located on the underside of the retractable arm.

3D surface profiles of the test specimens were obtained using a Keyence optical profilometer.

2.2.4. Specimen Temperature History Measurement

Several temperature measurement methods were developed, as described in the following, to ensure the temperature history was representative of hot stamping conditions.

To obtain a reference temperature history at a location away from the area of contact between the friction cup and sample, a thermocouple was attached to the edge of the specimen by press-fitting.

Two methods were considered to measure the specimen temperature history in the contact area. One method used a modified specimen holder that was designed and fabricated as part of this research to enable a spring-loaded thermocouple. The other method used an embedded thermocouple inside the specimen to measure temperature beneath the contact area.

2.2.4.1. Spring-Loaded Thermocouple Approach

For the spring-loaded thermocouple approach, the thermocouple wire clamp was located in a cavity below the contact area and vertically supported by a compression spring with a stiffness of 2.2 N/mm. With a relaxed length of 16 mm and a compressed length of 12 mm, the spring applied a clamping force of 8.8 N on the thermocouple against the underside of the specimen contact area. A tunnel that connected the side of the specimen holder to the wire clamp cavity allowed the thermocouple wire to be routed from the data acquisition system (DAQ) to the wire clamp location (Figure 26). The two ends on the thermocouple were spot welded together to ensure that both wires could reliably contact the specimen. In addition, the spot-welded thermocouple end was ground to a smooth finish to maximize its contact surface area with the specimen. This maximized conduction heat transfer between specimen and thermocouple. It also reduced the temperature measurement delay and discrepancy caused by the temperature difference between specimen and thermocouple end.

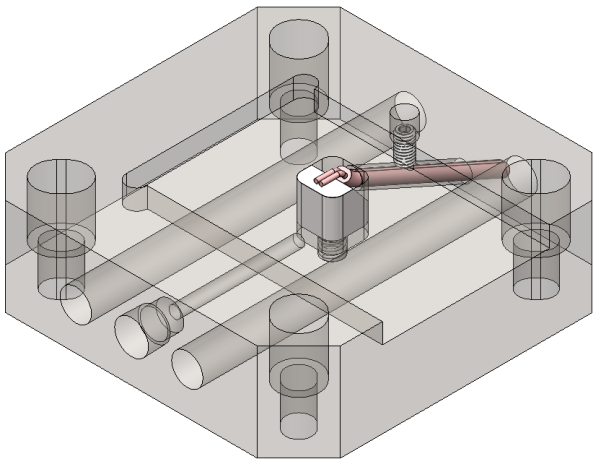

Figure 26: Model of the modified specimen holder to enable the use of a spring-loaded thermocouple to measure temperature history of the specimen contact area.

Several features of the original specimen holder, such as trunnions for an external specimen clamp, were removed on this modified specimen holder to free up workspace for a more efficient and rapid specimen transfer process. The specimen socket depth was increased from 0.920 mm to 6.35 mm (Figure 27) for easier positioning of the sample during the transfer process (Figure 28). This improved test reliability by preventing the specimen from falling out of its socket during its rapid manual positioning into the specimen holder.

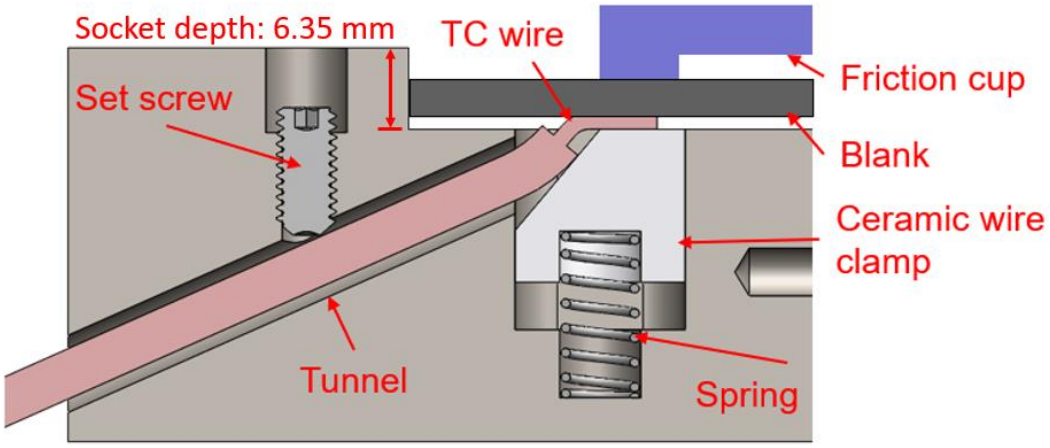

Figure 27: CAD model cross-section of the modified specimen holder showing the interior components.

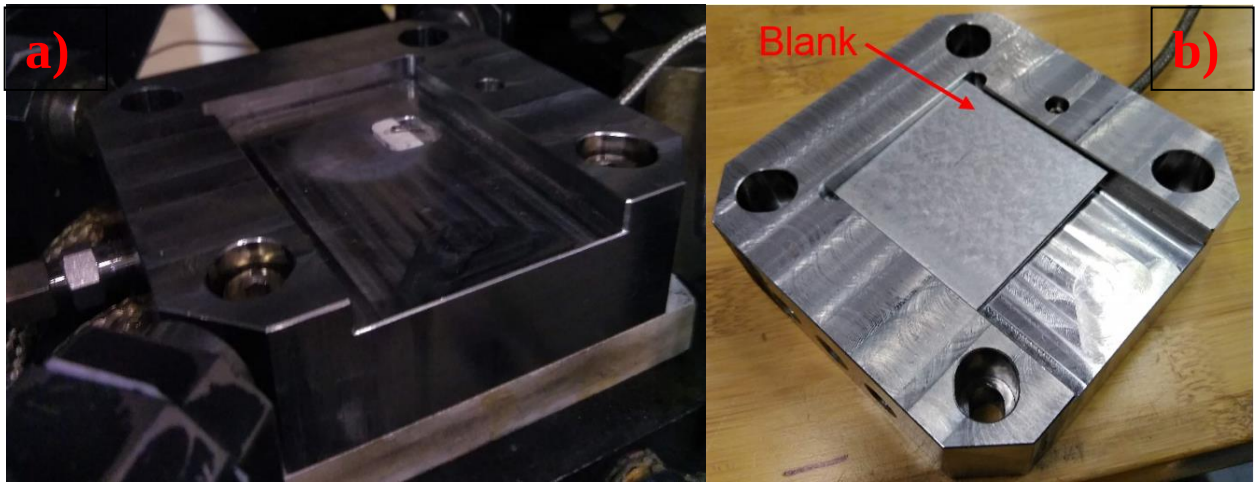

Figure 28: a) Modified specimen holder installed in the TCT apparatus with the spring-loaded thermocouple located below the friction cup contact area. b) TCT specimen placed on the modified specimen holder prior to contact with the friction cup.

Using the spring-loaded thermocouple to measure the contact area temperature, recording could only start once the sample was placed in the holder. A reference thermocouple provided temperature data during austenitization and transfer from the furnace. The spring-loaded thermocouple could only provide reliable data once the normal force has been applied to ensure proper contact.

2.2.4.2. Embedded Thermocouple Approach

The second method to measure the specimen thermal history in the contact area was to attach the thermocouple directly within the specimen interior, as shown in Figure 29. Since the thermocouple wires had a large diameter to sustain austenitization temperatures, inserting them into the thickness side of the specimen required precision machining of blind holes. The thermocouple wires needed to be press-fit into the blind holes to form a sturdy connection with the specimen.

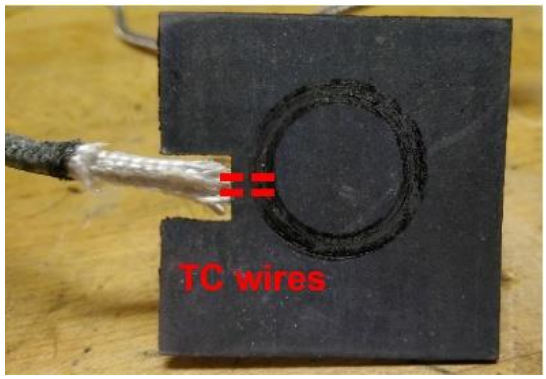

Figure 29: Thermocouple wires embedded beneath the contact area of a TCT specimen.

The test procedure remains identical to the standard TCT process described in Section 2.2.2. Due to the large diameter of the thermocouple that were connected to the external DAQ, the furnace

door did not achieve a complete seal for the heating chamber. During the transfer process, the high stiffness of the thermocouple prevented the specimen from staying in the specimen socket despite the improved socket geometry in the modified specimen holder. To maintain the specimen in its socket during the test, the operator must use pliers to hold the specimen in its intended position. The pressing action of the pliers on the specimen surface was assumed to produce negligible impact on the specimen temperature due to the small area of contact for thermal conduction.

2.3. Formability Characterization Experimental Methodology

To represent industrial forming attributes such as the use of a binder, die, and punch on sheet metal, Nakazima and Marciniak formability tests from ISO12004-2 [55], as well as a hybrid punch geometry due to Deng and McGuire [56], were modified to represent a direct hot stamping process.

2.3.1. Formability Test Equipment

The Nakazima dome test featured a 100 mm diameter hemispherical punch, as shown in Figure 30. The punch was made of hardened Uddeholm Dievar tool steel and was attached to the stationary base of the forming press. The die and binder had a 106.68 mm diameter center hole that was concentric to the punch perimeter. The die and binder entry radii were 8 mm (not shown for brevity).

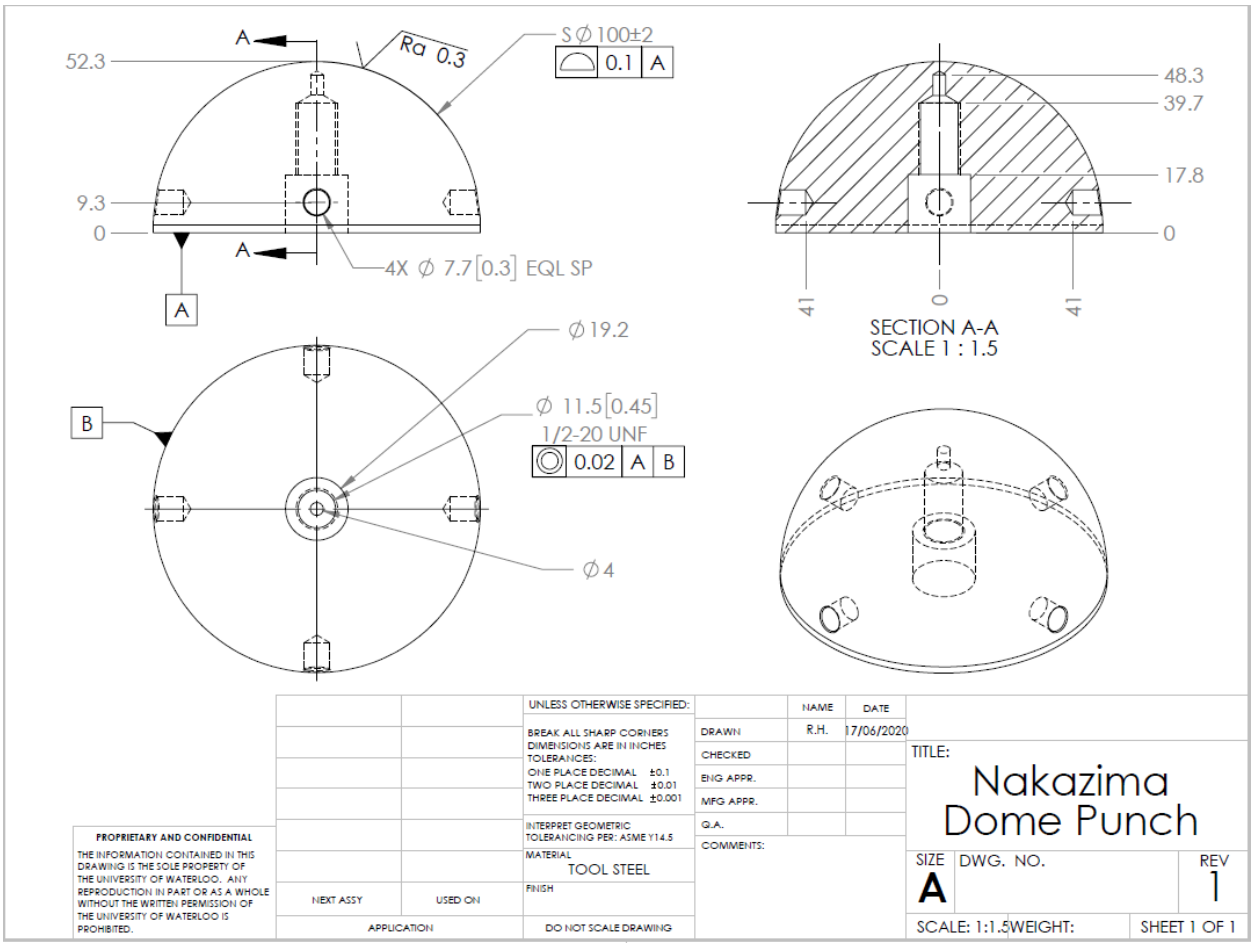

Figure 30: Nakazima dome punch geometry used in hot stamping tests. It is made of Uddeholm Dievar tool steel. All dimensions are in millimeters.

The second formability test, the Marciniak test, utilized a flat cylindrical punch with rounded shoulders, shown in Figure 31, which eliminated bending in the sample gage area. In addition, a mild steel carrier blank was placed between the sample and binder/punch to decrease friction on the sample gage area, as shown in Figure 32. It supported the shoulder of the sample and avoided fracture in that region. Like the Nakazima test, the outer diameter of the punch was 100 mm. The die center opening had a diameter of 110.6 mm and an entry radius of 12.7 mm (not shown for brevity).

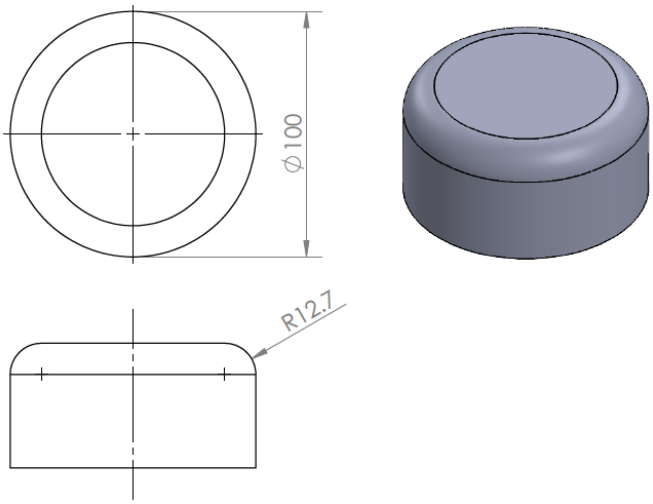

Figure 31: Marciniak punch geometry. The shoulder is tangent on both sides and has a nominal radius of 12.7 mm. All dimensions are in millimeters.

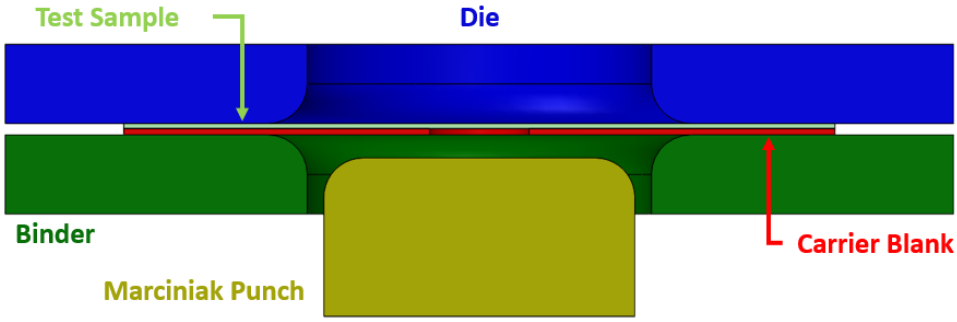

Figure 32: Marciniak test components schematic. Position of components is taken during clamping prior to the forming stroke.

The carrier blank was made of 2 mm thick mild steel, as shown in Figure 33. The carrier blank had a 32 mm diameter central hole such that there was no friction where the neck developed in the sample. Mild steel was chosen for the carrier blank due to its high formability and excellent hole expansion ratio (HER). The carrier blank formability must exceed that of the sample. To decrease friction between the carrier blank and the punch, three Teflon sheets with a nominal thickness of 0.127 mm per sheet were placed between the die/punch and carrier blank. The carrier blank and Teflon sheets were placed on the binder prior to each test.

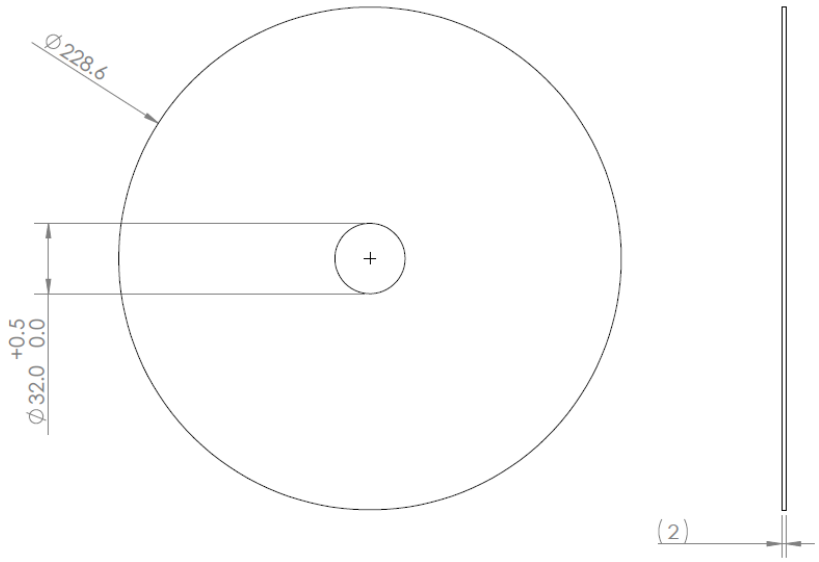

Figure 33: Carrier blank used in Marciniak and hybrid tests. The 32 mm diameter center hole edges are deburred and ground with 800 grit sandpaper.

A hybrid Marciniak-Nakazima test was considered based upon the geometry proposed by Deng and McGuire [56]. As shown in Figure 34, the hybrid punch profile started with a flat top section at the center and a large 25 mm shoulder. This shoulder radius was intermediate to that of the Marciniak punch (12.7 mm) but smaller than the hemispherical radius of the Nakazima punch (50 mm). The hybrid punch also used the same carrier blank as the Marciniak punch. A recessed circular hole at the center of the hybrid punch further prevented direct contact with the center of the sample gage section.

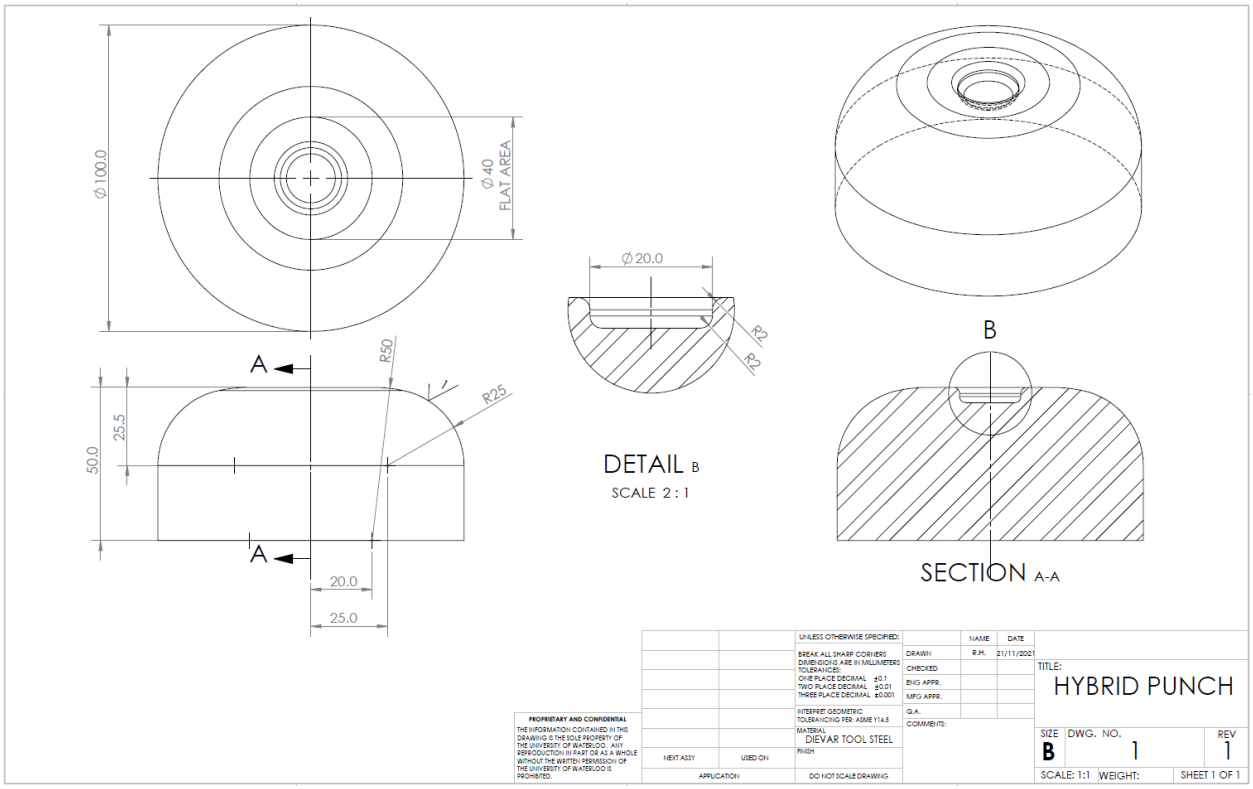

Figure 34: Hybrid Marciniak-Nakazima punch geometry inspired by work from Deng and McGuire [56]. The center of the punch begins with a flat section then transitions to larger shoulder radii toward the outer perimeter. All dimensions are in millimeters.

The die and binder were the same for all three punch configurations. The binder and die were water-cooled. The punch base was also modified to allow rapid cooling or could be heated to decrease the cooling rate in the region of the sample in contact with the punch.

The formability test equipment consisted of a stationary punch mounted on the base of a Macrodyne hydraulic forming press, as shown in Figure 35. A binder surrounded the punch and was mounted on a hydraulic cushion to provide up to 355 kN of clamping force on the sample against the die. The binder featured spring-loaded fittings that enabled the transferred sample from the furnace to be accurately positioned and to prevent initial contact with the binder. This

minimized quenching prior to the forming stroke. The die was installed on a fast-approach 600 kN (60 ton) actuator that created the forming downstroke at 60 mm/s to complete the forming stroke before the formation of martensite in the sample. Vertical linear guide rails were installed on both sides of the die fixture.

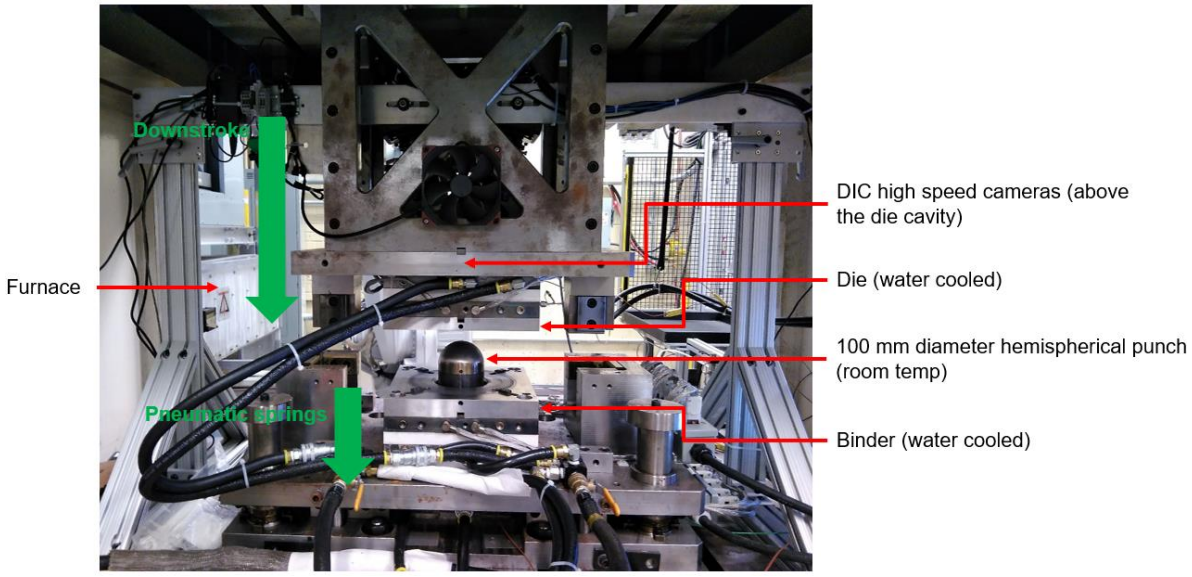

Figure 35: Nakazima dome test equipment setup in the forming press

The hot formability tests were performed using an automated system that included an austenitization furnace and a six degree-of-freedom (DOF) motion transfer robot integrated into the forming press, as shown in Figure 36. The transfer robot used pneumatic suction grippers to place the room temperature sample into the furnace. After austenitization, the other end of the transfer robot manipulator used steel retractable grippers to place the heated sample on the binder of the forming press.

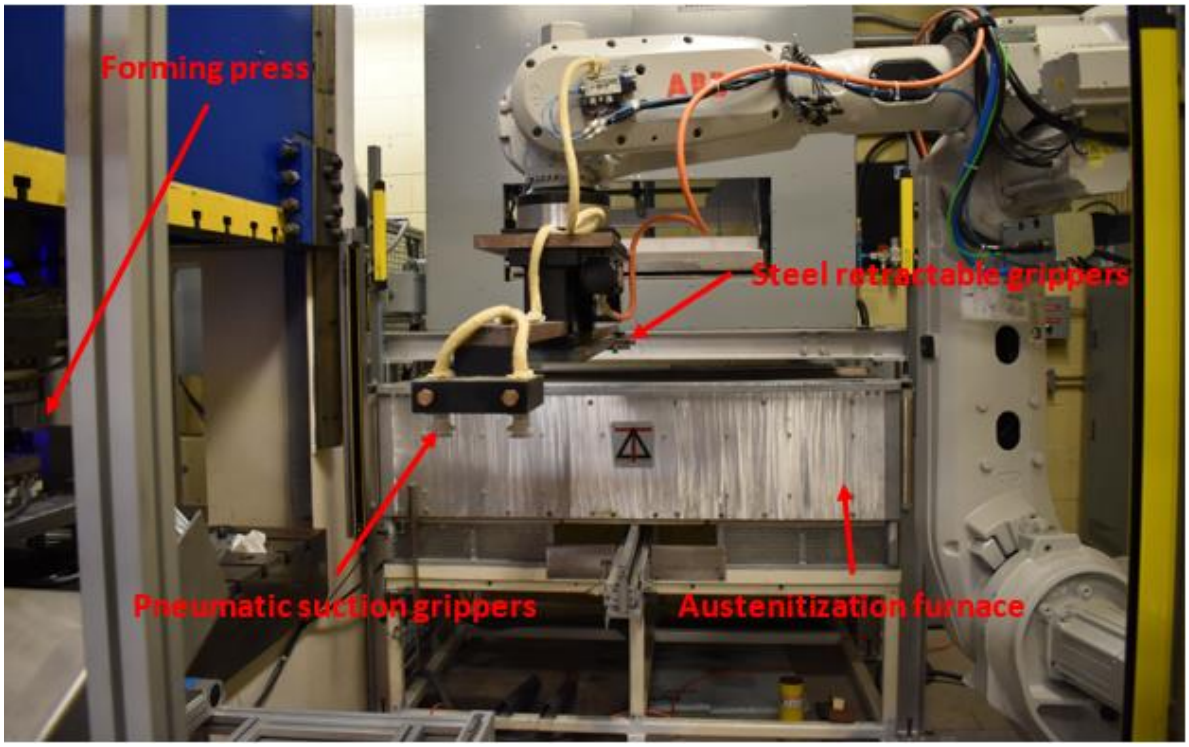

Figure 36: Automated austenitization furnace and transfer robot.

2.3.2. Formability Samples

Each PHS1800 Nakazima sample geometry followed the ISO12004-2 standard [55] with a constant shaft length of 25.4 mm, as shown in Figure 37. Each gage width aimed to produce a different ratio between major and minor strain.

The sample geometries of Figure 37 were laser cut and then manually deburred to reduce the chance of premature edge fracture during testing.

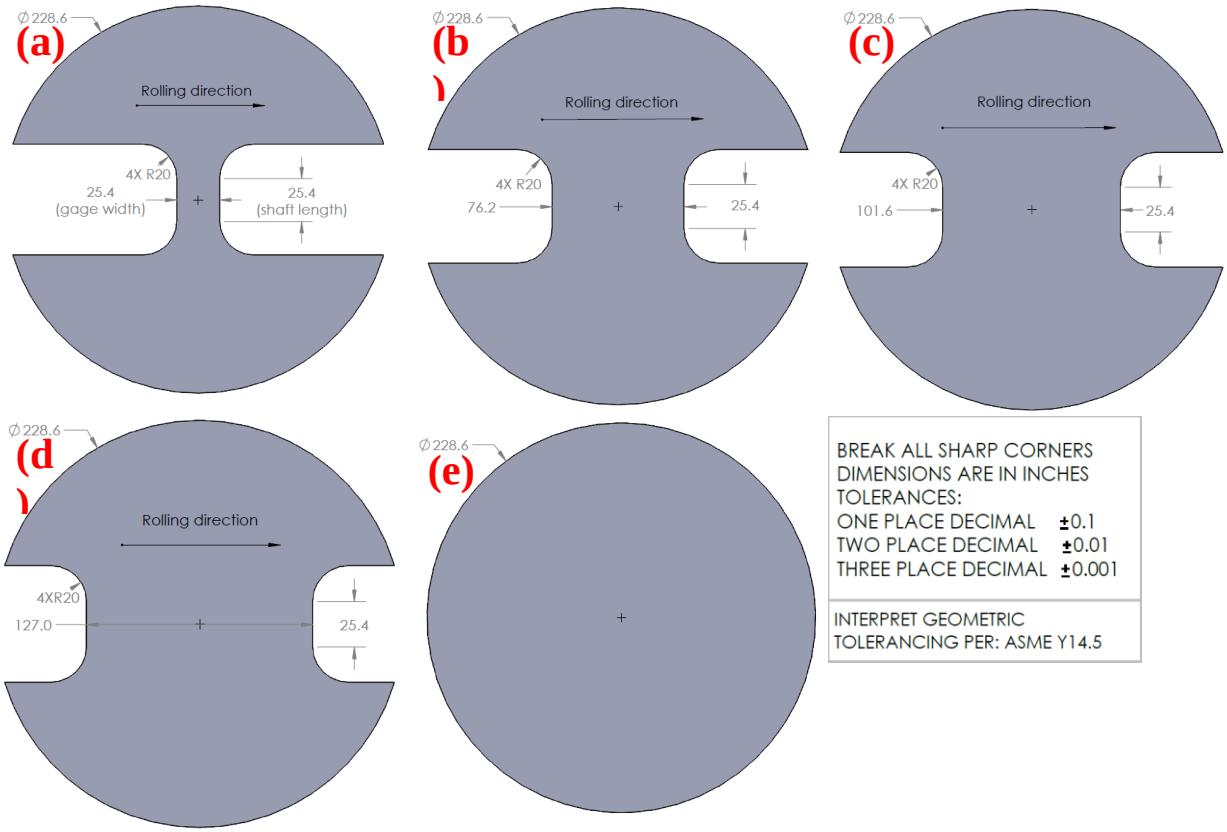

Figure 37: PHS1800 sample geometry used in Nakazima tests according to ISO12004-2. All geometries have a shaft length of 25.4 mm. Gage width: (a) 25.4 mm (b) 76.2 mm (c) 101.6 mm (d) 127.0 mm (e) Equibiaxial with 228.6 mm diameter circle.

To provide good adhesion of the painted speckle pattern on the Al-Si coated samples for digital image correlation (DIC) strain measurement, each sample was subjected to the coating pre-alloying treatment of Lu *et al.* [16]. The pre-alloying treatment consisted of holding the sample in a chamber furnace at a temperature of 700°C for 10 minutes. The sample was manually transferred to a pair of water-cooled flat steel plates in a hydraulic press and quenched. This thermal cycle created a dark gray background which provided good contrast against white paint speckles to track the deformation strain during the forming stroke as shown in Figure 38. It also created intermetallic microstructures that would not melt during austenitization. Without pre-alloy, the molten Al-Si layer would dissolve the white paint speckles and cause a blurry speckle pattern. Furthermore, the

conventional speckling method for room temperature tests, which involved a black painted background with white speckles or vice versa, resulted in cracking of the background paint during high-temperature deformation.

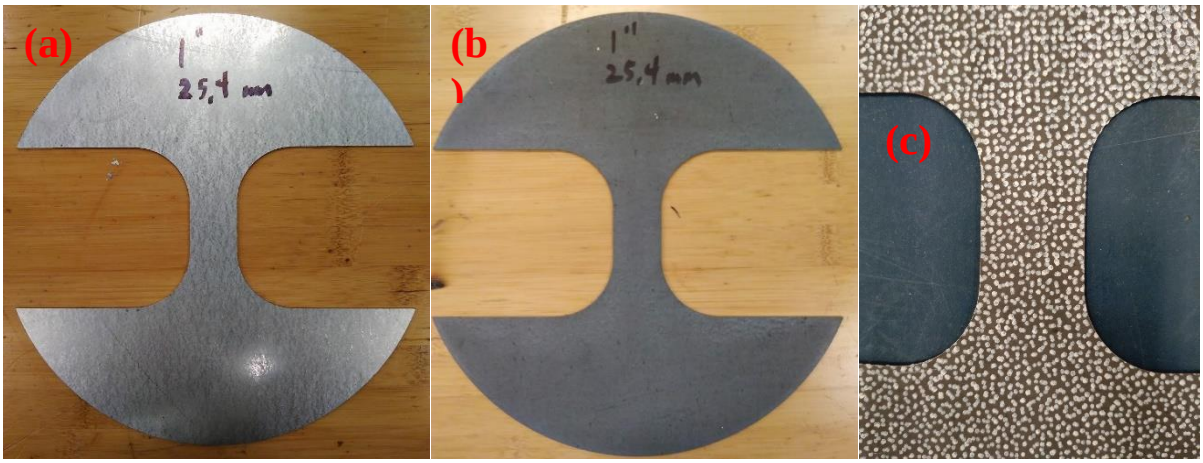

Figure 38: PHS1800 Nakazima dome test sample through its surface preparation process for DIC strain measurements. (a) After laser cutting to its 25.4 mm gage width geometry. (b) After the pre-alloying procedure. (c) After application of white paint speckles

Lu *et al.* [16] showed that the pre-alloying process did not have a significant impact on the tensile properties of PHS1800. Using a Gleeble thermal-mechanical test system, they reported that the tensile flow curves of specimens pre-alloyed at 700°C for 10 minutes followed by quenching were similar to those that were not pre-alloyed. These tests were performed at temperatures of 700°C and 800°C with strain rates of 0.5 s^{-1} and 1 s^{-1} [16].

2.3.3. Formability Test Procedures

The industrial direct hot stamping process was replicated by austenitization of the sample followed by rapid transfer from the furnace to forming press for the forming stroke. The entire test process was automated with sequential block diagrams in the LabVIEW control system.

Each pre-alloyed and speckled sample was first austenitized in the furnace at a temperature of 930°C for 5 minutes, as shown in Figure 39. The sample was then transferred from the furnace to the forming press. This process took about 14 seconds from the sample exiting the furnace to the start of the press cycle at a nominal speed of 60 mm/s, as shown in Figure 40.

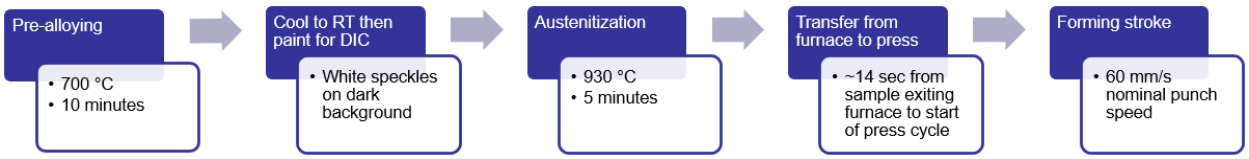

Figure 39: Formability testing process for each sample

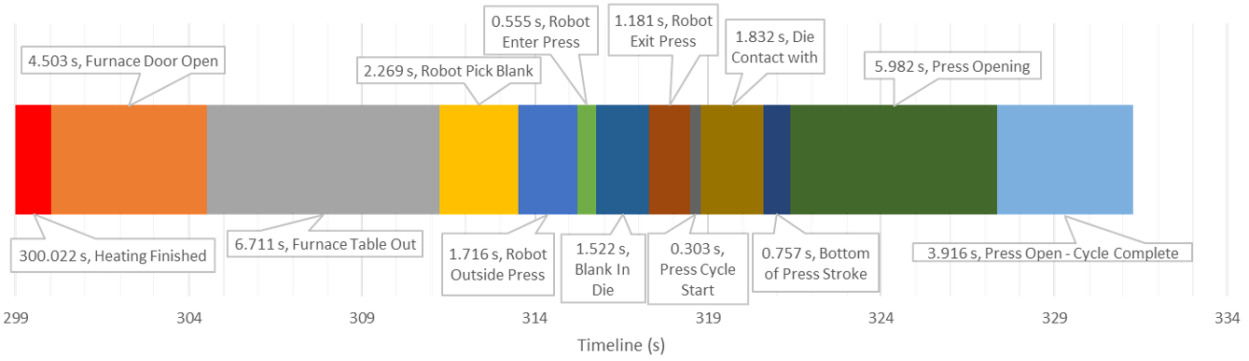

Figure 40: Events timing after 300 seconds of austenitization in the furnace. The transfer time required from the sample exiting the furnace to the start of the press cycle lasts about 14 seconds.

Figure 41 shows the measured forming stroke speed which attained a maximum of ~100 mm/s at the end of the forming stroke. An oscillatory response was seen in the press velocity, but given the monotonic nature of the press displacement and need for rapid forming, this press motion was deemed acceptable.

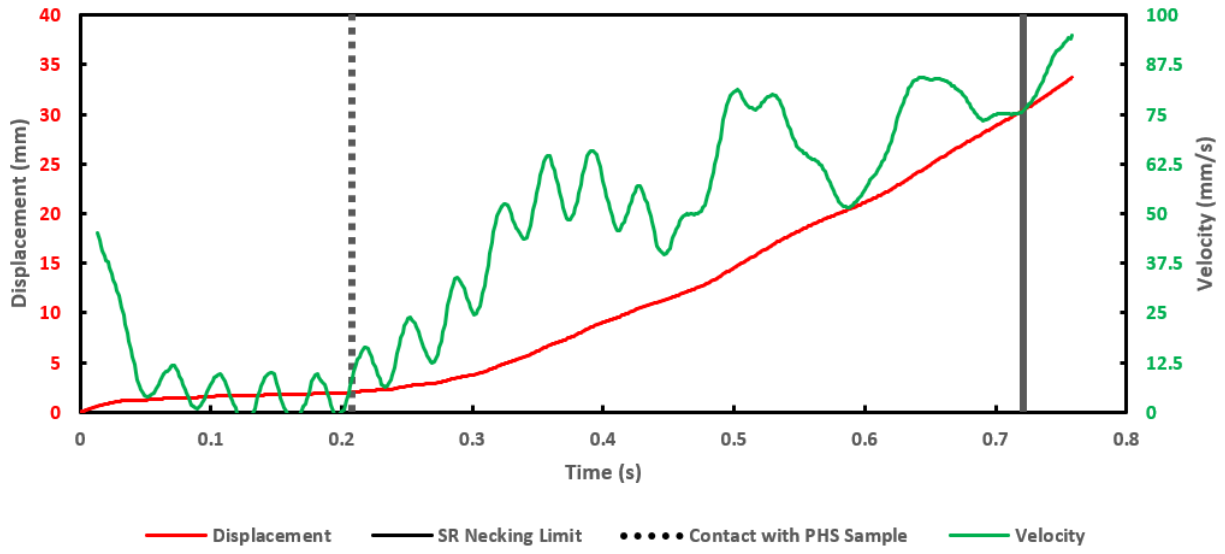

Figure 41: Velocity and displacement of the punch at the start of the forming stroke.

In the Marciniak and Hybrid punch tests, the center hole of the carrier blank prevented contact and quenching of the PHS sample. As the PHS sample was placed on the carrier blank and deformed in the forming stroke, it was expected to contact the entire surface area of the carrier blank except at the center of the samples. To further induce a temperature difference between the PHS sample's apex and its peripheral area in Marciniak and hybrid tests, a clamping time of 3 seconds was used prior to initiating die motion to quench the sample and carrier blank between binder and die. In the Nakazima tests, the punch temperature was increased to reduce the rate of temperature drop at the apex of the sample.

2.3.4. Temperature Measurement

A pyrometer was positioned above the die cavity and aimed at the specimen to monitor the blank temperature during forming. The pyrometer was calibrated against measurements from a reference thermocouple embedded in a number of setup samples. This calibration was performed using a flat PHS1800 sheet calibration sample that was clamped between flat steel plates for quenching during the forming stroke. According to Figure 42, the difference between thermocouple and pyrometer measurements was about 10°C, which was deemed sufficiently accurate for this research.

When the calibration sample was removed from the furnace during transfer, its temperature started to decrease from its austenitization temperature of 930°C, as shown in Figure 42. The temperature drop rate decreased, because the radiative and convective heat transfer rate between the sample and room temperature air decreased as the sample temperature decreased. After the calibration sample contacted the binder and the press motion was started, the rate temperature drop was similar to that for to the transfer phase. Since the center of the calibration sample was suspended above the die cavity, it did not contact any tooling and was not subjected to conductive heat transfer. As the pyrometer was aimed at the center of the sample, the die press motion did not have a significant impact on the measured temperature drop rate.

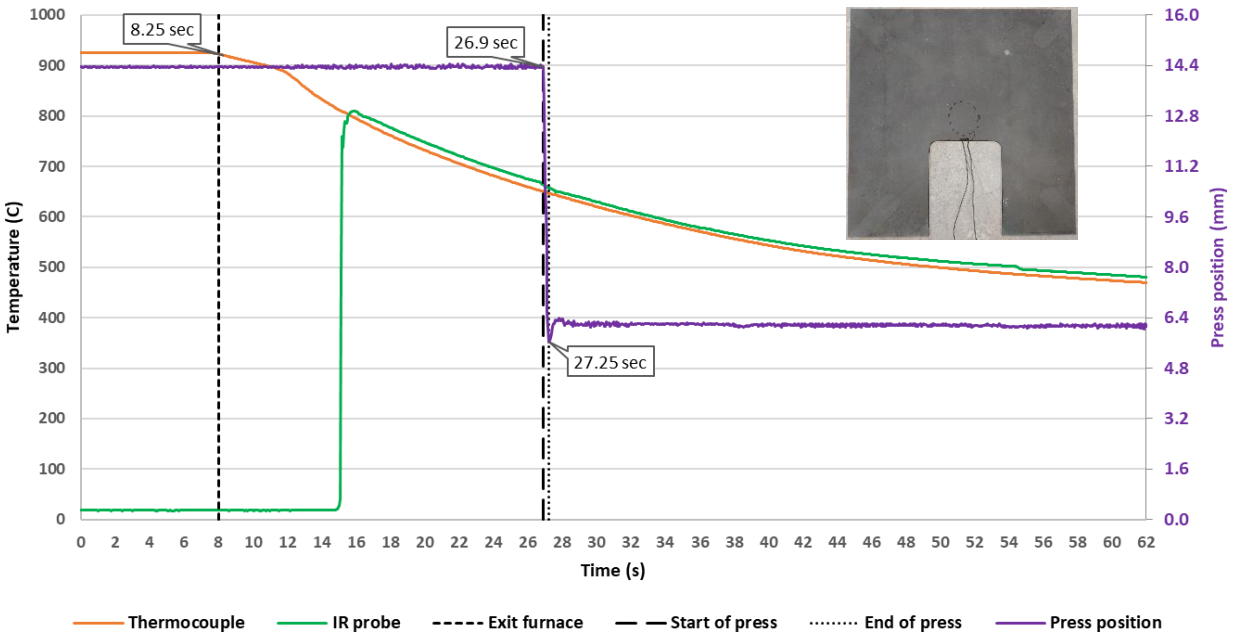

Figure 42: Calibration sample temperature evolution over time for pyrometer calibration. Measurements by the pyrometer (IR) are calibrated against reference thermocouples that are embedded in the sample.

2.3.5. Strain Measurement

Two Photron AX100 high-speed cameras were mounted above the die cavity to enable stereoscopic DIC strain measurement. The cameras had an image resolution of 1024 x 1024 pixels and were set to an imaging rate of 500 frames per second to record the forming stroke which lasted about 1 second. Nikon CP-12 62 mm polarizing lenses were attached to each camera to decrease reflection noise coming from the sample surface. To prevent the cameras from overheating, a 120 mm diameter fan was installed next to the cameras. Several DIC speckling methods were considered and are described in Appendix. The speckling methods for each type of formability test are summarized in Table 3.

Table 3: DIC analysis parameters for Nakazima, Marciniak, and hybrid formability tests

Formability test	Speckling method	Subset size	Step size	Filter size	Image scale
Nakazima	45° direct fire	29	7	7	0.116 mm/pixel
Marciniak	Tactical speckling	37	9	11	
Hybrid	Tactical speckling	37	9	11	

Using the DIC processing software Vic 3D, the deformation at the gage section was tracked to obtain the major and minor strains at each time frame. The first pair of images was the reference for all subsequent frames. The virtual strain gage (VSG) was 71 pixels which corresponded to 8.2 mm using equation (4).

$$VSG\ (pixel) = (filter\ size - 1) \times step\ size + subset\ size \quad (3)$$

$$VSGm\ (length) = VSG \times image\ scale \quad (4)$$

2.4. Marciniak Punch Heights at Necking Limit and Fracture

Since the Marciniak test tooling geometry remained the same for all PHS variants, the punch height attained at the necking limit constituted a metric for the material's formability. Figure 43 demonstrated the data analysis process used to obtain the corresponding punch height for each sample geometry of each PHS variant. This process used the same DIC parameters employed for the determination of necking limit strains. All major and minor strains were extracted at the center of each sample where necking occurred. Since each DIC frame was associated with a time stamp,

the frame corresponding to the necking limit indicated the time stamp when the punch reached the height that produced the onset of necking.

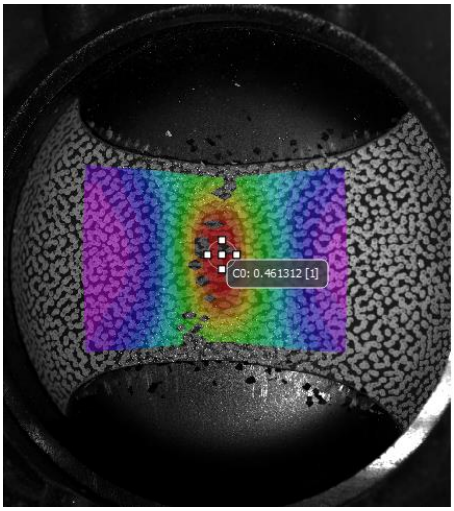

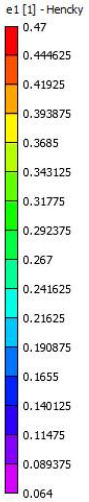

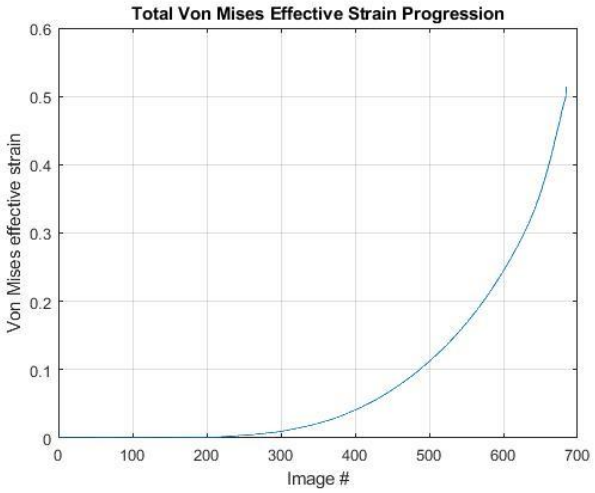

Set Target e_{eff}

- Determine major strain e_1 and minor strain e_2 at necking limit for each gage width.
- Compute total Von Mises effective strain: $e_{eff} = \sqrt{\frac{2}{3}(e_1^2 + e_2^2 + e_3^2)}$
- Assume a homogeneous strain state through thickness*: $e_3 = -(e_1 + e_2)$
- Assume linear strain paths for Marciniak punch geometry: $e_{effective} \approx e_{equivalent}$

* Since the apex of each sample does not contact the punch, and bending is negligible at the apex, the strain distribution through all layers of the material is near homogeneous

Extract Data at Sample Apex

- Obtain strain path at the necking location (apex) through DIC data. The DIC processing parameters are identical to those used to calculate the necking limit strains.
- Apply a moving average filter around 20 data points to the extracted e_{eff}
- Locate the DIC image # that features the closest e_{eff} to the target necking limit e_{eff} for the corresponding gage width

Determine Punch Height at Necking Limit

- Use the press position during the 3 seconds clamping prior to forming as the default 0 mm punch position
- Determine the punch height at necking by finding the punch position of the DIC image # at necking limit e_{eff}

Figure 43: Process to determine punch height at the necking limit strain.

Visible fracture in the DIC images was used to identify the end of the test, as shown in 44. The same procedure to obtain the height at necking was applied to calculate the height at fracture.

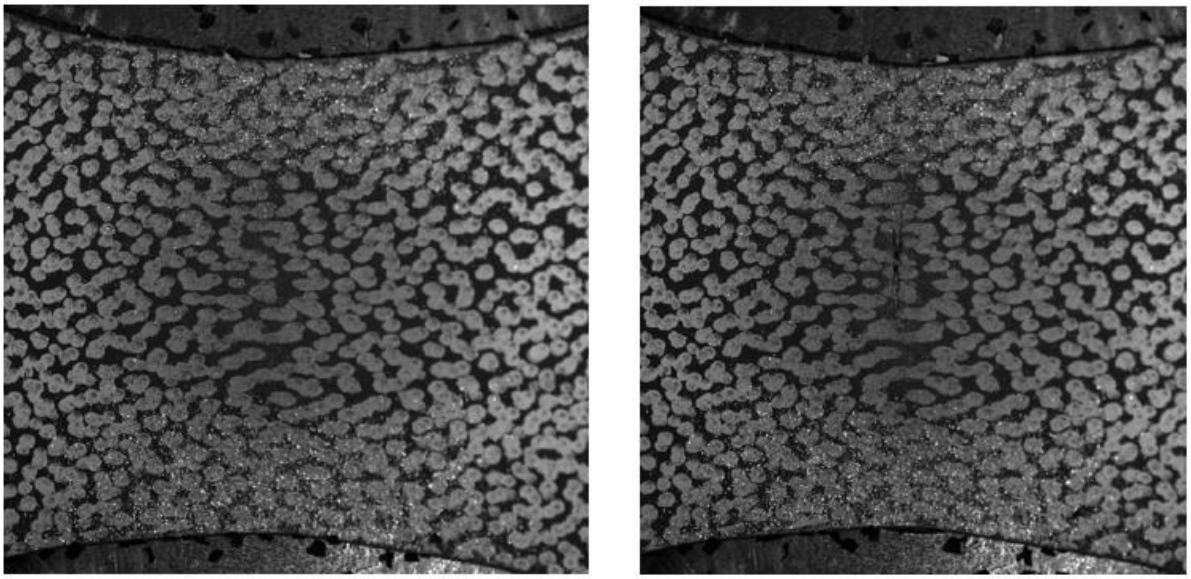

Figure 44: Detection of initial fracture.

3. Numerical Modelling of Formability Testing

The direct hot stamping process in this work was modelled with the LS-Dyna R11.0 commercial simulation software, which was commonly used by industry for metal forming and crashworthiness analysis. In the Nakazima, Marciniak, and hybrid formability tests, the tooling and sample geometries were modelled with shell and solid elements. Since extensive material deformation and heat transfer occurred simultaneously, an explicit dynamic time integration scheme for mechanical deformation was coupled with an implicit time integration scheme for heat transfer. Hypermesh software was used to mesh the geometry of the tooling and sample.

The simulated austenitization process increased the PHS sample temperature and generated thermal expansion. To represent the transfer process, the sample was first cooled to its initial forming temperature. The austenitized PHS sample was then deformed during the forming stage with the same parameters used in experimental tests. The objective of the simulations was to investigate the cause of undesirable necking locations and to evaluate different process conditions to resolve it.

3.1. Model Geometry

The hot stamping Nakazima, Marciniak, and hybrid Nakazima-Marciniak tests of PHS1800 were numerically represented with geometries meshed using Hypermesh and simulated using LS-DYNA.

3.1.1. Nakazima Punch Simulation

The Nakazima model contained the austenitized PHS sample, punch, binder, and die as shown in Figure 45. To reduce computational cost, the tooling and PHS sample were modelled using quarter symmetry along the vertical axes of symmetry. Each tooling component, shown in Figure 45, was represented by two numerical entities: a 2D rigid shell mesh to discretize the contact surface and a 3D solid mesh for its internal volume used to model heat transfer.

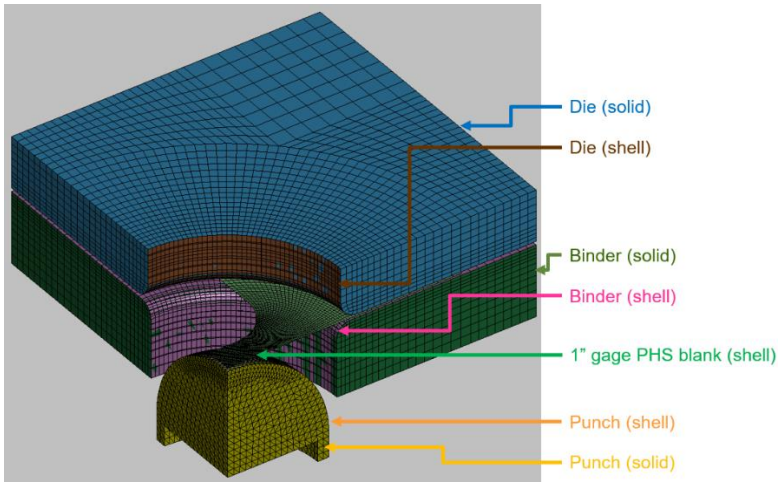

Figure 45: Finite element mesh used to model the Nakazima dome test.

The deformable PHS sample was meshed using fully integrated shell elements with seven through-thickness integration points. A higher mesh density was used toward the center of the sample, as shown in Figure 46. The shell thickness was set to 1.6 mm, corresponding to the sheet metal thickness. Since deformation was expected to localize at the apex of the punch, a higher mesh density at the apex provided higher resolution. The lower mesh density toward the periphery of

the sample caused minimal compromise in model resolution, because the peripheral area was clamped between binder and die and was subject to minimal deformation.

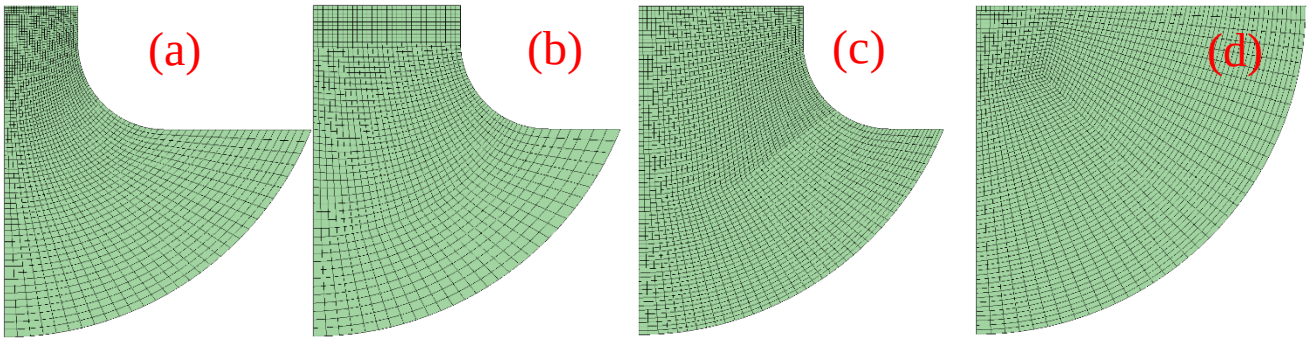

Figure 46: 2D quad shell mesh for PHS sample with gage widths of (a) 50.8 mm (b) 101.6 mm (c) 114.3 mm (d) 228.6 mm diameter.

3.1.2. Marciniak Punch Simulation

The model of the Marciniak test used the same tooling components as the Nakazima test, except for the punch geometry and mild steel carrier blank as shown in Figure 47. The carrier blank was also meshed using fully integrated shell elements with seven through thickness integration points.

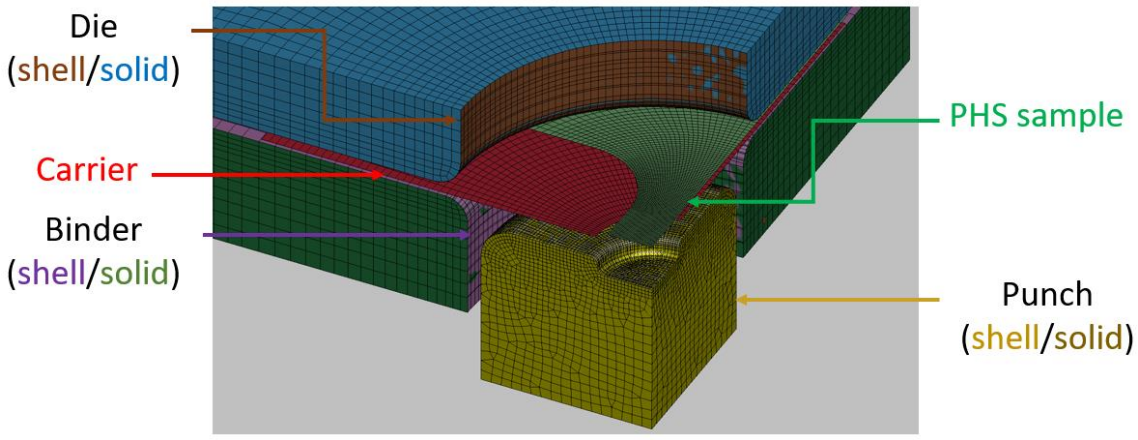

Figure 47: Mesh pattern to model the Marciniak test.

3.1.3. Hybrid Nakazima-Marciniak Punch Simulation

The hybrid Marciniak-Nakazima test simulation was identical to the Marciniak test simulation except for the punch geometry, as shown in Figure 48. Like the Marciniak test setup, the flat top section of the hybrid punch was initially positioned 6 mm away from the carrier blank surface to prevent premature contact.

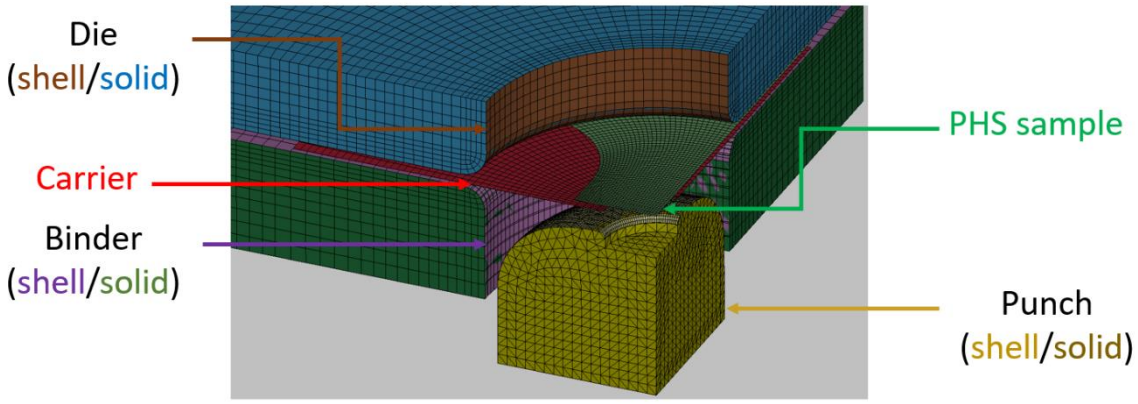

Figure 48: Mesh pattern to model the hybrid Marciniak-Nakazima test.

3.2. Material Models

Each component in a formability test was assigned with its corresponding material properties to simulate realistic deformation behaviors.

3.2.1. Rigid Tooling Material Model

The tooling components, which were the punch, die, and binder, were rigid with thermal properties corresponding to steel. All rigid body tooling components were made of steel with an elastic modulus of 207 GPa.

3.2.2. Press Hardened Steel Material Model

The PHS sample was modelled using a temperature and strain rate dependent constitutive model available in LS-DYNA (*MAT_106_ELASTIC_VISCOPLASTIC_THERMAL). The adopted true stress-plastic strain curves corresponded to the modified Norton-Hoff equations (5) to (7) with coefficients for PHS1800 developed by Lu *et al.* [16] and listed in Table 4. The fits were based on experimental flow curves, shown in Figure 49, obtained by Lu *et al.* [16]. They cover a temperature range from 600°C to 900°C and strain rates from 0.01 s^{-1} to 2 s^{-1}. LS-DYNA interpolated between these input curves to determine the instantaneous flow stress σ. The elastic modulus was also modelled as a function of temperature, as described by Lu *et al.* [16].

$$\sigma(\varepsilon_p, \dot{\varepsilon}, T) = A \cdot e^{\beta/T} \cdot (b + \varepsilon_p)^n \cdot \dot{\varepsilon}^m \tag{5}$$

$$n(T) = n_1 \cdot T^2 + n_2 \cdot T + n_3 \tag{6}$$

$$m(T) = m_1 \cdot T^2 + m_2 \cdot T + m_3 \tag{7}$$

ϵ_p is plastic true strain. $\dot{\epsilon}$ is strain rate. T is material temperature.

Table 4: Coefficients for modified Norton-Hoff equations for PHS1800 hardening curves by Lu et al. [16]

A (MPa s^m)	B (K)	b	n_1 (K^{-2})	n_2 (K^{-1})	n_3	m_1 (K^{-2})	m_2 (K^{-1})	m_3
27.60	2677.42	0.0022	2.36e-6	-4.82e-3	2.64	2.05e-7	-2.03e-4	8.16e-2

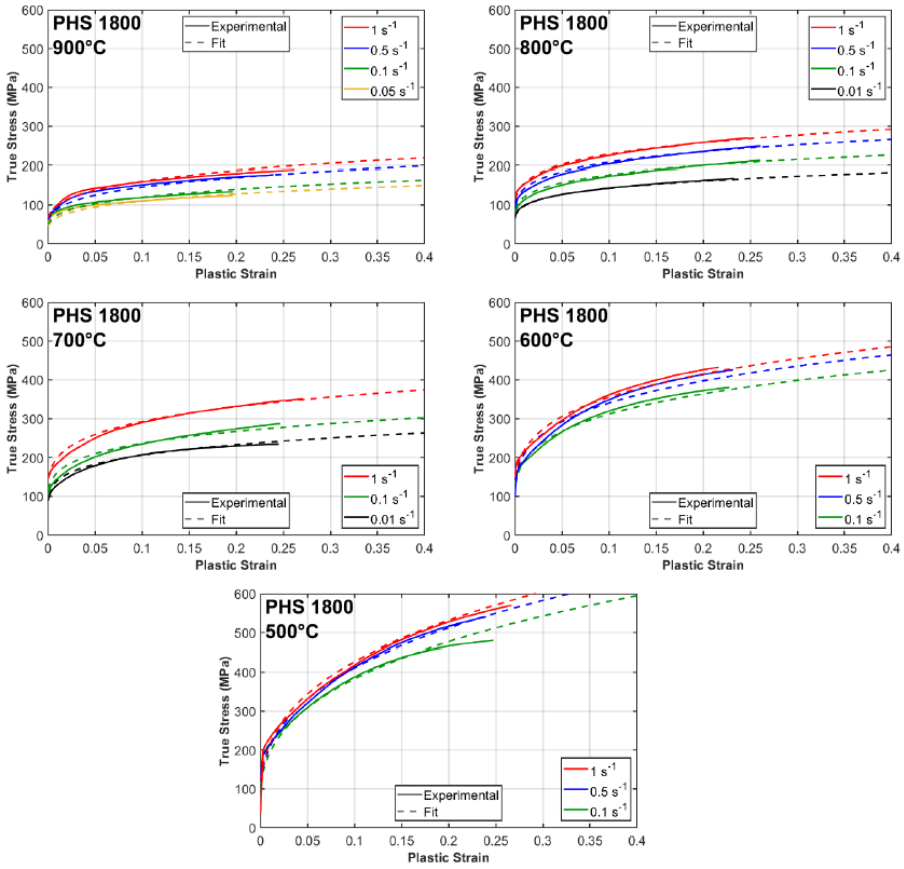

Figure 49: True stress-plastic strain flow curves of PHS1800 under various temperatures and strain rates by Lu et al. [16]

3.2.3. Carrier Blank Material Model

The carrier blank was also modelled with the LS-DYNA material card *MAT_106_ELASTIC_VISCOPLASTIC_THERMAL. The 2 mm thick mild steel sheet was assumed to have a pearlite-ferrite microstructure. Thus, its material model was based on the

constitutive model developed by Li et al. [57]. The flow curves from equation (8) are shown in Figure 50.

Johnson-Cook model for flow stress σ of ferrite - pearlite microstructure by Li et al. [57] with its material coefficients provided in Table 5:

$$\sigma = f_1(\dot{\epsilon}, T) + f_2(T)(\epsilon - \epsilon_0)^{f_3(T)} \tag{8}$$

$$f_1(\dot{\epsilon}, T) = A - B\left(\frac{T}{T_0}\right) - C * \ln\left(\frac{\dot{\epsilon}}{\dot{\epsilon}_0}\right) - D\left(\frac{T}{T_0}\right)^2 + E\left[\ln\left(\frac{\dot{\epsilon}}{\dot{\epsilon}_0}\right)\right]^2 + F\left(\frac{T}{T_0}\right)\ln\left(\frac{\dot{\epsilon}}{\dot{\epsilon}_0}\right) \tag{9}$$

$$f_2(T) = \frac{G}{1 + e^{\left[H\left(\left(\frac{T}{T_0}\right) - I\right)\right]}} \tag{10}$$

$$f_3(T) = J - K\left(\frac{T}{T_0}\right) \tag{11}$$

ϵ is true strain. $\dot{\epsilon}$ is strain rate. T is material temperature. T_0 is the lowest quasi-static test temperature at 293 K. $\dot{\epsilon_0}$ is quasi-static test strain rate at 0.001 s^{-1}. ϵ_0 is 0.002 true strain.

Table 5: Coefficients for Johnson-Cook model equations for flow stress of ferrite-pearlite microstructure by Li et al. [57]

$\dot{\epsilon}$	T_0	A	B	C	D	E	F	G	H	I	J	K
0.001	293	449.8064	48.5971	20.4355	16.0959	2.2521	4.2453	876.7807	3.6692	2.8341	0.8839	0.1214

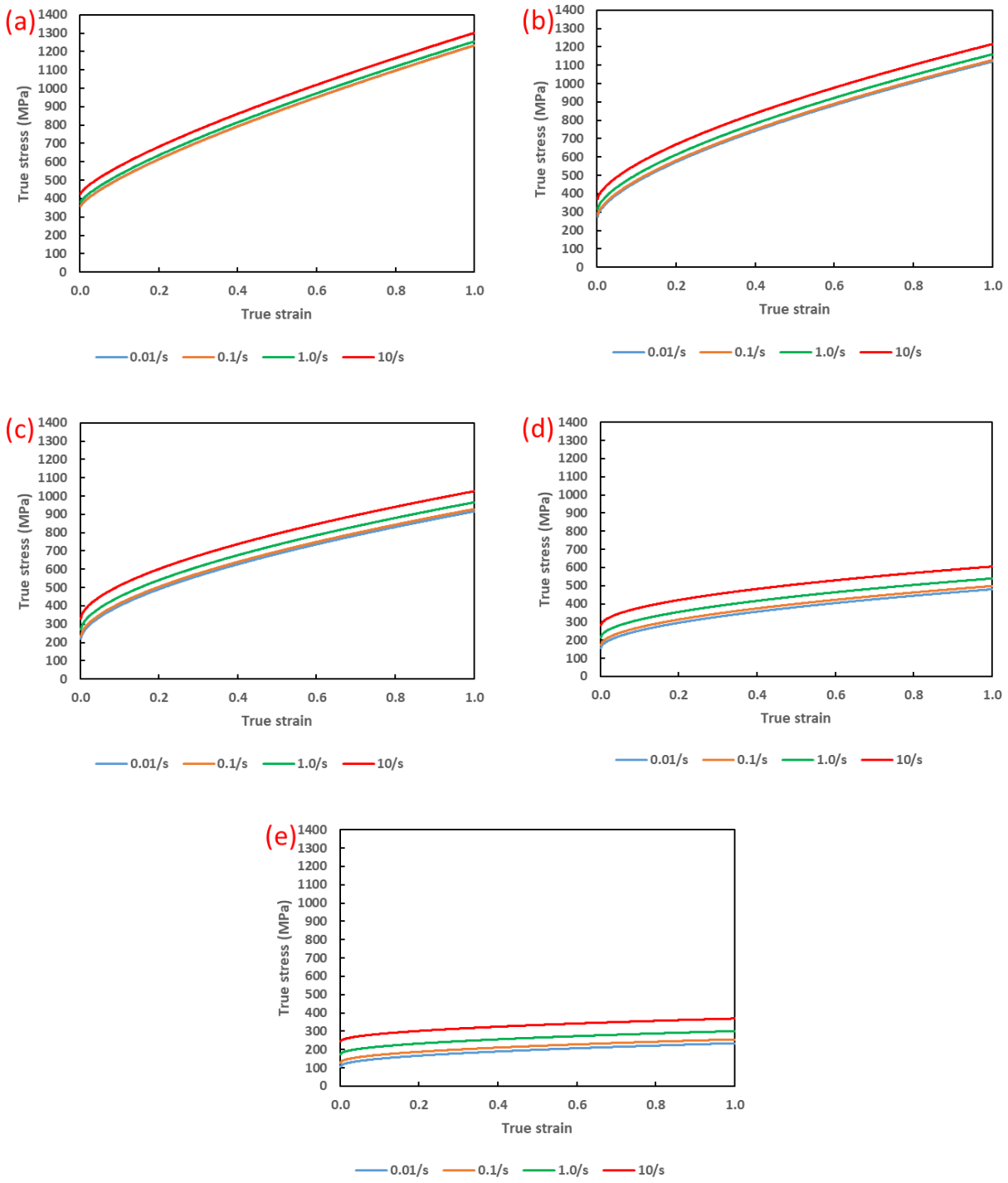

Figure 50: Flow curves for pearlite-ferrite microstructure of mild steel at strain rates of 0.01, 0.1, 1.0, and 10 s^{-1}. These are defined at temperatures: (a) 20°C, (b) 300°C, (c) 450°C, (d) 600°C, (e) 700°C.

3.3. Boundary Conditions and Contact Treatment

The binder force applied in the simulations was 88,750 N, which corresponded to a quarter of the total clamping force of 355,000 N. An average CoF of 0.294 from Section 4.3 was applied to all tooling-PHS1800 contact surfaces and prevented material drawing into the die cavity.

A penalty function-based contact treatment was enforced between contacting bodies. Typically, the sheet metal was designated a "slave surface", while the tooling was designated the "master surface". During contact, any slave node that penetrated a master element was repelled by an interface force $\overrightarrow{F_n}$ in a direction normal $\vec{n}$ to the master element according to equation (12).

$$\overrightarrow{F_n} = -(l * k_i)\vec{n} \tag{12}$$

In equation (12), l represented the magnitude of the penetration of the slave node, and k_i was the penalty stiffness. To prevent motion instabilities caused by a large penalty stiffness, a scale factor of 0.1 was applied to the penalty stiffness k_i [58]. The interface force was also used to calculate the frictional force which resisted tangential sliding along the contact interface.

3.4. Thermal Properties

The heat transfer model accounted for natural convection and radiation for cooling of the blank in air along with conduction between the blank and tooling. The conduction heat transfer coefficients were defined as a function of contact pressure in Table 6 according to George [59].

Table 6: Conduction heat transfer coefficients [59]

Contact Pressure [MPa]	Conduction Heat Transfer Coefficient [W/m^{2}K]
0	400
3	650
5	900
10	1000
20	2200
40	3000

Prior to contact, the PHS sample transferred heat to the tooling components and ambient room temperature air through convection and radiation. These effects were combined to create effective HTC, shown in Table 7, that were dependent on temperature and independent from interface conduction.

Table 7: Effective HTC for convection and radiation [60]

Temperature (°C)	Effective Heat Transfer Coefficient [W/m^{2}K]
50	11.0
500	41.5
600	53.5
700	67.8
800	85.1
900	106.0
1000	129.0

3.5. Tooling Motion

In each formability test, the punch was fixed in place while the die motion was controlled by the press. The binder acted under force control and moved with the die while clamping the blank to the die. The model initialized contact by first applying the binder force which clamped the PHS sample against the die. For the Marciniak and hybrid punch models, a clamping time of 3 seconds was enforced prior to the start of the forming stroke. A clamping period was not considered in the Nakazima models. Prescribed velocity of the die followed a cosine acceleration up to a speed of 1.4 mm/sec, as shown in Figure 51, followed by deceleration to a stationary position. The Marciniak and hybrid punches were initially offset by 6 mm from the carrier blank's surface to prevent premature contact. No offset was used in the Nakazima tests.

3.5.1. Die Motion

To minimize vibrational instability associated with sudden motion of the die, which could result in rebound or "bounce" of the binder, the prescribed velocity of the die followed a cosine acceleration up to a speed of 1.4 mm/sec, as shown in Figure 51. It was then followed by deceleration to a stationary position. This approach avoided having the die impacting the PHS sample at high speed and promoted stable clamping of the PHS sample.

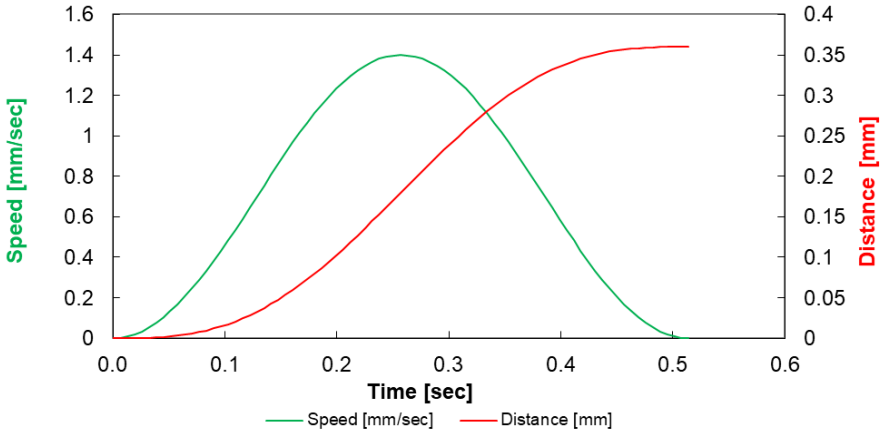

Figure 51: Speed and distance travelled by the die at the start of the simulation to clamp the PHS sample between the die and binder. The speed profile follows a cosine curve with a peak of 1.4 mm/sec.

3.5.2. Punch Motion

Since the clamping impact of the binder induced vibration in the PHS sample, the punch was initially offset by 6 mm from the carrier blank's surface to prevent premature contact.

In the Nakazima tests, the punch immediately contacted and deformed the PHS sample upon die closure. This process is shown in Figure 52.

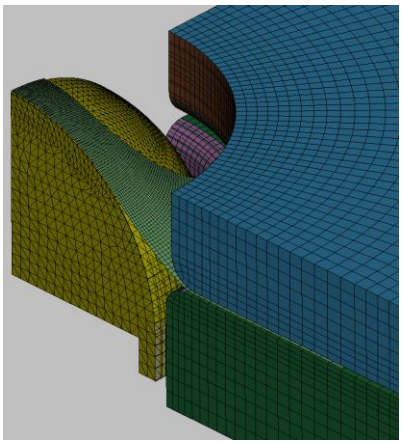

Figure 52: Deformation of the 25.4 mm gage width PHS sample in Nakazima testing during the forming stroke at a punch displacement of 33 mm.

After 3 seconds of clamping in the Marciniak and hybrid tests, the punch started to move into striking position by following a cosine speed profile with a maximum of 10 mm/sec, as shown in Figure 53. However, the Nakazima tests did not involve any clamping delay prior to the forming stroke.

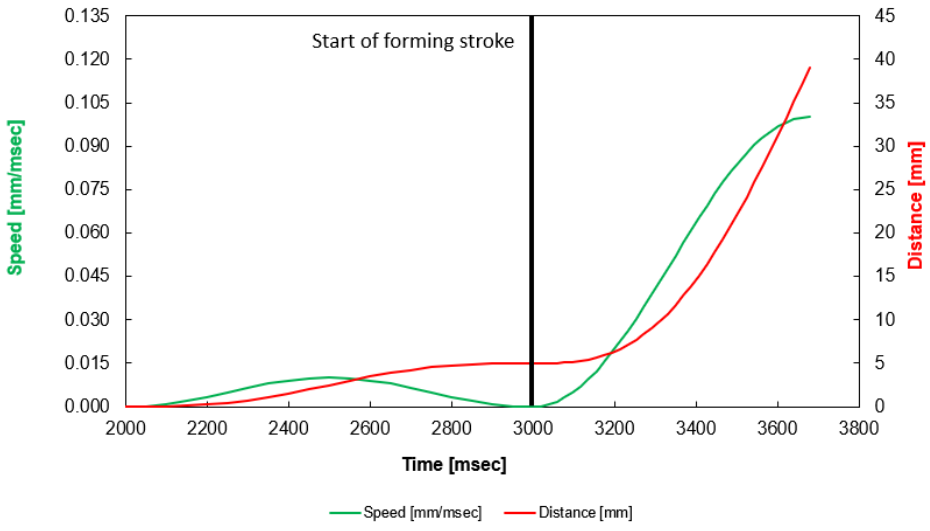

Figure 53: Speed and distance travelled by the punch after a clamping time of 2 seconds. The top surface of the punch, initially 5.8 mm below the surface of the binder, advances by 5 mm until the start of the forming stroke after a clamping time of 3 seconds. Then, it accelerates to a maximum speed of 100 mm/s (0.1 mm/msec) following a cosine curve toward the end of the forming stroke.

During the forming stroke after a clamping time of 3 seconds, the punch deformed the carrier blank and PHS sample as shown in Figure 54 for the Marciniak tests, and in Figure 55 for the hybrid tests. The model predictions are described in greater detail in Chapter 6 of this thesis.

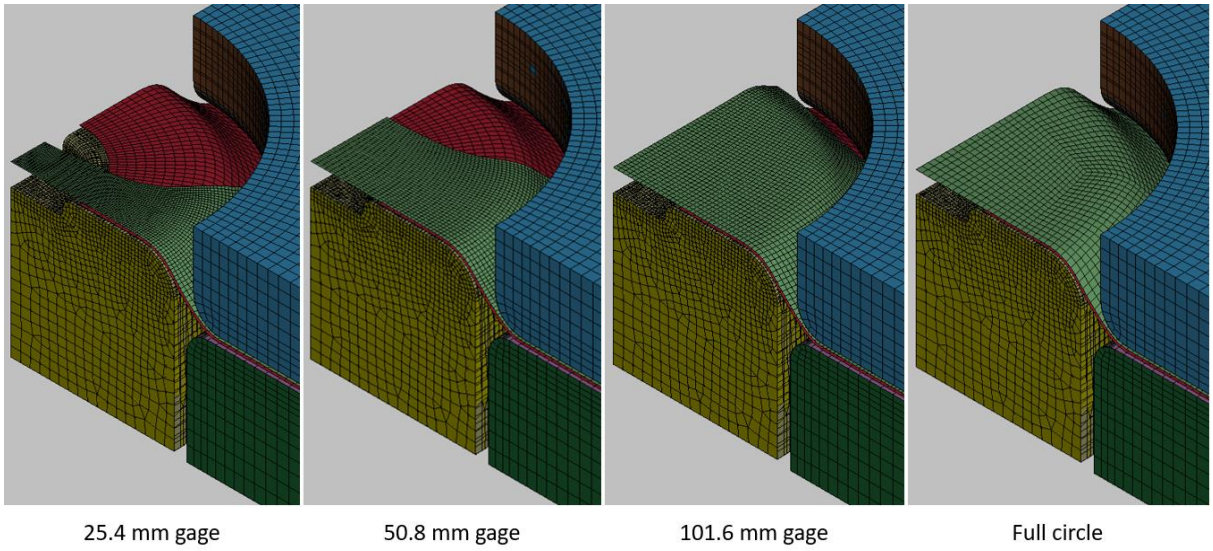

Figure 54: Deformation of the PHS sample and carrier blank in Marciniak testing during the forming stroke at a punch displacement of 16 mm.

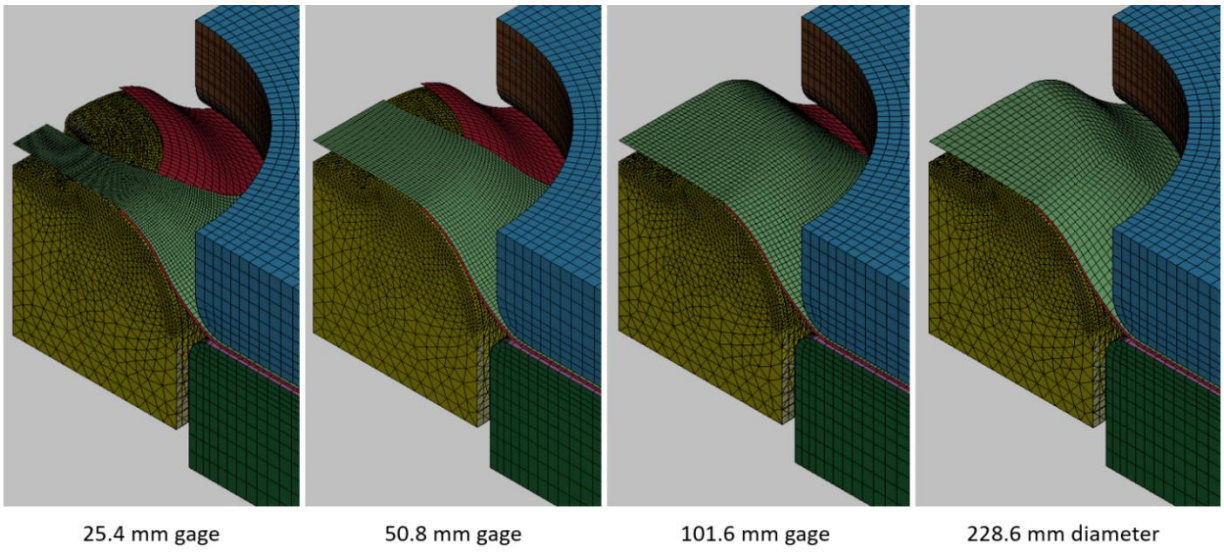

Figure 55: Deformation of the PHS sample and carrier blank in hybrid Marciniak-Nakazima testing during the forming stroke at a punch displacement of 23 mm.

3.6. Initialization of Blank Thermal Expansion

The PHS sample experienced a temperature increase in the furnace. Then, it experienced contraction due to cooling during transfer to the press. In the current model, the austentization process was not modelled. Instead, the blank was initialized by simulating a temperature increase from 300 K (27°C) at room temperature to a temperature of 1150 K (877°C) immediately prior to the start of the forming operation using a coupled structural thermal analysis. This pre-forming temperature of 877°C corresponded to the measured temperature of the PHS sample after the transfer process from the furnace to the forming press. The PHS material model did not consider any phase changes and associated the strain rate dependent flow curves to each temperature value (Section 3.2). Since only thermal expansion occurred during heating, the pre-heating simulation iterated using an implicit time integration scheme with a time step of 0.05 seconds for a total duration of 1 second. As shown in Figure 56, the austenitization stage outputted the initial uniform temperature distribution and thermally expanded geometry of the PHS sample, which were necessary inputs to accurately simulate the forming stroke.

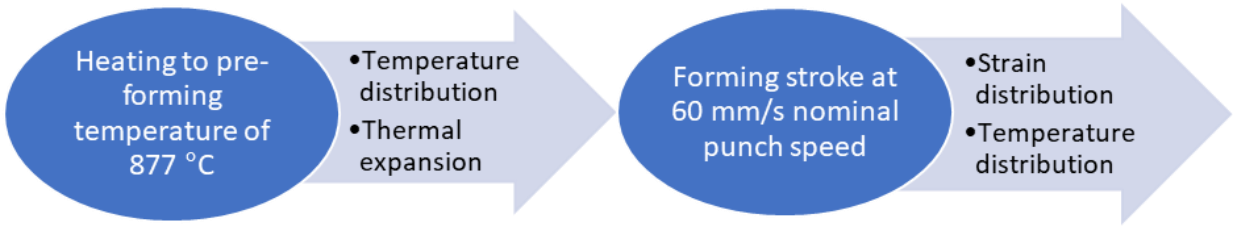

Figure 56: Simulation process to initialize thermal expansion prior to forming stroke

4. Friction Characterization: Results and Discussion

This chapter presents the results from the TCT friction characterization of PHS1800, PHS1500 (AS150), and PHS1500 (AS80) under hot stamping conditions. This data includes specimen/friction cup surface roughness, temperature history of a specimen during friction, effects of sliding speed/contact pressure on the coefficient of friction, and effects of tool wear on test data.

4.1. Surface Roughness of PHS Specimens

Before austenitization, the Al-Si coated PHS1800 specimens had a reflective metallic surface finish (Figure 57a). After austenitization and die quenching heat treatments, the surface became dark and matte (Figure 57b). Wear marks, where the Al-Si coating was removed (Figure 57c), were present on each specimen following friction testing.

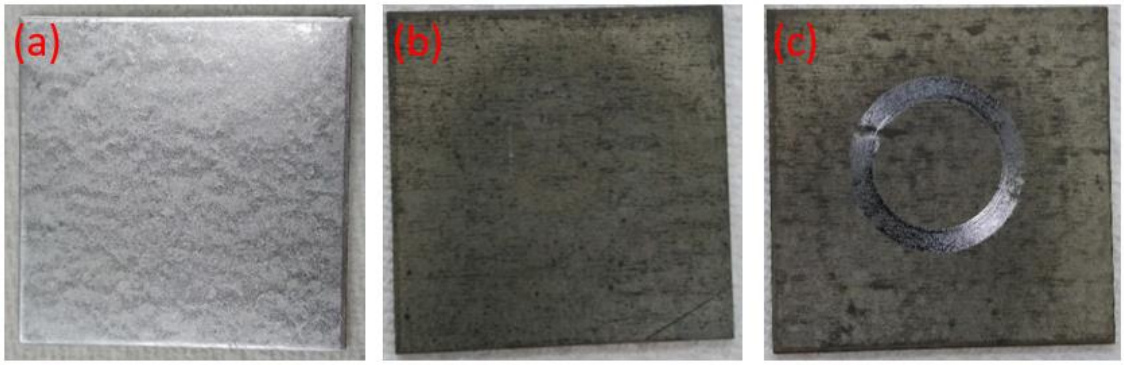

Figure 57: Al-Si coated PHS1800 specimen used in TCT friction testing: (a) Initial condition. (b) After heat treatment. (c) After friction testing

The average surface roughness was obtained from five measurements taken across a specimen (Figure 58b&c) using a contact profilometer. The Ra values corresponded to the arithmetic average distance from the surface peaks or valleys to the mean surface profile (Figure 58a). The average surface roughness increased from 1.26 µm in the as-received condition to 2.76 µm Ra after heat treatment, as shown in Table 8.

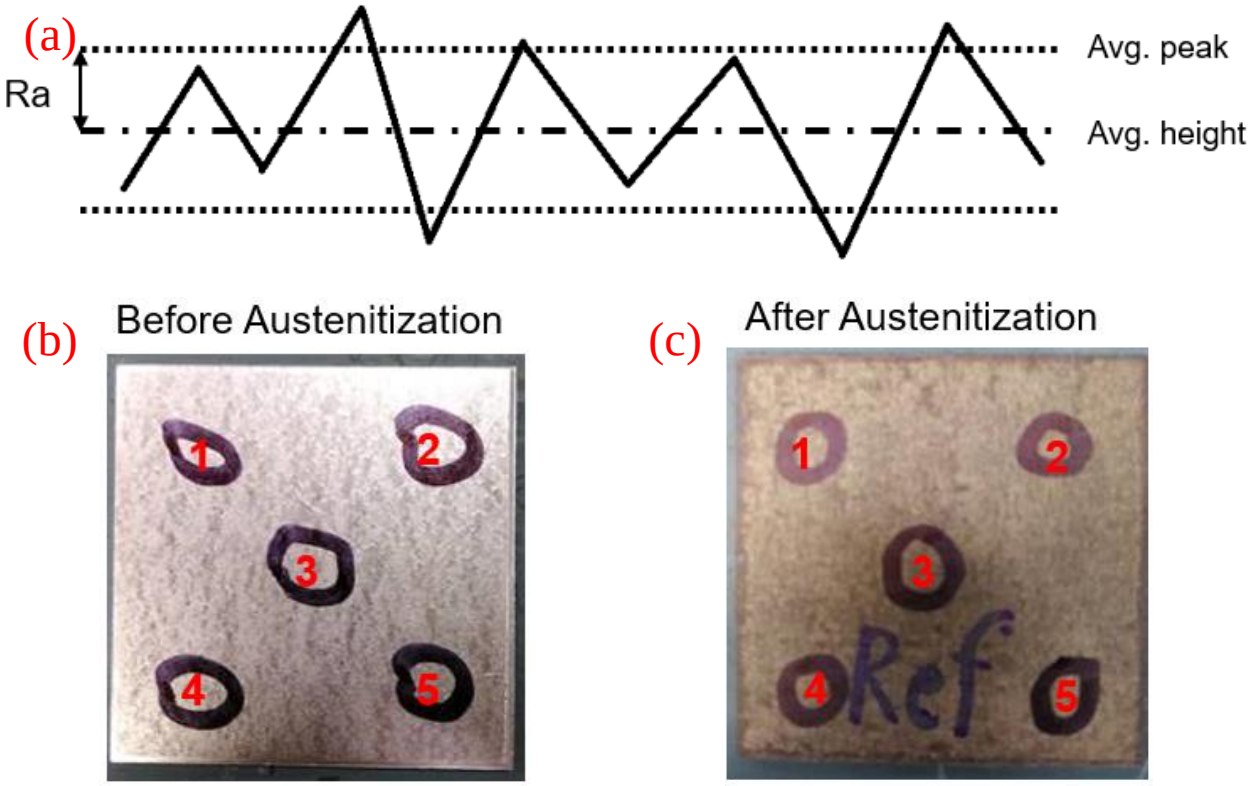

Figure 58: (a) Definition of Ra used to quantify surface roughness. The Ra value corresponds to the distance between the average height of all peaks or valleys and the average peak position. (b) Surface of an Al-Si coated PHS1800 specimen prior to austenitization. The average Ra value is obtained among 5 measurement locations. (c) Surface after austenitization showing measurement locations.

Table 8: Surface roughness of Al-Si coated PHS1800 before and after austenitization.

	Before Austenitization (Ra)	**After Austenitization (Ra)**
Average	1.26 µm	2.76 µm
Sample Standard Deviation	0.08 µm	0.34 µm
Difference	1.50 µm	

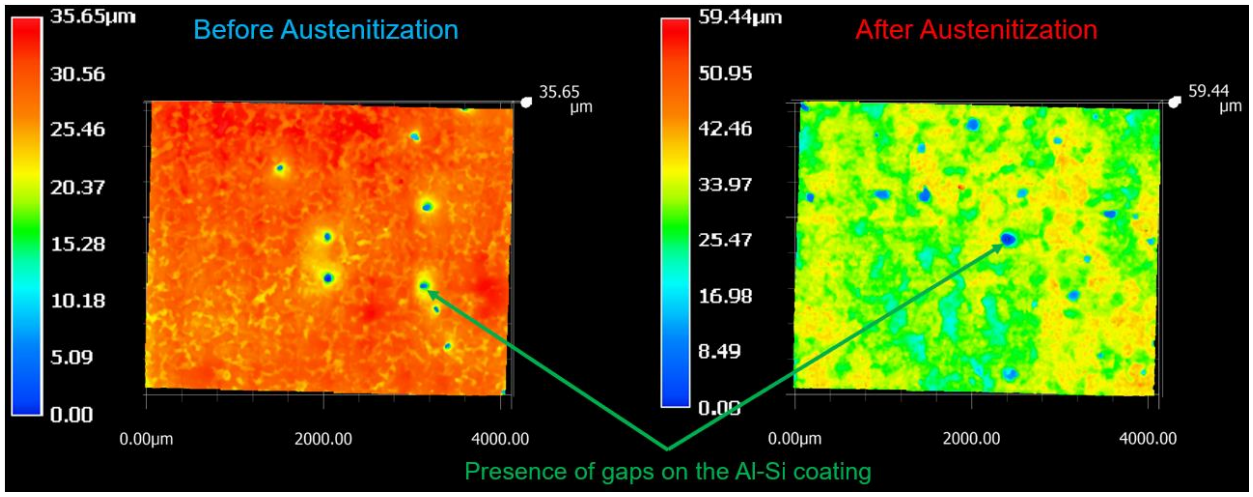

Figure 59: Surface height of Al-Si coated PHS1800 before and after austenitization. Gaps in the Al-Si coating are present before and after austenitization. They extend to the base metal, which is measured to be a common surface profile height.

4.2. Specimen Temperature History during TCT

This section presents temperature measurements used to validate the thermal history of the TCT samples in hot stamping. Two measurement techniques were considered, as presented in the following: contact between the thermocouple and the specimen contact area was achieved through a spring-loaded clamp and by embedding the thermocouple inside the thickness of a specimen.

4.2.1. Thermal History Measured Using the Spring-Loaded Thermocouple

This section presents the recorded thermal histories using the spring-loaded thermocouple (Section 2.2.4.1) at a sliding speed of 20 mm/s and a contact pressure of 30 MPa, along with measurements using the thermocouple welded to the specimen edge.

The measured temperature histories from the two locations on the sample are shown in Figure 60. The reference thermocouple at the specimen edge indicated that the austenitization temperature was reached within 130 seconds after insertion into the furnace. During the test, the spring-loaded thermocouple heated up to a maximum of 517°C below the friction area. In contrast, the reference thermocouple near the edge measured 653°C away from the contact area. Despite the contact of the spring-loaded thermocouple against the specimen surface, the response time was inadequate, and this measurement approach was not pursued further.

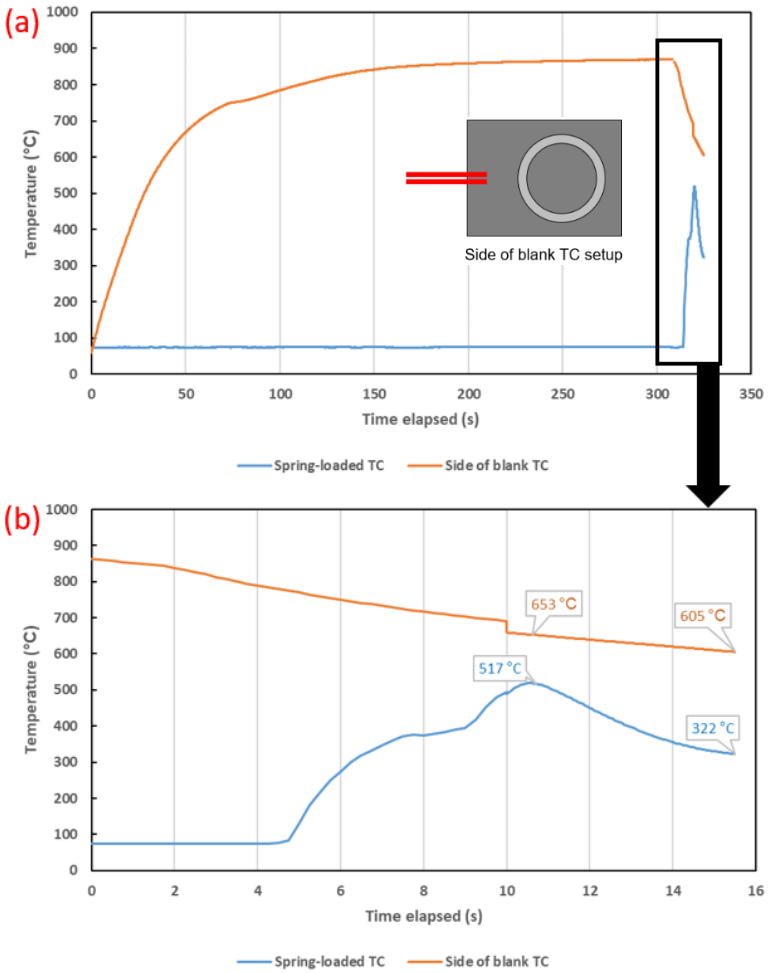

Figure 60: a) PHS1800 TCT specimen temperature profile using clamped thermocouples below the contact surface and another thermocouple welded on the side of the specimen. b) Close-up capturing the transfer and friction stages of the TCT test. Sliding speed: 20 mm/s. Contact pressure: 30 MPa

4.2.2. Temperature History Measured Using the Embedded Thermocouple

The measured temperature time histories from the edge thermocouple and the thermocouple embedded in the sample under the friction cup contact area (Section 2.2.4.2) are shown in Figure 61a. Since the thermocouple wires were embedded in the specimen, the recorded temperature profile during austenitization was similar to that obtained using the reference thermocouple in Figure 60a and Figure 61a. When the specimen was transferred from the furnace to the TCT apparatus, the measured temperature below the friction area decreased from ~900°C to ~750°C at the start of contact with the friction cup. Using a constant sliding speed of 20 mm/s, the friction rotation lasted approximately 5 seconds, and during which the specimen temperature decreased from ~750°C to ~275°C (Figure 61b). The temperature profile of the contact area was similar to that obtained using the reference thermocouple during the transfer and friction stages. A faster cooling rate was observed beneath the contact area, likely due to the immediate proximity of the contact area thermocouple to the friction cup which pulled heat out of the sample.

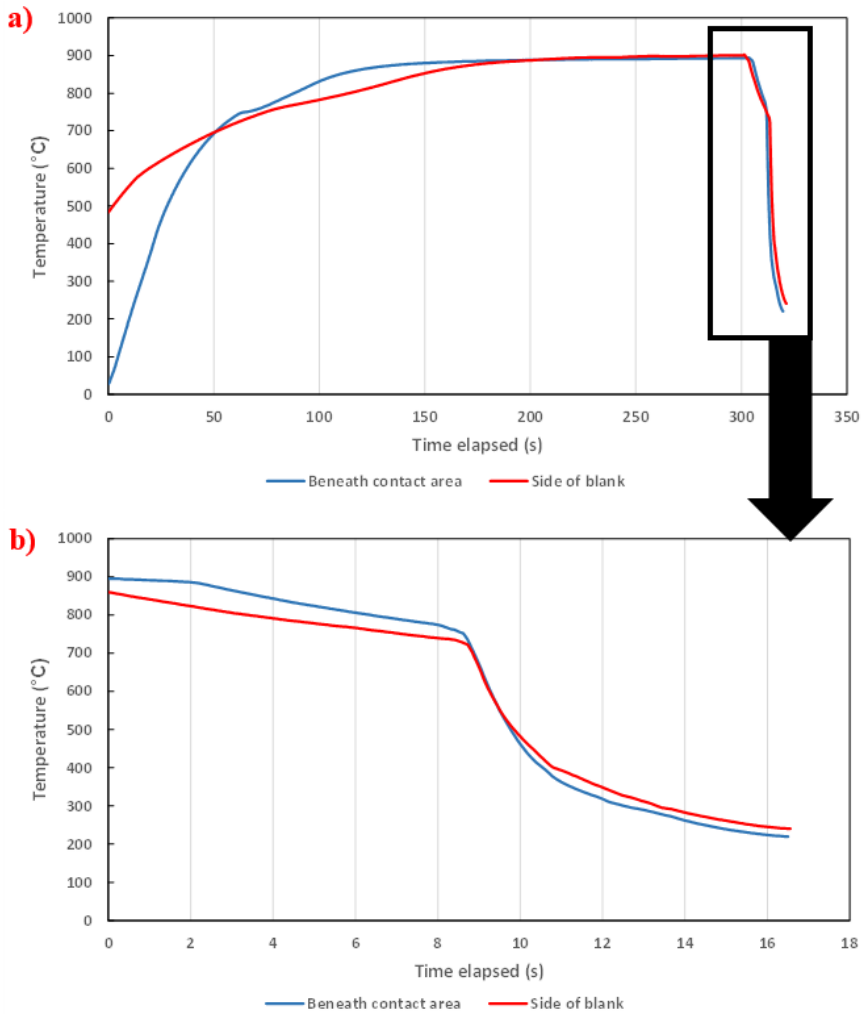

Figure 61: a) Alternative method for PHS1800 TCT specimen temperature profile using embedded thermocouples beneath the contact area. b) Close-up showing temperature history during the transfer and friction stages of the TCT test. Sliding speed: 20 mm/s. Contact pressure: 30 MPa. Sliding distance: 100 mm.

The cooling rate remained approximately constant at 12.5°C/s during the manual transfer from the furnace to the specimen holder. The cooling rate then increased to about 71.5°C/s upon contact with the cup, which was sufficient to produce a martensitic microstructure.

4.3. Friction Measurements

This section presents the measured CoF data and the dependency of friction response on parameters such as sliding distance, contact pressure, sliding speed, and tool wear.

4.3.1. Effect of Sliding Speed on Coefficient of Friction

Figure 62 shows a representative plot of CoF versus sliding distance obtained from a TCT test on a PHS1800 sample at a contact pressure of 30 MPa and sliding speed of 20 mm/s. The CoF was initially high due to static friction and then rapidly decreased as the interface transitioned to a dynamic friction condition. After this initial drop, the CoF gradually increased as the cup rotation continued. The CoF did not reach a steady state, because the specimen temperature was continuously decreasing due to heat conduction from the hot blank to the tooling and specimen holder. In addition, convection to ambient air and radiation also contributed to the cooling rate [38]. The contact pressure stabilized to its nominal value of 30 MPa after a sliding distance of 10 mm.

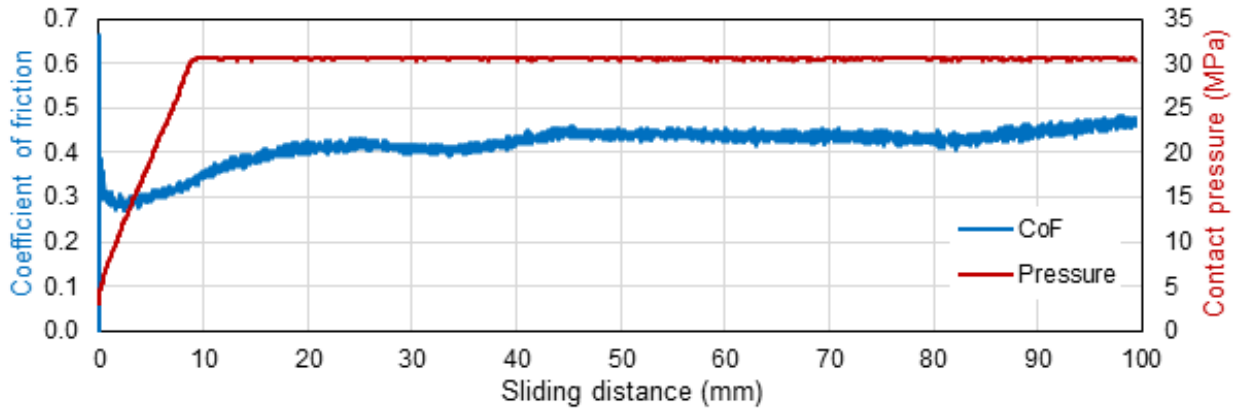

Figure 62: Representative CoF versus sliding distance history obtained from TCT testing of Al-Si coated PHS1800. Nominal sliding speed: 20 mm/s. Nominal contact pressure: 30 MPa.

The impact of sliding speed on CoF was analyzed from 10 mm/s to 38 mm/s using a constant contact pressure of 15 MPa. Figure 63a shows the CoF versus sliding distance for each sliding speed at a sampling interval of 10 mm sliding distance. Each CoF data point was obtained as an average over a sliding distance of 10 mm to reduce noise. The CoF data in Figure 63a varied with sliding distance with similar behavior for all sliding speeds considered. An average CoF for each test was calculated as the average value over a sliding distance range of 10-100 mm; this range was selected to avoid the initial static CoF below 10 mm sliding distance. The average CoF was plotted as a function of sliding speed in Figure 63b. In general, there was little dependence of the sliding velocity on the CoF for a contact pressure of 15 MPa as demonstrated by the overlap of the 95% confidence intervals in Figure 63b.

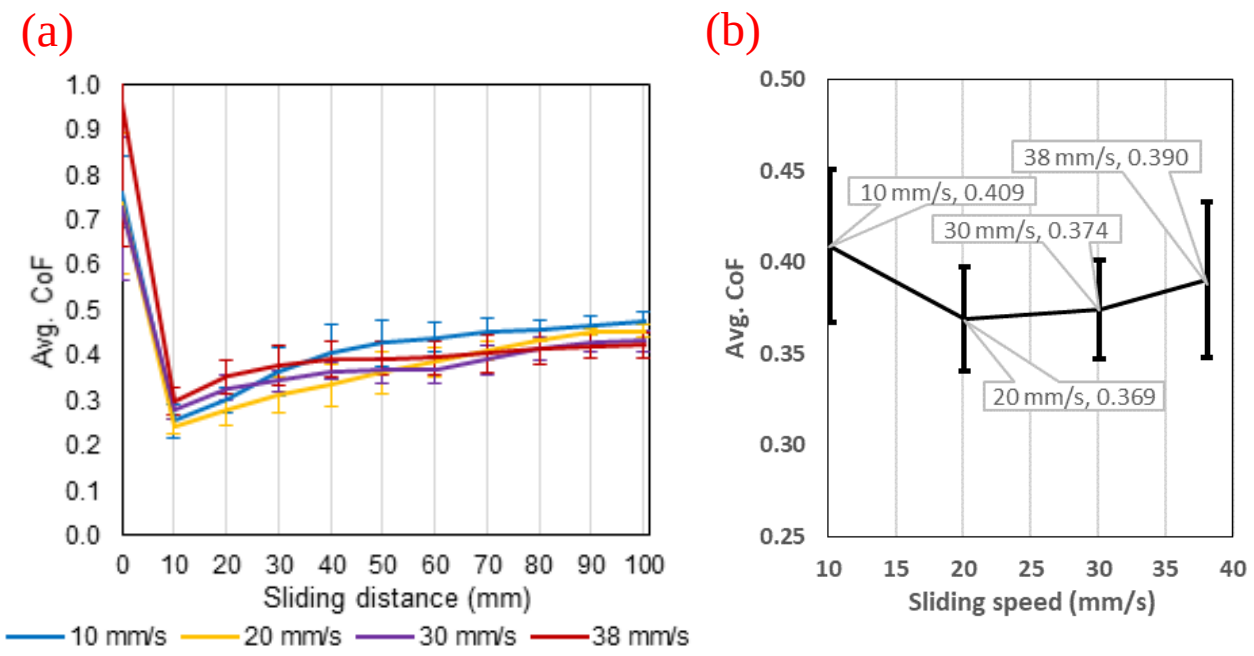

Figure 63: (a) CoF of PHS1800 at sliding speeds from 10 mm/s to 38 mm/s. Contact pressure is constant at 15 MPa. Each data point is an average CoF over a sliding distance of 10 mm. (b) Average CoF (10-100 mm sliding distance) at each sliding speed with a constant contact pressure of 15 MPa. Error bars correspond to 95% confidence intervals.

4.3.2. Impact of Contact Pressure on Coefficient of Friction

The influence of contact pressure on CoF was investigated using contact pressures in the range 5-30 MPa at a constant sliding speed of 20 mm/s. Similar to Figure 63a, Figure 64a shows the CoF versus sliding distance response for each contact pressure at a sampling interval of 10 mm sliding distance along with the average CoF from 10 to 100 mm (Figure 64b). The CoF had a significant dependency on contact pressure, as shown in Figure 64a and Figure 64b. The increase in average CoF with contact pressure (Figure 64b) was approximately linear over a range of contact pressure from 5 MPa to 25 MPa. It is believed that the contact pressure dependence was caused by asperity flattening within the contact interface, which increased the real contact area and the CoF [38].

Interestingly, Hardell *et al.* [3] reported a decrease in CoF with contact pressure for hot stamped Al-Si coated high strength boron steel hardened by tempering and quenching in water, which differed somewhat from the current work. However, those tests considered self-mated boron steel, which was essentially sliding on itself, tested at room temperature. Above this pressure range, the CoF did not change relative to that at 25 MPa. The strongest dependency on contact pressure was seen over a sliding distance of 10 mm to 60 mm (Figure 64a). Beyond this range, the CoF curves converged.

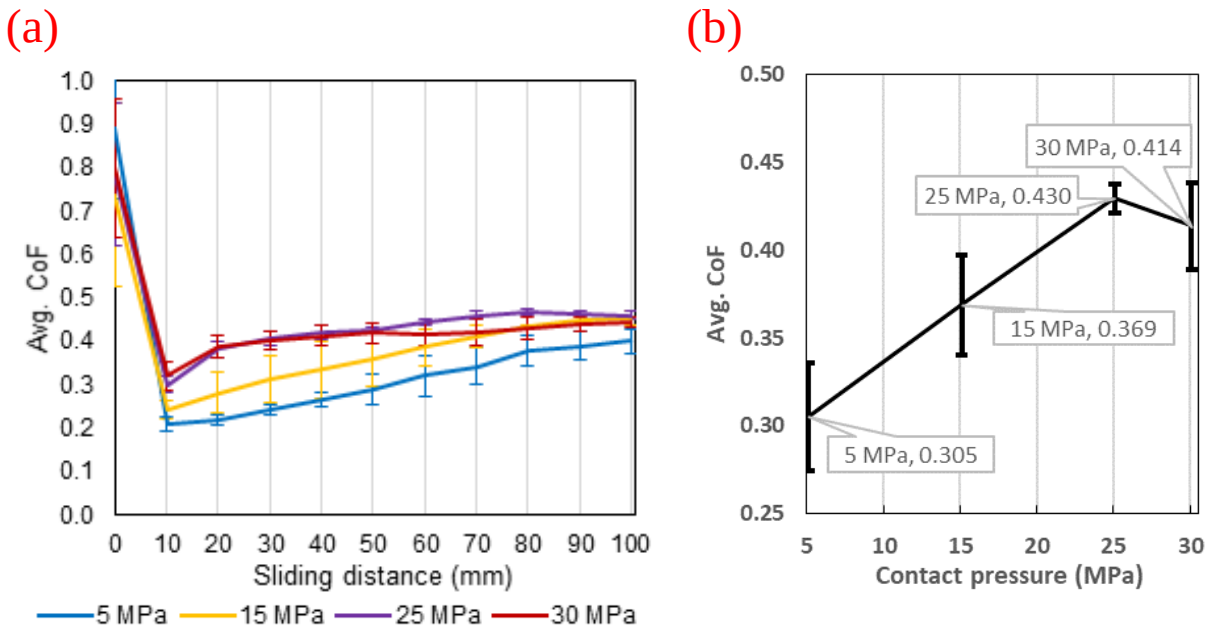

Figure 64: (a) CoF of PHS1800 at contact pressures from 5 MPa to 30 MPa. Sliding speed is constant at 20 mm/s. Each data point is the average CoF taken at 10 mm sliding distance intervals. (b) Average CoF (10-100 mm sliding distance) at each contact pressure at a sliding speed of 20 mm/s. Error bars correspond to 95% confidence interval for each sliding speed.

4.3.3. Impact of Tool Wear on Coefficient of Friction

To examine the effect of repeated frictional sliding on the same tooling surface, Figure 65a shows the results from repeated tests performed using new sheet samples on the same friction cup. The results demonstrated that repeated use of the same friction cup for up to 10 TCT tests did not significantly affect the average CoF beyond the initial transients prior to 10 mm sliding distance. Each test corresponded to a sliding distance of 100 mm, thus totalling a sliding distance of 1 m after 10 TCT tests using the same friction cup. Figure 65b does not show any statistically significant trend in CoF, because the majority of the 95% confidence intervals overlap among the data points. As a result, tool wear in the early stages of hot stamping production runs should not result in significant impact on its friction characteristics. Wear over the duration of longer production runs requires further investigation.

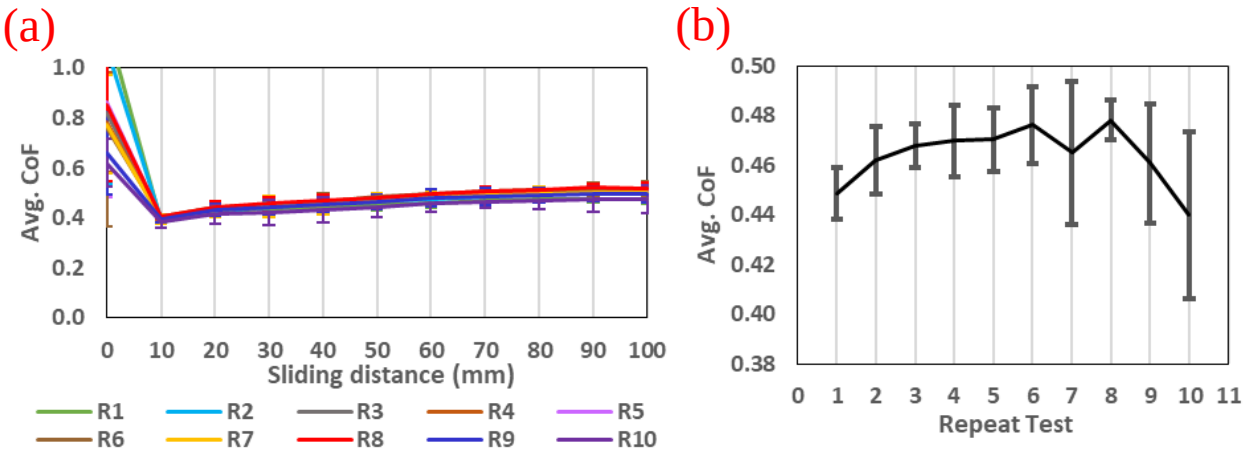

Figure 65: (a) CoF of PHS1800 at a constant contact pressure of 30 MPa and a constant sliding speed of 20 mm/s. A total of 10 TCT tests are performed on each friction cup with a sliding distance of 100 mm/run. Each curve (R1-R10) corresponds to successive repeat tests on the same friction cup. (b) Average CoF (10-100 mm sliding distance) for each TCT repeat test. Error bars correspond to 95% confidence interval for each repeat test.

4.4. Comparison of Coefficients of Friction between PHS Variants

The majority of the TCT were performed on the PHS1800 with select comparisons using PHS1500. These tests considered two Al-Si coating density variants: AS150 (150 g/m^3) and AS80 (80 g/m^3). The average CoF values for PHS1800, PHS1500 (AS150), and PHS1500 (AS80) are compared in Figure 66 using a constant sliding speed of 20 mm/s and a contact pressure of 30 MPa. The initial (static) CoF measured at a sliding distance of 0 mm was unstable with a high level of noise across each variant and did not provide accurate values of static CoF. Beyond a sliding distance of 10 mm, the average dynamic CoF of the PHS variants followed a similar trend with a positive slope as sliding distance increased up to 100 mm. Although the differences in CoF were relatively small, the average dynamic CoF magnitudes ranked in ascending order were: PHS1800, PHS1500 (AS150), and PHS1500 (AS80). These rankings were maintained throughout the dynamic friction range from 10 mm to 100 mm. Since PHS1800 and PHS1500 (AS150) had the same Al-Si coating density of 150 g/m^2, the lower average dynamic CoF of PHS1800 was likely caused by the difference in the base metal strengths and microstructure. On the other hand, the higher average dynamic CoF of PHS1500 for the thinner AS80 coating compared to thicker AS150 coating was likely caused by the former's lower Al-Si coating density of 80 g/m^2, because the base metal constituents were identical. The thicker Al-Si coating of the AS150 variant caused the friction cup to grind through more coating material than the AS80 variant before reaching the base metal. Since the Al-Si coating had different mechanical properties than the PHS1500 base metal, the friction behavior of the tooling with the Al-Si coating was different than with the PHS base

metal. An earlier depletion of the coating through adhesion would increase the CoF as the tooling slid directly against the PHS base metal.

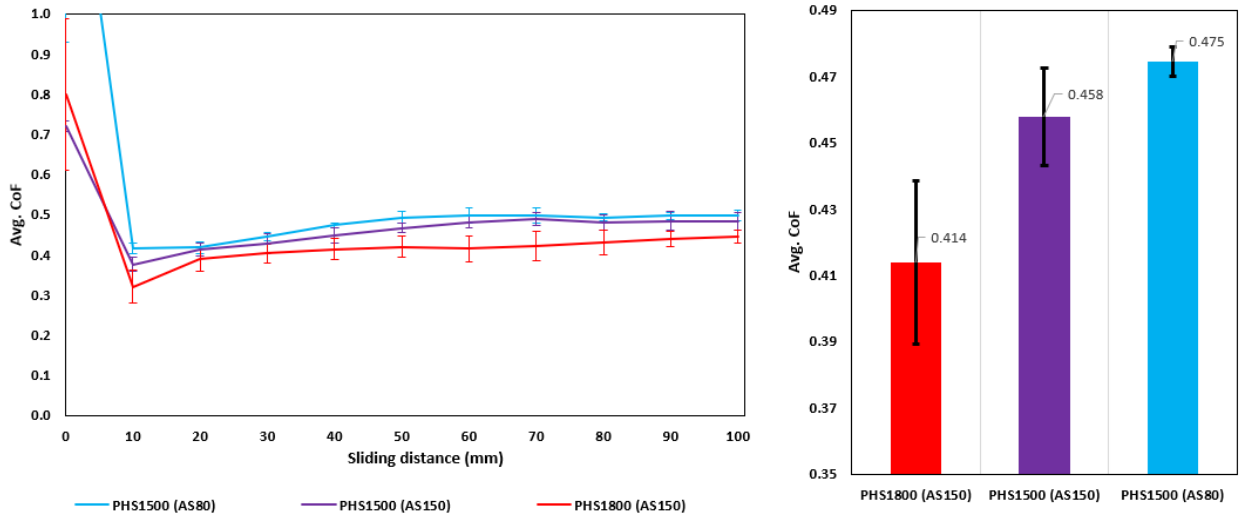

Figure 66: Average coefficients of friction comparison between PHS1800, PHS1500 (AS150), and PHS1500 (AS80). Error bars represent 95% confidence intervals. Sliding speed: 20 mm/s. Contact pressure: 30 MPa.

4.5. Post-Test Observations of TCT Specimens

During the tool wear test, the friction cup and TCT specimens were examined after each repeat test. To evaluate the consistency of CoF during tool wear, the surface roughness of the friction cups was measured. The specimen and friction cup mass changes were also monitored for any significant transfer of material.

4.5.1. Surface Roughness of Friction Cups and Worn Specimens

The wear marks on the specimen surface showed a decrease in average surface roughness in the direction perpendicular to the sliding direction as sliding speed (Figure 67a) or contact pressure (Figure 67b) increased. The average surface roughness in the direction parallel to the sliding direction decreased from 10 mm/s to 20 mm/s then remained consistent at higher speeds. The surface roughness in the direction parallel to the sliding direction decreased as pressure increased from 5 MPa to 15 MPa. Nonetheless, it remained consistent at higher contact pressures. The decrease in surface roughness was likely caused by an increasing amount of rough Al-Si coating ground away by the friction cup. However, the statistical significance of the observed trends was low due to overlapping 95% confidence intervals.

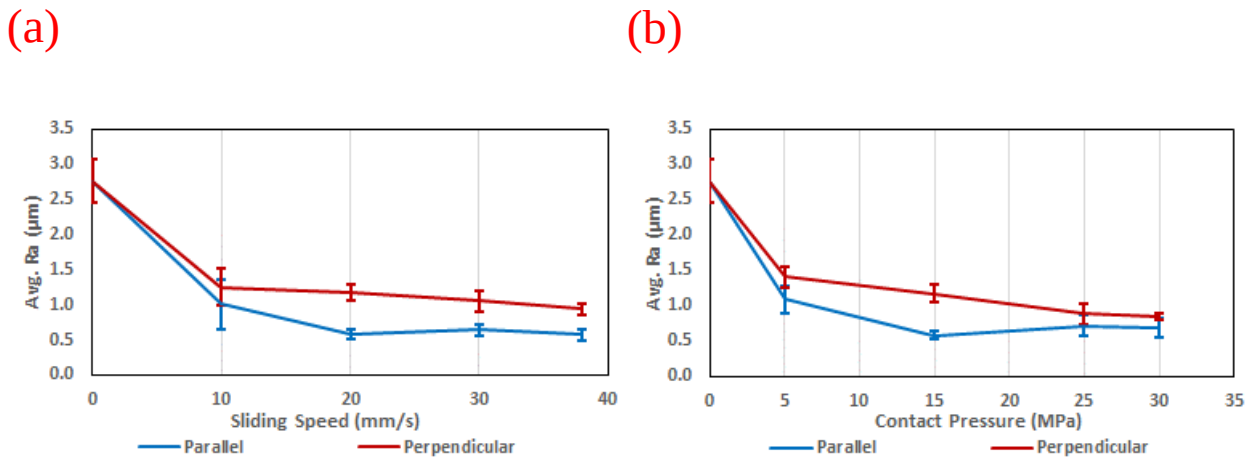

Figure 67: Average surface roughness of wear marks on single PHS1800 TCT test specimens using new friction cups with (a) sliding speeds from 10 mm/s to 38 mm/s at 15 MPa. (b) Contact pressures from 5 to 30 MPa at 20 mm/s. Initial average surface roughness after austenitization is 2.76 µm, as shown in Table 8.

Before the first tool wear test, the friction cups were lapped to a surface finish with an Ra value of about 0.2 µm. After the first test, the surface roughness of the cup increased significantly for measurements taken in directions parallel and perpendicular to the sliding direction (Figure 68). After the first test, the surface roughness remained constant for all subsequent TCT tests on the same friction cup. This observation was consistent with the results in Section 4.3.3, which demonstrated that tool wear did not have a statistically significant impact on the CoF, at least for the limited number of repeat tests performed here. Material transfer of Al-Si coating from the test specimens to the friction cup [37] and of tooling material from the friction cup to the test specimen [40] likely occurred during each friction test. The occurrence of this material transfer in TCT was not validated in this study.

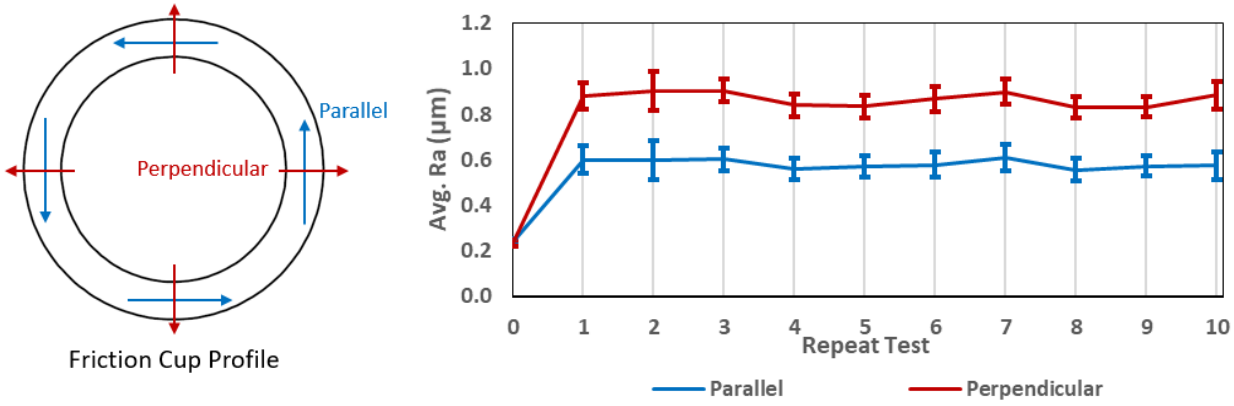

Figure 68: Average surface roughness of friction cup (tooling) in lapped condition and after each TCT repeat test. Measurements are taken in directions parallel and perpendicular to the sliding direction against the specimen. Error bars correspond to 95% confidence interval for each TCT run. Sliding speed: 20 mm/s. Pressure: 30 MPa.

5. Formability Characterization Results and Discussion

This chapter presents the results of the formability characterization of the PHS1800 and PHS1500 sheets using the Nakazima and Marciniak and hybrid Nakazima-Marciniak punch developed by Deng and McGuire [56] is considered.

5.1. Nakazima Dome Tests on PHS1800

The Nakazima tests represented the first attempt at characterizing the formability of PHS under hot stamping conditions and provided a baseline for all subsequent formability tests. Since the Nakazima test did not utilize a carrier blank, it represented the simplest formability test setup. Initial tests were performed in which the die descended in a single stroke without pausing (zero clamping time). Additional tests considered a pause in the stroke in which the die descended far enough to clamp the blank against the binder and held for a period of time (clamping time) prior to contacting the punch. The clamping period served to quench the outer periphery of the blank while maintaining a higher temperature at the apex of the sample.

Using stereoscopic DIC imaging of the sample's speckled surface during deformation, the principal strains and fracture onset could be used to assess the material's formability characteristics. Necking and fracture occurred a significant distance away from the apex of the Nakazima punch, as shown in Figure 69 for all sample widths considered. One reason for this deviation from the apex was friction between the unlubricated punch and hot sample. In addition,

the material in contact with the punch apex and die/binder quenched more quickly than the unsupported region of the sample where the localization occurred.

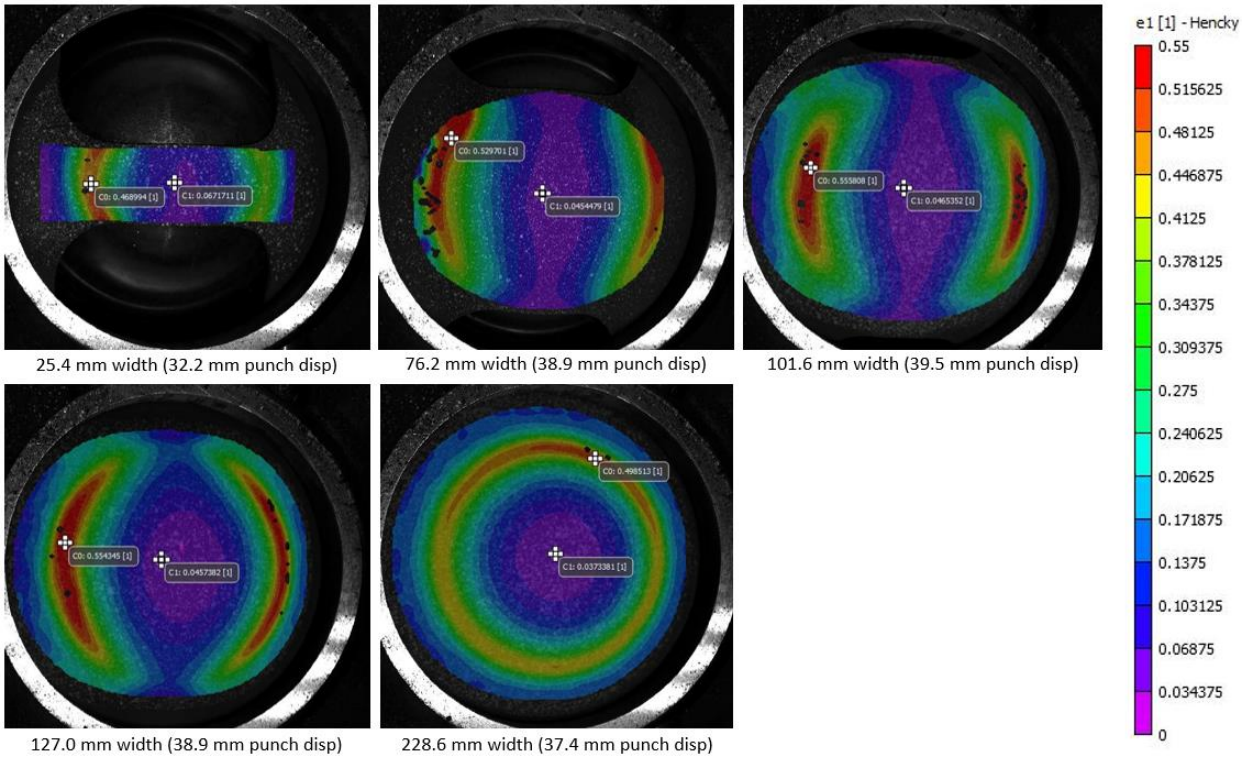

Figure 69: Major strain distribution of unlubricated Nakazima dome samples at the onset of fracture. Nominal punch speed: 60 mm/s. Clamping time: 0 second. Lubrication: None

As the sheet temperature at the punch apex decreased, its flow stress increased which caused additional resistance to deformation. As a result, the strain paths at the necking locations remained close to plane strain, regardless of sample width, as evidenced by the rather low minor strains seen in Figure 70. Despite this off-apex failure location, the strains to fracture in these specimens were well in excess of 0.4, indicating the very high formability of the PHS1800 grade under hot stamping conditions.

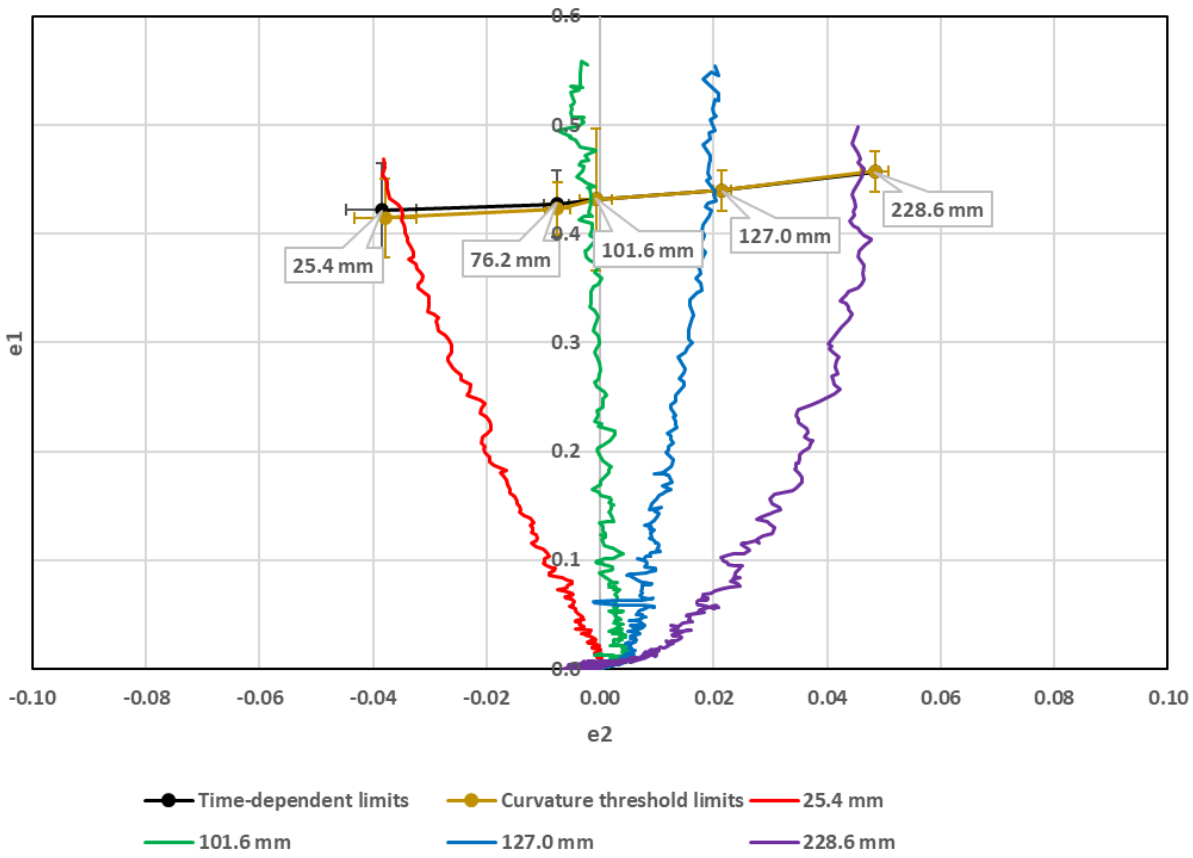

Figure 70: Strain paths for sample widths from 25.4 to 228.6 mm with the LBF and curvature-based limit strains. Nominal punch speed: 60 mm/s. Clamping time: 0 second. Lubrication: None

The necking limit strain for each strain path was calculated using the time-dependent linear best fit (LBF) method developed by Volk and Hora (Figure 71) [26] and implemented by DiCecco *et al.* [27] within a MATLAB program. This method determined the beginning of instability based on a representative thinning rate from the DIC strain measurements. The thinning rate curve was separated into stable and unstable zones. Each zone was then fit with a least squares linear regression line. The intersection of the regression lines from each zone was taken as the threshold of strain rate instability and onset of necking. These necking limits are plotted in Figure 70 from which the calculated necking limit strains were well aligned with their corresponding strain paths

and formed an FLC over the limited range of minor strain of -0.04 to 0.05. The 101.6 mm width geometry produced a strain path that was closest to plane strain to identify the FLC0. This rather limited range of minor strain was due to necking occurring away from the punch apex, shown in Figure 69, which imposed a constraint on the minor strain development.

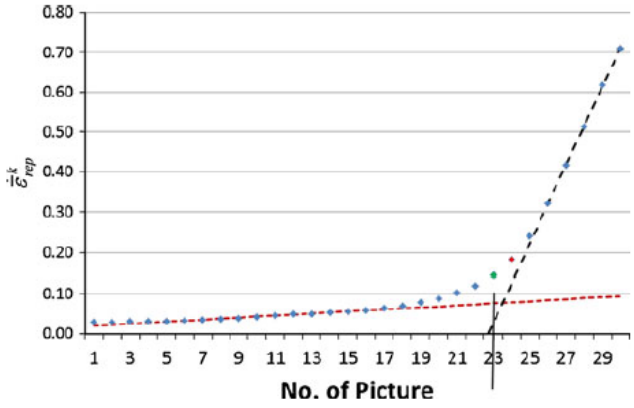

Figure 71: Example demonstrating the time-dependent linear best fit (LBF) necking detection method developed by Volk and Hora [26]

As an alternative to using the LBF method, the necking limit strain of each strain path was also determined using the enhanced curvature method of DiCecco *et al.* [61] with a threshold of 0.005 mm^{-1}. The limit strains with the curvature method, also plotted in Figure 70, were very close to the LBF values.

Attempts to solve the problem of localization occurring away from the punch apex, which resulted in near-plane strain conditions for every sample geometry, included applying lubrication on the contacting surface of the punch and increasing the clamping time prior to the forming stroke. Since a high CoF between the punch and sample inhibited free movement of the sample material at the apex, a graphene-based lubricant was applied on the contact surface of the punch using a brush.

As the solvent dried, a layer of solid graphene particles remained on the surface that were resistant to the transient temperatures experienced at the punch-sheet metal interface. These graphene particles served as a solid-state lubricant that reduced friction between the contact surfaces. Unfortunately, the graphene lubricant did not produce any significant improvement in shifting the necking location toward the apex, as demonstrated in Figure 72. In the unlubricated condition, the necking area of the 25.4 mm gage width PHS sample is represented by the red zone in Figure 72 and was located at the gage transition zone in the unsupported region of the sheet between the punch and the die, away from the center of the PHS sample. Likewise, the 228.6 mm diameter equibiaxial geometry also had localization away from the apex. When the graphene lubricant was applied, the observed necking locations of the 25.4 mm gage width and the 228.6 mm diameter sample geometries were similar to those from the reference unlubricated condition. On the other hand, the necking limit strain of the lubricated samples were lower than that of the reference due to lower sample temperature. This may be caused by the higher thermal conductivity from the lubricant which created a high cooling rate for the sample. When the sample temperature decreased, so did the limit strain.

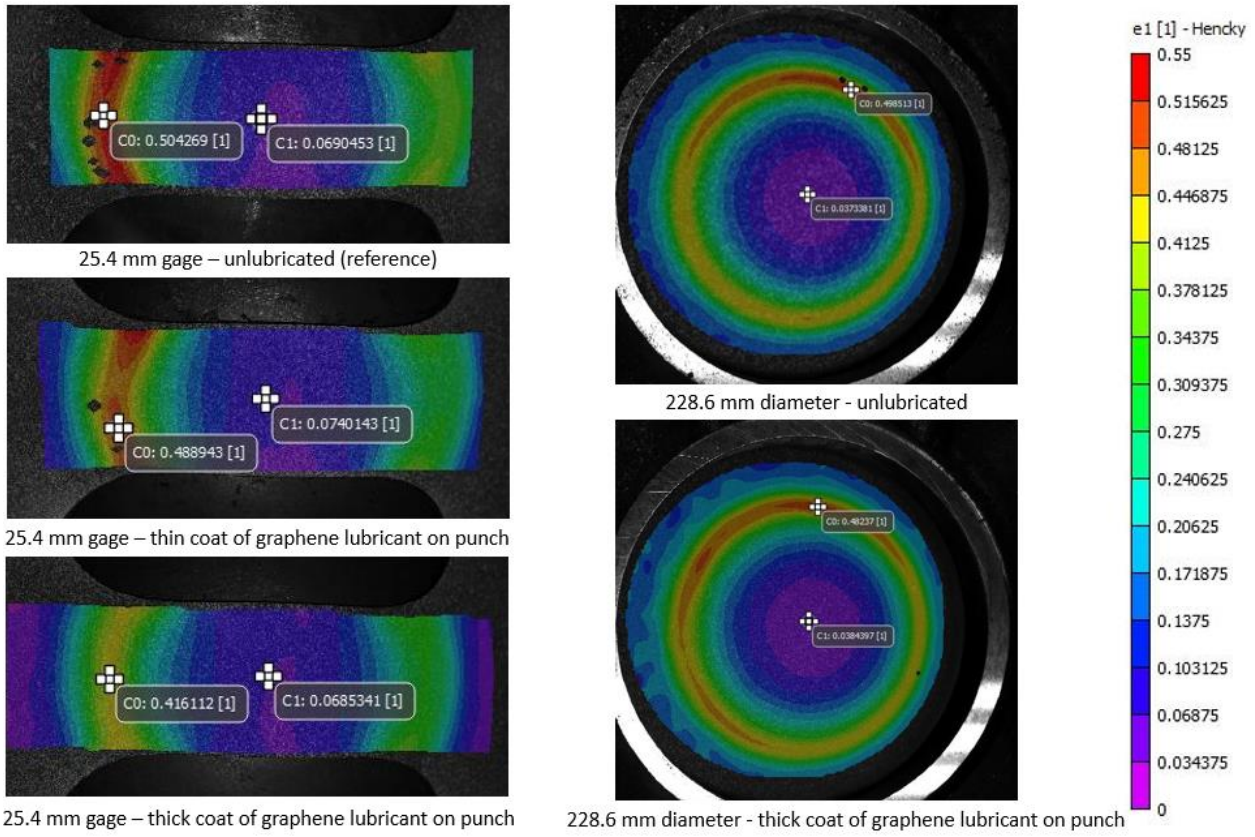

Figure 72: Major strain distribution of lubricated Nakazima dome samples with gage widths of 25.4 mm and 228.6 mm at the onset of fracture without prolonged clamping time. Graphene lubrication is applied on the punch. Major strain distributions of unlubricated samples are shown for reference. Nominal punch speed: 60 mm/s. Clamping time: 0 second. Lubrication: graphene solution

As the PHS sample temperature decreased, its flow stress increased as demonstrated by Lu *et al.* [16]. Therefore, decreasing the temperature of the peripheral area of the blank close to the clamped region while maintaining a high temperature at the apex should induce a higher amount of deformation at the apex. To promote such a temperature distribution, prior to the forming stroke, the sample was clamped between the binder and die for up to 10 seconds to quench the peripheral area of the sample. During this clamping period, the sample was held above the punch to limit cooling at the apex. Again, however, the resulting necking location was still located away from the apex for the 25.4 mm gage width and the 228.6 mm diameter geometries, as seen in Figure 73,

without a significant difference in the induced level of minor strain compared to the reference method in Figure 69. The necking location major strain values of both sample geometries decreased as the clamping time increased. Since the PHS sample temperature decreased during clamping, the limit strains decreased. In addition, strain concentrated towards the edges of the gage section radius due to the stress concentration associated with the rounded notch.

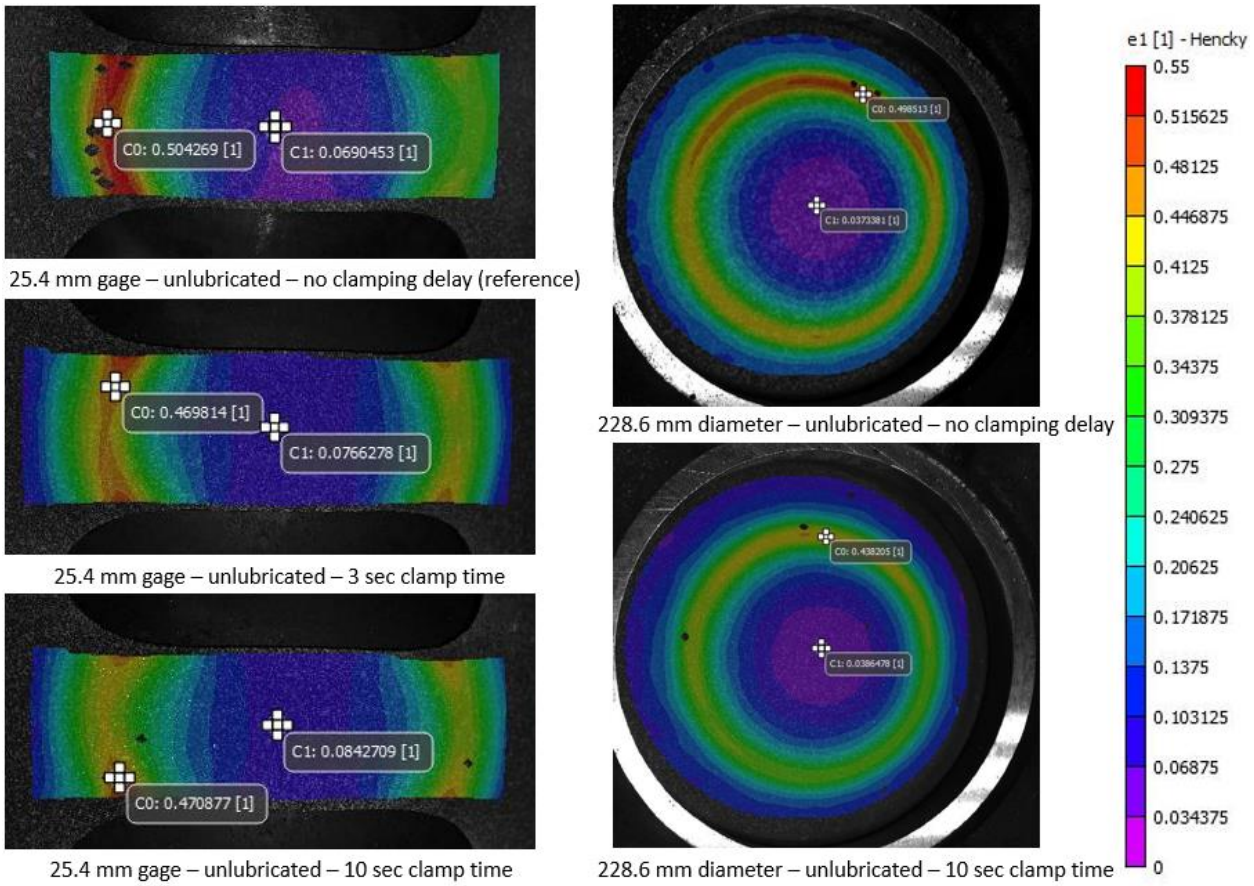

Figure 73: Major strain distribution of unlubricated Nakazima dome samples with gage widths of 25.4 mm and 228.6 mm at the onset of fracture with prolonged clamping times. Major strain distributions of unlubricated samples without a prolonged clamping time are shown for reference. Nominal punch speed: 60 mm/s. Clamping time: 0, 3 or 10 seconds. Lubrication: none

Finally, to further increase the temperature difference between the apex and its peripheral area, tests were performed with the punch heated to 300°C to reduce cooling of the apex region to promote localization. Unfortunately, it was not successful. This approach aimed to reduce the cooling rate at the apex due to the lower temperature difference between the austenitized sample and punch surface. Nonetheless, the heated punch did not promote a change in necking location toward the apex, as seen in Figure 74.

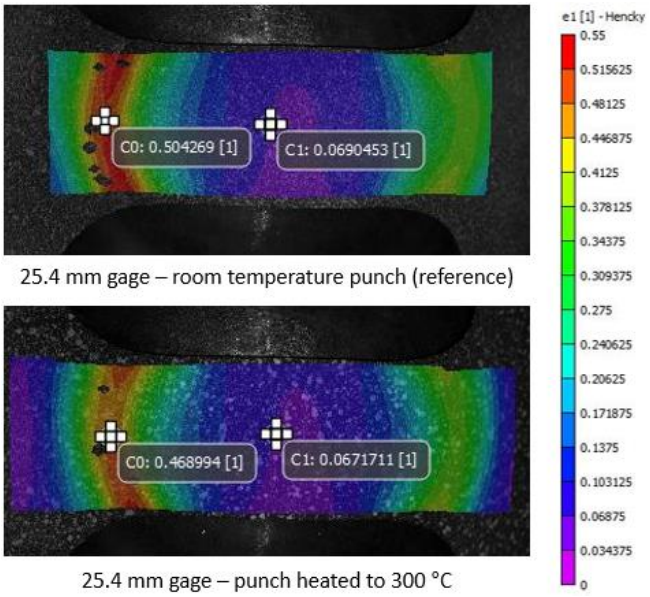

Figure 74: Major strain distribution of 25.4 mm gage width PHS1800 samples at necking limit strains with a room temperature punch (reference) and a punch heated to 300°C. Nominal punch speed: 60 mm/s. Clamping time: 0 second. Lubrication: none

5.2. Marciniak Tests on PHS1800

Since Nakazima tests were not successful in characterization formability across a broad range of strain states, Marciniak tests were considered with the carrier blank serving to quench the outer region of the blank while the central region stayed at a high temperature and localized.

The Marciniak tests were successful to promote localization within the central hole of the carrier blank for different gage widths shown in Figure 75. The carrier blank did not appear to fracture prior to the onset of necking.

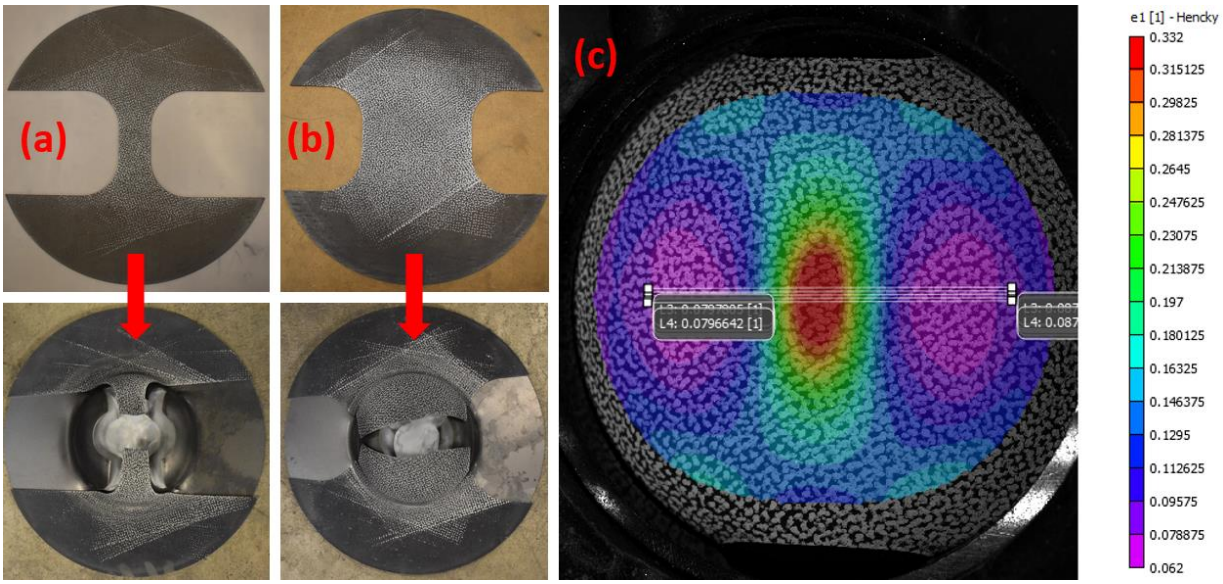

Figure 75: PHS1800 samples before and after Marciniak testing: (a) 25.4 mm gage (b) 114.3 mm gage. (c) Major strain profile of a PHS1800 sample with 114.3 mm gage at the onset of necking. Nominal punch speed: 60 mm/s. Clamping time: 3 seconds. Lubrication: none

5.2.1. Strain Paths and Limit Strains

Using DIC strain measurements at the center of each PHS sample geometry during the forming stroke, the strain paths in terms of the major versus minor strain are shown in Figure 76 from the Marciniak tests. The necking location happened at the blank center without significant friction, with a higher temperature, and with a lower flow stress relative to the shoulder of the blank. Therefore, the measured strain paths spanned the entire desired range of the minor strain. The 50.8 mm gage width produced a strain path that was relatively close to uniaxial deformation with large negative minor strains. The 101.6 mm gage produced a near-plane strain condition with a minor strain magnitude lower than 0.007. Likewise, the 228.6 mm diameter sample geometry produced near-equibiaxial deformation. In contrast to the Nakazima tests, the Marciniak strain paths were more linear as expected. Each strain path followed a linear trend due to the absence of bending, in contrast to the Nakazima strain path data in Figure 70.

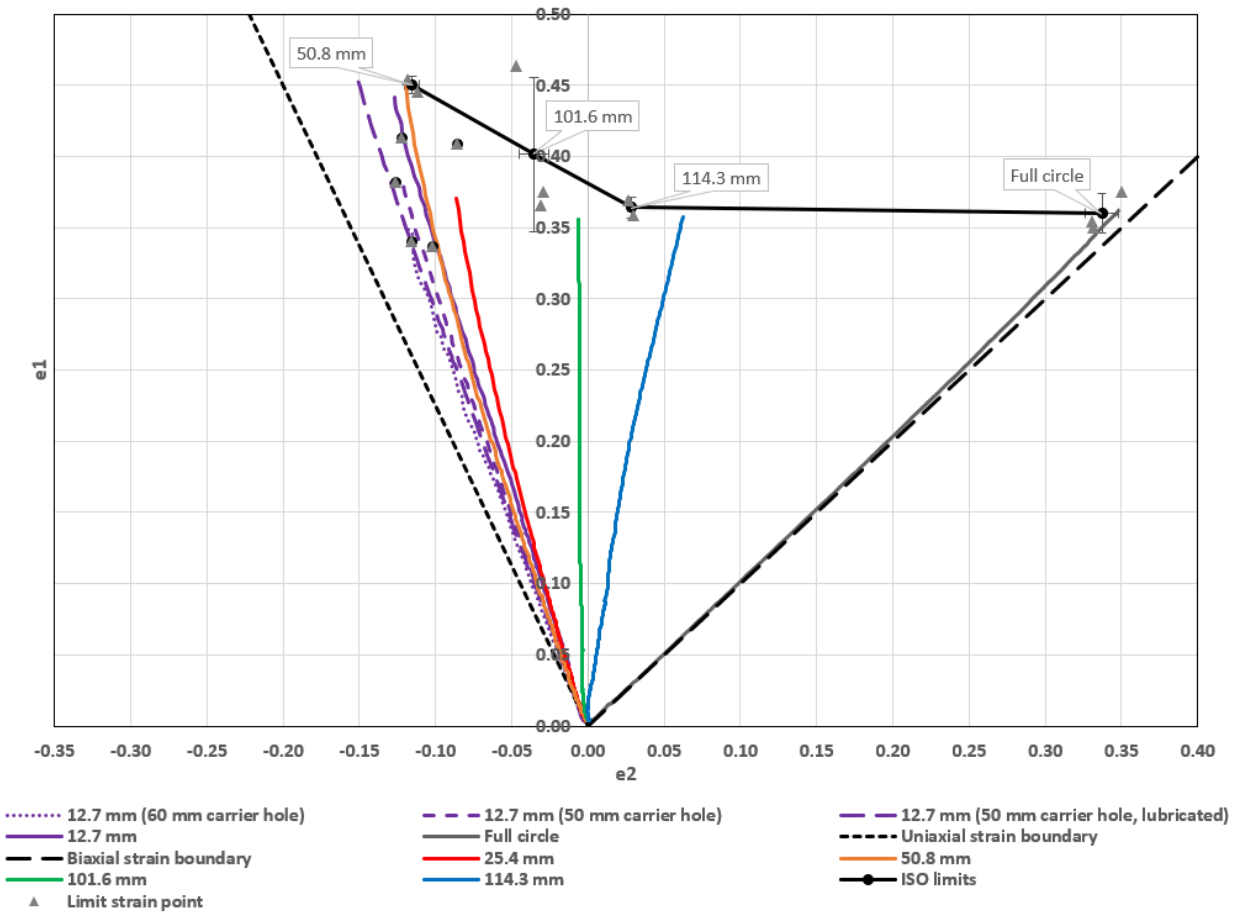

Figure 76: Strain paths of PHS1800 sample geometries and their corresponding FLC using the Marciniak test. The necking limit strains of the FLC are determined using the ISO method. Error bars correspond to the sample standard deviation of each necking limit strain. Nominal punch speed: 60 mm/s. Lubrication: 3 sheets of 0.127 mm thick Teflon between punch and carrier blank. Clamping time: 3 seconds. R-value: 0.8

Several attempts were made to generate strain paths that were closer to the uniaxial strain condition. This included use of blanks with narrower gage widths of 25.4 mm and 12.7 mm. In addition, application of the graphene-based lubricant onto the carrier blank around the center hole was implemented to reduce frictional resistance. Finally, larger center hole cut-out diameters of 50 mm and 60 mm in the carrier blank were also implemented. The results of these attempts are plotted in Figure 76. As can be seen, the narrower blank width of 12.7 mm did result in a strain path that was incrementally closer to uniaxial tension than the 50.8 mm blank. For these narrower

blanks, the larger carrier cut-out and addition of lubricant further shifted the strain path towards uniaxial tension. Unfortunately, the rather narrow gage width of 12.7 mm made the soft blank difficult to handle during robotic transfer from the furnace to tooling.

Due to the large DIC speckle size deployed to counter the negative effects of Al-Si coating surface cracks during extensive deformation, the resulting large virtual strain gage resulted in a compromise in the spatial resolution of the strain field. This issue generated noise at the apex area when necking became imminent. It confounded application of the LBF [26] and curvature [62] methods, which were not successful at resolving the limit strains in a consistent manner due to the local nature of these detection methods. As a result, the position-dependent ISO necking limit method [55] was used instead to determine the necking limit strain for all the Marciniak tests. It interpolated the necking strain at the blank center based on the surrounding lower-noise strain field. The resulting FLC in Figure 76 spanned from near-uniaxial deformation of the 50.8 mm gage width to the equibiaxial 228.6 mm diameter circular blank.

Figure 77 shows the measured major and minor strain distributions at the centerline of each sample geometry along the gage length and perpendicular to the sheet rolling direction. The strain distributions in Figure 77 were taken shortly after localized necking, but prior to final fracture when the DIC speckle pattern was compromised. The maximum value of each major strain curve corresponded to the center of the sample. As expected, the minor strain at the center of each blank was negative for the 50.8 mm gage, near zero for the 101.6 mm gage, and close to its corresponding major strain value for the 228.6 mm diameter circle.

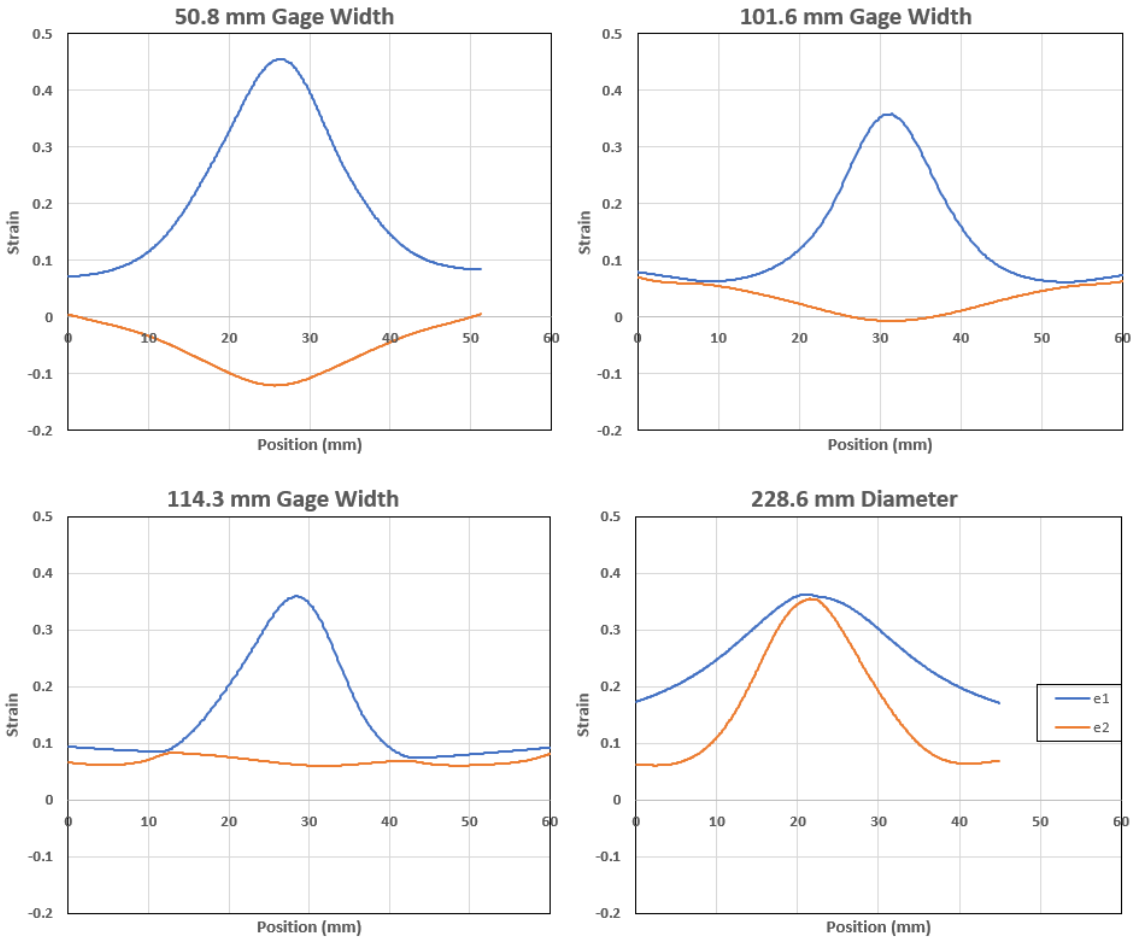

Figure 77: Major and minor strain distributions of PHS1800 at the centerline of the gage length perpendicular to the rolling direction. The strain profiles are taken near the onset of necking before excessive noise appears at the apex. The peak major strain in each geometry corresponds to the apex of the sample. Nominal punch speed: 60 mm/s. Lubrication: 3 sheets of 0.127 mm thick Teflon between punch and carrier blank. Clamping time: 3 seconds.

5.2.2. Measured Temperature and Strain Rate at Blank Center

The influence of strain rate on formability is particular interest since the increased positive rate sensitivity at elevated temperatures can increase the limit strains. According to Figure 53, the punch speed was not constant and, as a result, the strain rate at the PHS1800 sample center

increased during the test. Figure 78 shows the measured Von Mises effective strain rate as a function of effective strain at the blank center for each sample width. Each strain rate history was plotted until fracture. All PHS sample geometries showed an increase in strain rate over the deformation history (Figure 78). This increase likely reflected an increase in punch speed during the tests, as well as onset of diffuse necking in the near-uniaxial deformation case. The effective strain corresponding to the necking onset is also indicated in Figure 78. The operative strain rate at necking ranged from 2 s^{-1} for the circular 228.6 mm diameter specimens to over 5 s^{-1} for the narrower 50.8 mm gage width specimens.

Note that the repeat tests for each sample geometry followed a similar trend in strain rate history during the entire forming stroke. Each curve featured a data point collection interval of 0.002 seconds and a moving average filter with a span of 20 data points to reduce noise while maintaining an acceptable level of data resolution.

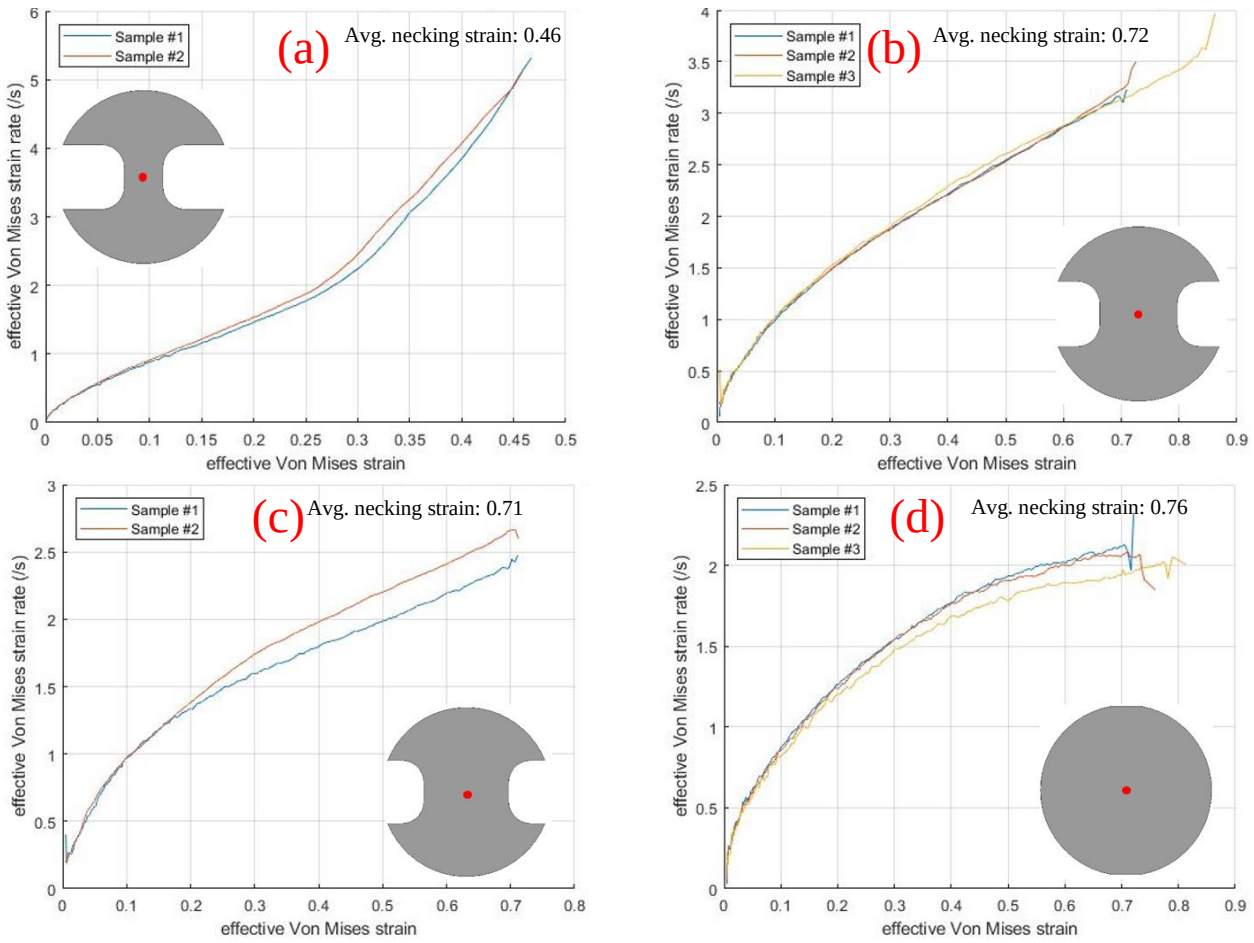

Figure 78: Effective Von Mises strain rate as a function of its strain values for PHS1800 test results obtained with each gage width: (a) 50.8 mm (b) 101.6 mm (c) 114.3 mm (d) 228.6 mm.

The temperature histories at the center of the PHS1500 (AS150) samples are shown in Figure 79 along with the major strain. Also plotted is the major strain history until the onset of necking. The corresponding cooling rate remained almost constant for all gage widths. This linear decrease in temperature at the center of the blank was likely a result of the absence of physical contact with any component in the central region because it was suspended above the carrier blank hole. Consequently, the sample gage width did not show any significant impact on the cooling rate which

varied from 21.8°C/s to 24.5°C/s. The temperature decrease over the course of the test was approximately 15°C, which was considered small.

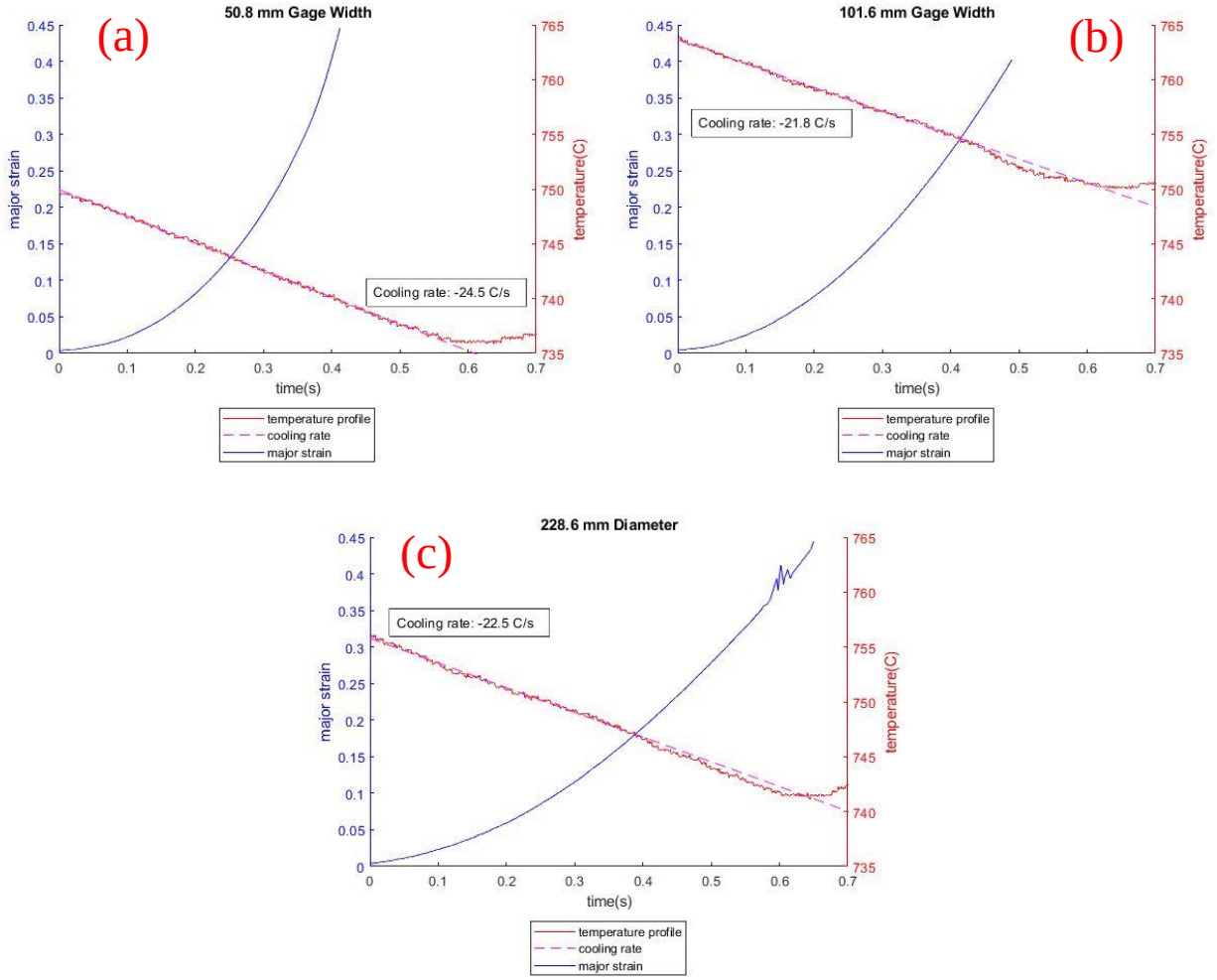

Figure 79: Major strain and temperature progress of PHS1500 (AS150) during the forming stroke of the Marciniak test for gage widths of a) 50.8 mm, b) 101.6 mm, and c) 228.6 mm diameter. Major strain is measured until the onset of necking. Average cooling rate is obtained through linear regression until 0.4 seconds. Nominal punch speed: 60 mm/s. Lubrication: 3 sheets of 0.127 mm thick Teflon between punch and carrier blank. Clamping time: 3 seconds.

As the forming stroke progressed, the effective Von Mises strain rates of all sample geometries increased as well (Figure 80). The magnitude of the effective Von Mises strain rate decreased as the sample gage increased in width. Thus, the deformation of the sample accelerated throughout

the forming stroke, and the magnitude of this acceleration decreased as the deformation mode shifted from near-uniaxial to equibiaxial.

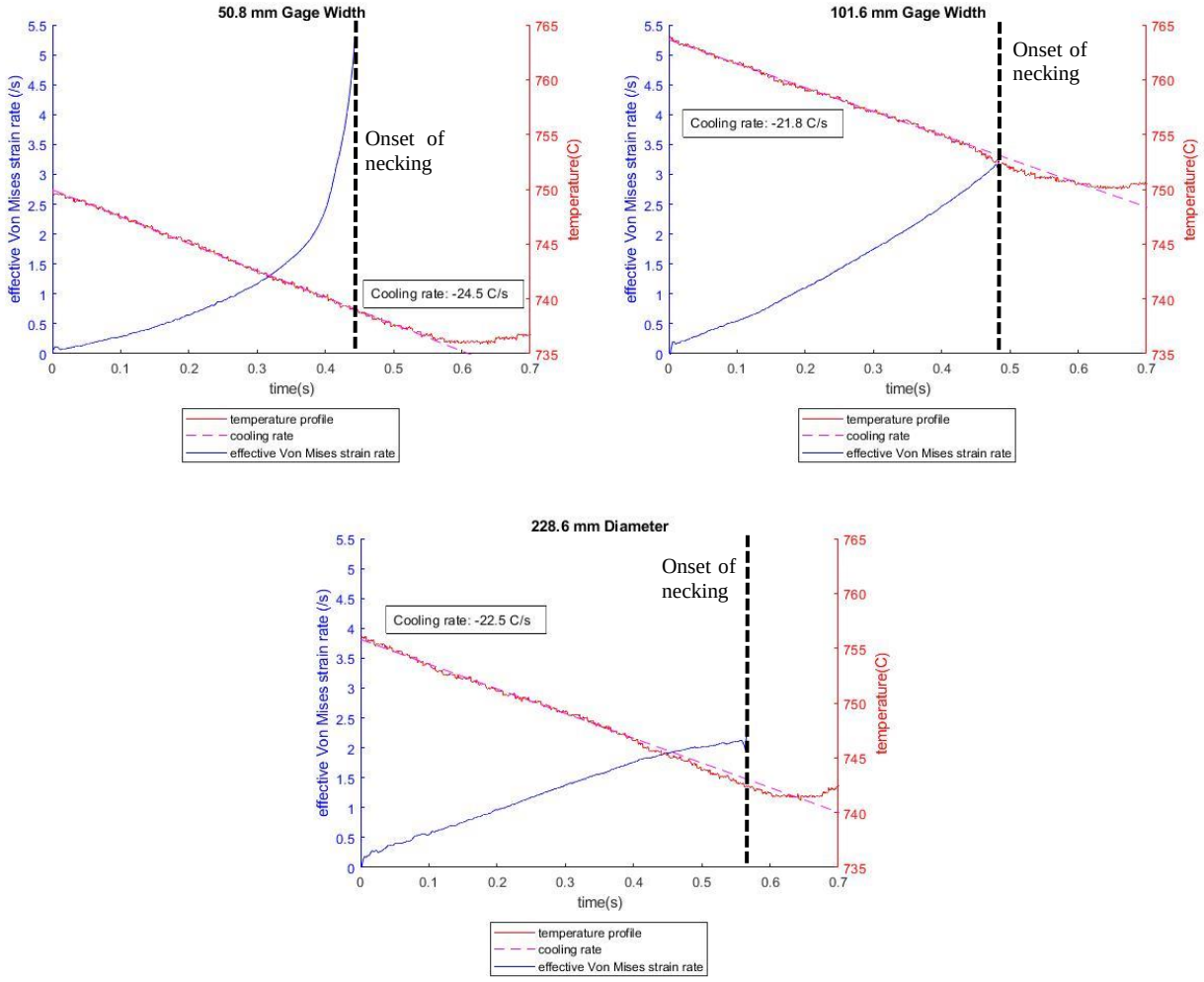

Figure 80: Effective Von Mises strain rate and temperature progress of PHS1500 (AS150) during the forming stroke of the Marciniak test. Effective Von Mises strain rate is measured until the onset of necking. Strain rate of the 228.6 mm diameter PHS sample geometry is prematurely stopped at ~0.6 sec due to excessive instability. Average cooling rate is obtained through linear regression until 0.4 seconds. Nominal punch speed: 60 mm/s. Lubrication: 3 sheets of 0.127 mm thick Teflon between punch and carrier blank. Clamping time: 3 seconds.

5.3. Hybrid Nakazima-Marciniak Formability Tests on PHS1800

This section presents the hot formability characterization of PHS1800 using the hybrid Nakazima-Marciniak punch geometry, initially developed by Deng and McGuire [56]. Like the Marciniak punch geometry, the hybrid punch featured a flat top section that enabled the use of a carrier blank to decrease friction at the blank center. The larger profile radius of the hybrid punch helped to resist tearing at the punch radius that was sometimes observed using the Marciniak punch.

The measured strain paths using the hybrid punch also spanned the near-uniaxial to equibiaxial strain ratios, as shown in Figure 81. In attempts to produce strain paths that were closer to the uniaxial strain boundary than the repeatable 50.8 mm gage width, the gage width was narrowed to 25.4 mm then to 12.7 mm. Like the Marciniak test, the 25.4 mm gage width did not produce a strain path that was closer to the uniaxial stress condition than the 50.8 mm gage width. On the other hand, the 12.7 mm gage width demonstrated a possible improvement over the 50.8 mm gage width.

Unlike the Marciniak test strain paths, applying graphene lubricant around the carrier blank center hole or increasing the carrier center hole diameter from 32 mm to 50 mm did not produce higher minor strain magnitudes in near-uniaxial deformation for the 12.7 mm gage width. As a result, the more repeatable 50.8 mm gage width samples were used to characterize necking limit strains under negative minor strain conditions.

Although the 101.6 mm gage width produced near plane strain deformation in Marciniak testing, it resulted in significant positive minor strain values in its strain path, so it did not create a plane strain state with the hybrid punch. Tests performed using a narrower 88.9 mm gage width produced slightly negative minor values that were closest to the plane strain state. Due to the effect of bending deformation from the large shoulder radius of the hybrid punch, all strains paths were less linear than their Marciniak counterparts.

Using the strain paths from the 50.8 mm, 88.9 mm, 101.6 mm, and 228.6 mm specimen widths, average necking limit strains were obtained with the same ISO interpolation method [55]. The resulting FLC spanned from near-uniaxial to equibiaxial stretching with the lowest limit strains near plane strain.

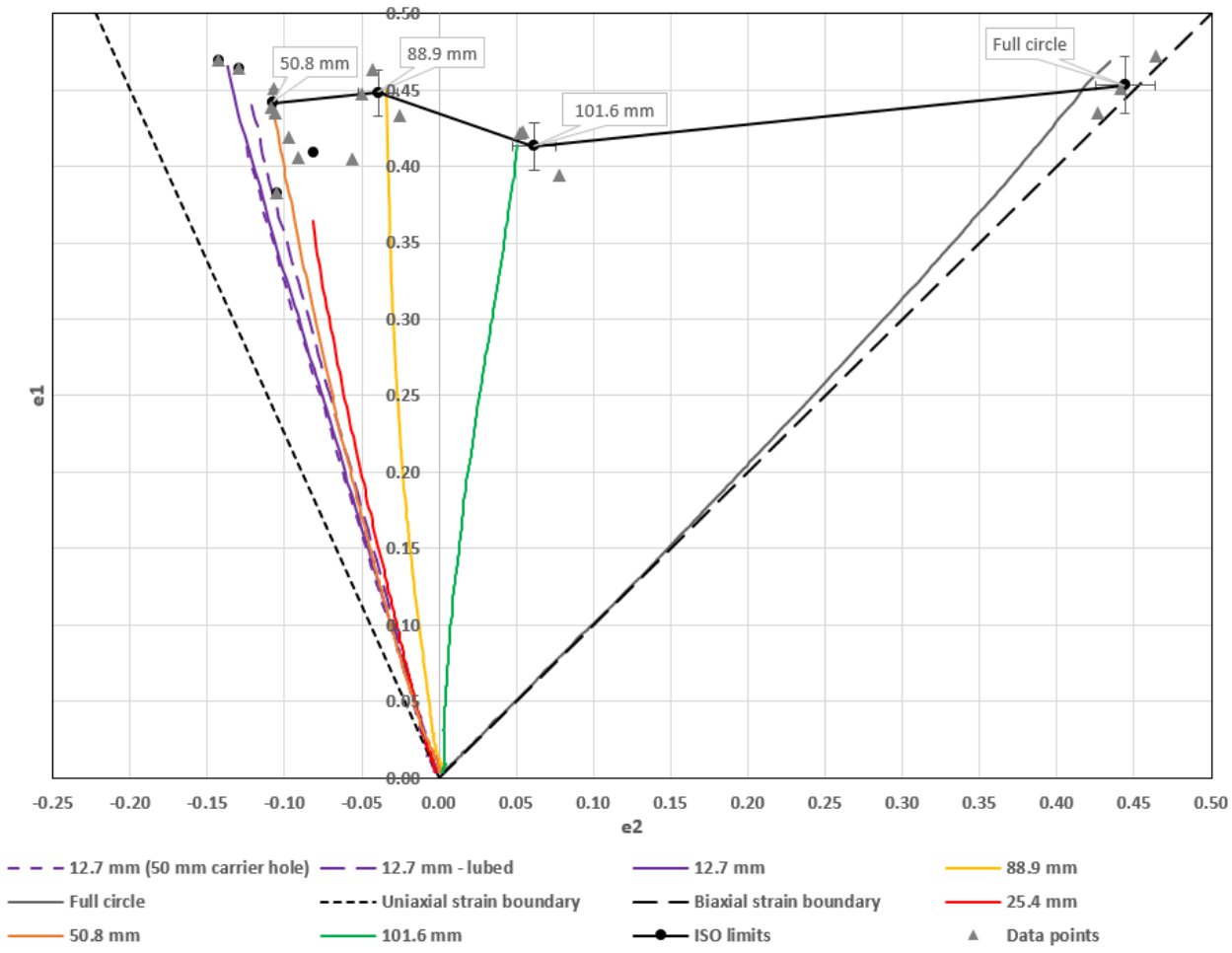

Figure 81: Strain paths of PHS sample geometries and their corresponding FLC using the hybrid Marciniak-Nakazima test. The necking limit strains of the FLC are determined using the ISO method. Error bars correspond to the sample standard deviation of each necking limit strain. Nominal punch speed: 60 mm/s. Lubrication: 3 sheets of 0.127 mm thick Teflon between punch and carrier blank. Clamping time: 3 seconds. R-value: 0.8

5.4. Comparison between Nakazima, Marciniak, and Hybrid Test Formability Limits

The FLCs generated using the Nakazima, Marciniak, and hybrid formability tests were compared in Figure 82. The FLCs obtained from the Marciniak and hybrid tests spanned from near-uniaxial to equibiaxial deformation, with similar necking limit strains using the 50.8 mm gage width

(negative minor strain). On the other hand, the hybrid punch achieved higher necking limits for plane strain and equibiaxial strain conditions compared to the Marciniak punch. This was likely caused by the effect of bending using the hybrid punch, which delayed the onset of necking and increased the forming limit strains [63]. Due to the location of necking occurring away from the PHS sample apex, the Nakazima FLC spanned a narrow range of minor strain that was close to plane strain condition for all sample widths. Nonetheless, the limit strains using the Nakazima test were similar to those obtained using the hybrid punch; both punches induced bending due to punch curvature.

The Marciniak test produced the lowest limit strains because it was consistent with in-plane stretching without bending nor tool contact pressure that increased the limit strains.

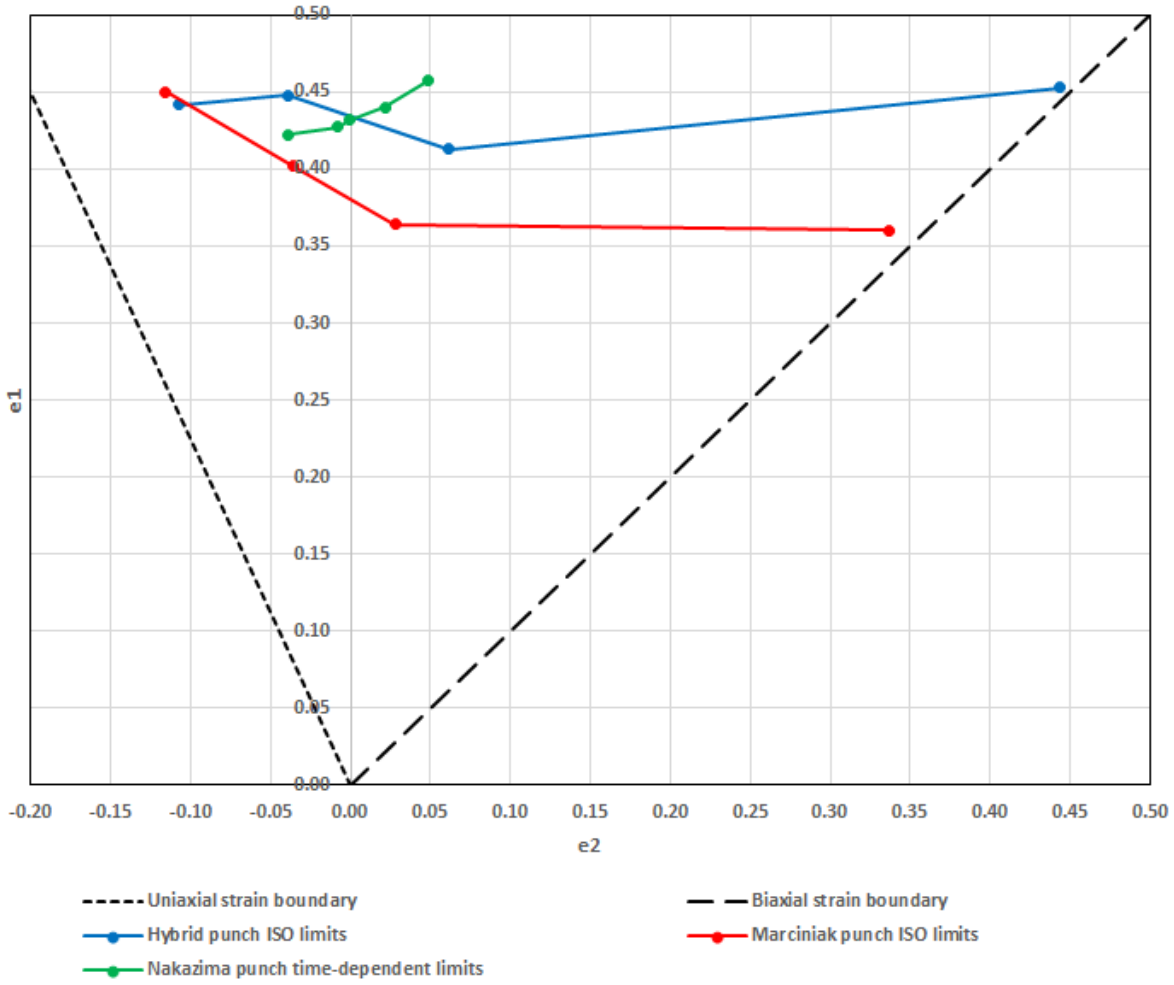

Figure 82: Comparison between FLCs obtained using Nakazima, Marciniak, and hybrid tests. The Nakazima FLC spans a much narrower range of minor strain than Marciniak and hybrid tests. Nominal punch speed: 60 mm/s. Lubrication: 3 sheets of 0.127 mm thick Teflon between punch and carrier blank (Marciniak and hybrid tests only). Clamping time: 3 seconds.

5.5. Comparison of formability limits for PHS1800, PHS1500 (AS150), and PHS1500 (AS80)

PHS1500 is the most commonly used hot stamped steel grade and is a predecessor of PHS1800, representing a baseline for the formability of PHS1800. Here, the formability of PHS1500 and

PHS1800 were compared. Two variants of PHS1500 were considered, with coating densities of 150 g/m^2 (the same coating density as on the PHS1800) and a lighter 80 g/m^2. For this comparison, the Marciniak punch geometry was adopted in view of its lack of bending effects, as discussed in Section 5.2.1.

For comparison purposes, identical forming conditions were considered, using a clamping time of 3 seconds, a mild steel carrier blank with a 32 mm center hole diameter, and a maximum punch velocity of 100 mm/s. Compared to the PHS1800 FLC, the PHS1500 variants exhibited slightly higher magnitudes of major limit strain for the full range of minor strain considered, as shown in Figure 83. Thus, the higher tensile strength of the PHS1800 grade (after quenching) came at the expense of a slightly lower FLC compared to PHS1500.

The effect of coating weight on formability could be assessed by comparing the FLCs for the two PHS1500 variants. In uniaxial and equibiaxial stretching, both PHS1500 variants showed similar limit strains.

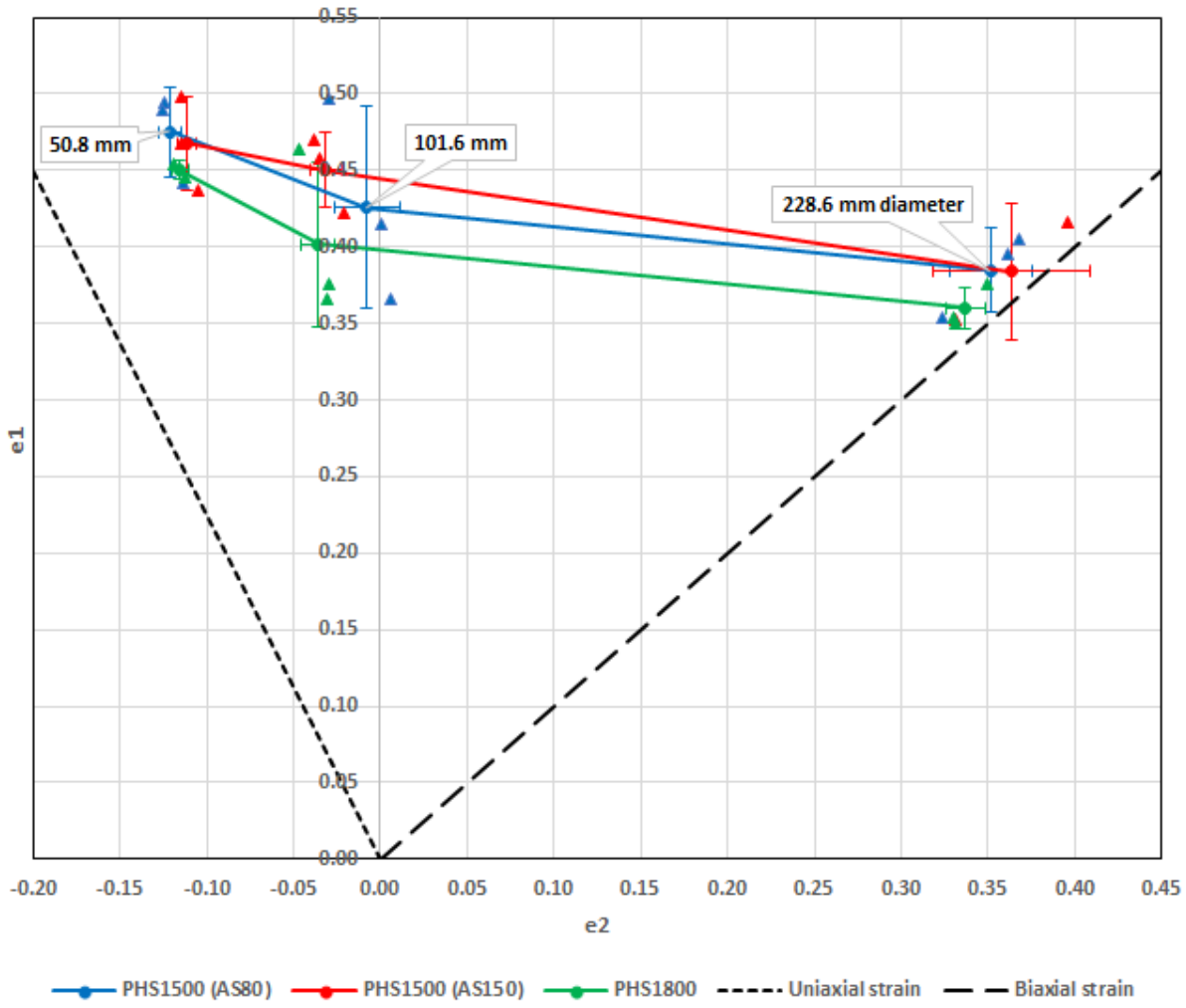

Figure 83: ISO necking limit strains producing FLCs for PHS1800, PHS1500 (AS80), and PHS1500 (AS150) in the Marciniak test. Error bars correspond to the sample standard deviation of each necking limit strain. Nominal punch speed: 60 mm/s. Lubrication: 3 sheets of 0.127 mm thick Teflon between punch and carrier blank. Clamping time: 3 seconds. R-value: 0.8

The punch heights at necking and fracture were determined with DIC and stroke-time data in Section 3.5.2. The resulting necking limit punch heights of each PHS variant are plotted in Figure 84. The resulting fracture punch heights of each PHS variant are also plotted in Figure 84.

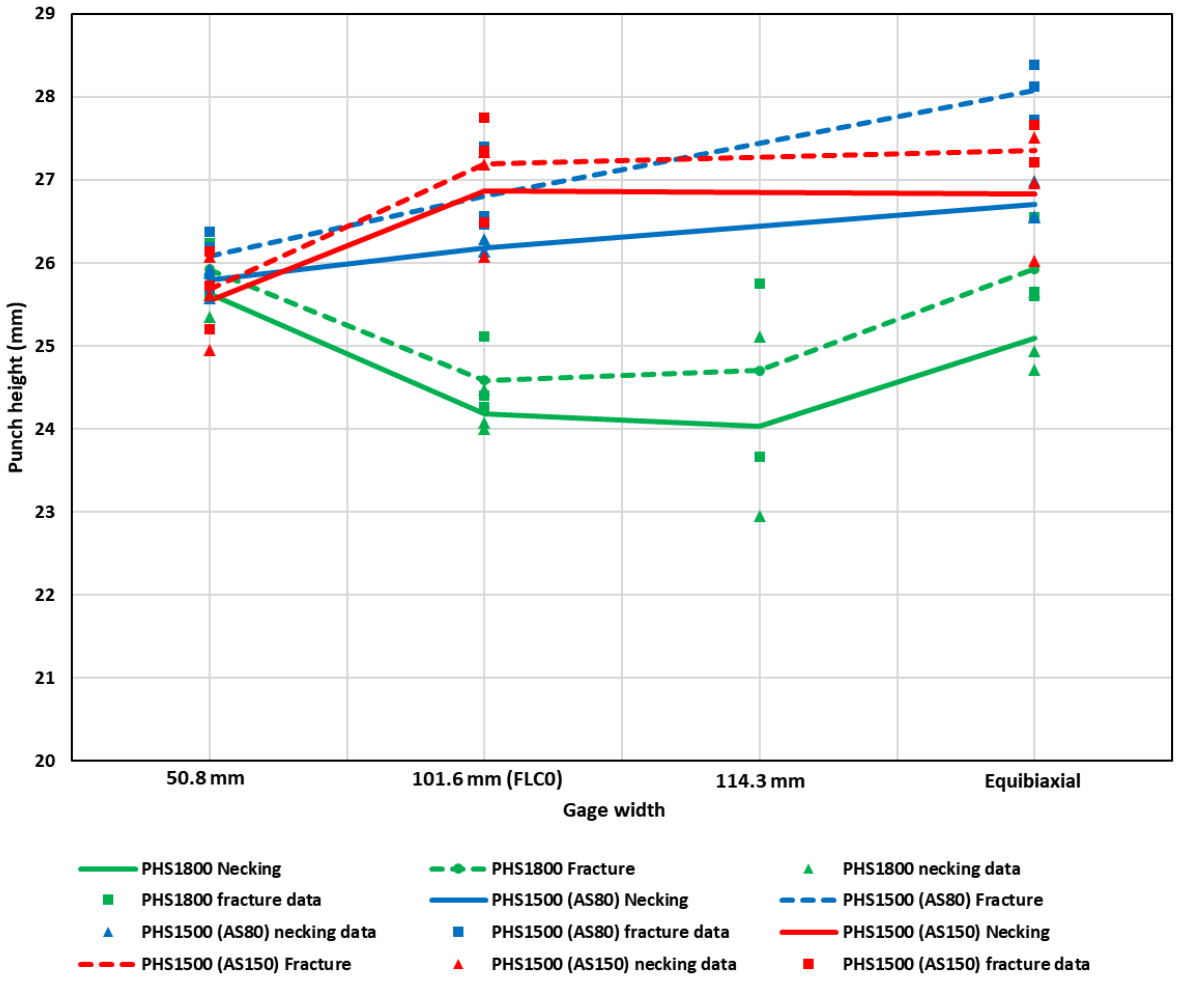

Figure 84: Marciniak punch height at necking limit and fracture of PHS1500 and PHS1800. Each average punch height (solid line) is obtained with 3 repeat tests (triangles for necking and squares for fracture). Nominal punch speed: 60 mm/s. Lubrication: 3 sheets of 0.127 mm thick Teflon between punch and carrier blank. Clamping time: 3 seconds.

As expected, the PHS1800 with its slightly lower limit strains also had lower average punch heights relative to the PHS1500 variants (Figure 84). The reduced coating density of PHS1500 (AS80) caused slightly lower formability properties in plane strain compared to PHS1500 (AS150). As a result, the average punch heights at the onset of necking in Figure 84 correlated with the average forming limit strains in Figure 83.

The average punch heights measured at the start of surface fracture followed closely the trend of their corresponding necking limit punch heights and featured higher magnitudes as expected. In uniaxial stretching with the 50.8 mm gage width, all PHS variants featured similar average punch heights at fracture. For the plane strain samples, the average punch heights at fracture followed the same order as their corresponding average punch heights at necking and ISO limit strains. In equibiaxial deformation, PHS1800 still retained the lowest average punch height at fracture.

6. Forming Simulation Results and Discussion

Select numerical simulations of the formability tests were developed using LS-DYNA to evaluate the accuracy of the material models. The goal of this effort was to provide greater insight into the tests and to develop a simulation platform for future development of hot stamping processes.

For the Nakazima test, only the 25.4 mm gage width was considered. For the Marciniak test and hybrid Nakazima-Marciniak punch simulations, gage widths of 25.4 mm, 101.6 mm, 114.3 mm, and 228.6 mm were considered.

6.1. Nakazima Test Predictions

Predictions for the hot stamping Nakazima test with a 25.4 mm width sample geometry are shown in Figure 85. At a punch displacement of 30 mm after contacting the sample, the area of the sample with the highest major strain in Figure 85a was predicted to be away from the punch center and to be closer to the die entry radius. This location corresponded to the necking location observed in the experimental tests, as shown in Figure 85b. It can be seen from comparison of the two figures that the predicted and measured strain distributions were similar.

The predicted and measured temperature-time histories at the apex of the Nakazima sample are shown in Figure 86. At the dome height corresponding to the experimentally measured limit strain, the predicted apex temperature decreased to 825°C. This is in the range of the corresponding

experimental value at the same elapsed time of 0.72 seconds from the start of the forming stroke (Figure 86). It is recognized that there were differences in the predicted and measured cooling rates. However, attempts to resolve these differences were left for future work, because attention shifted from Nakazima to Marciniak predictions due to the more desirable characteristics of the Marciniak test.

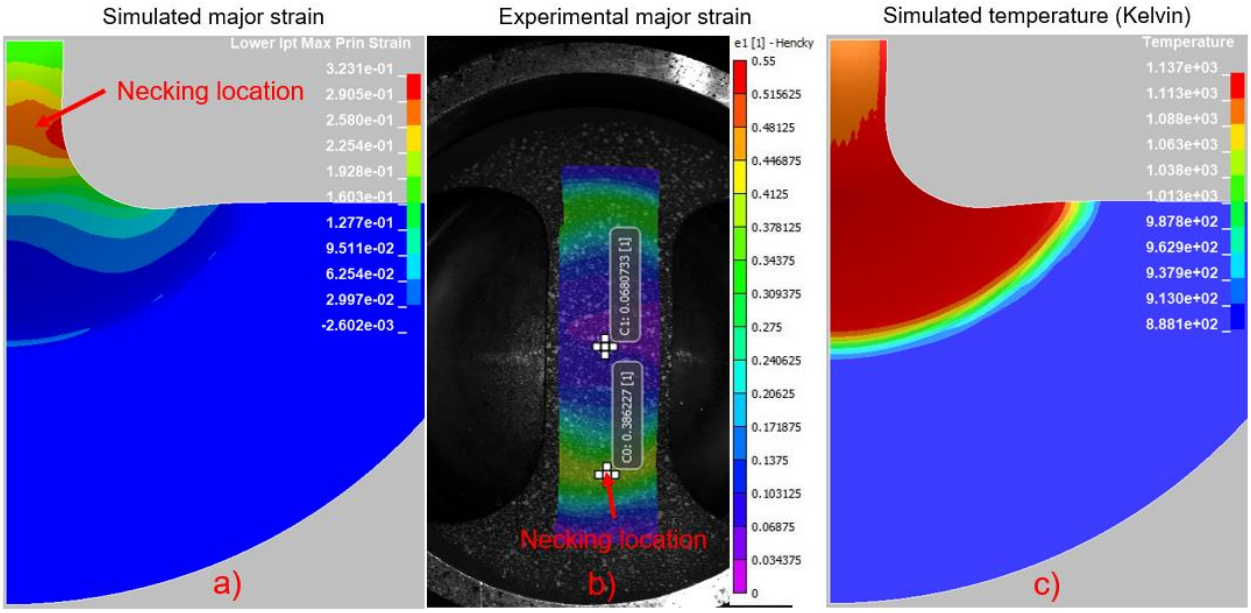

Figure 85: a) Simulated major strain profile of 25.4 mm width sample after a punch displacement of 30 mm. b) Experimental major strain profile. c) Simulated temperature profile. Nominal punch speed: 60 mm/s. Clamping time: 0 second. Lubrication: None

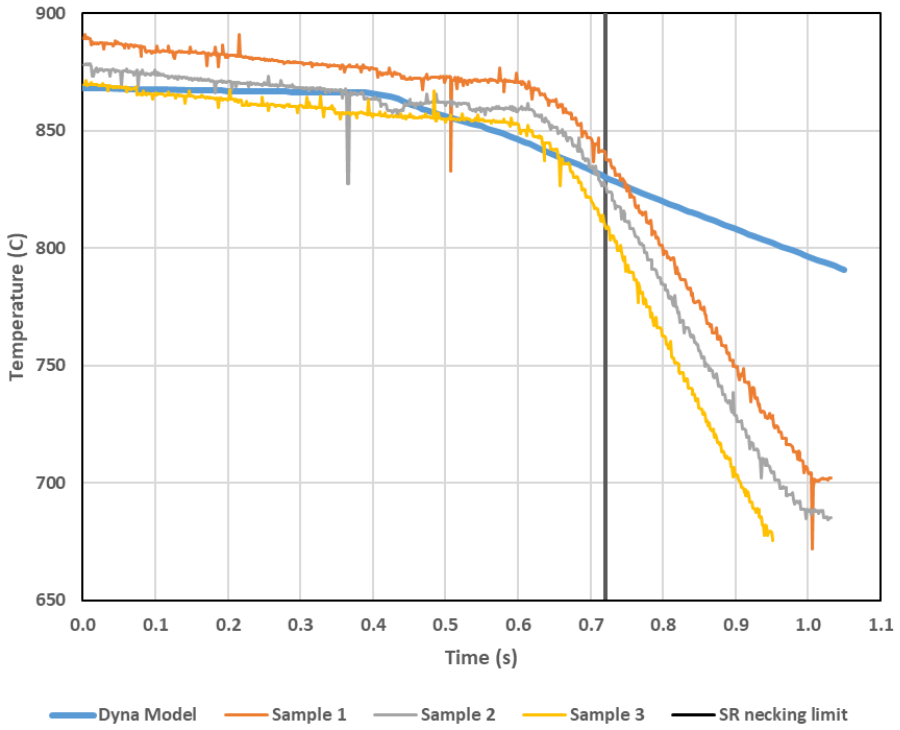

Figure 86: 25.4 mm gage Nakazima sample apex temperature-time history using a room temperature punch. Nominal punch speed: 60 mm/s. Clamping time: 0 second. Lubrication: None

Figure 85c shows the spatial variation of temperature within the Nakazima sample at the punch displacement corresponding to the onset of necking in the tests. It is evident that the temperature at the punch apex was lower than that in the unsupported region of the sample. The higher temperature in this region was the primary cause of localization away from the punch apex.

6.2. Marciniak Punch Test Predictions

This section presents the predictions for the Marcinicak punch test, including the temperature distribution, strain paths and location of necking.

6.2.1. Predicted Temperature Distribution

The use of a carrier blank prevented direct contact between the punch and PHS sample as discussed in Section 2.3.1. In addition, the carrier absorbed thermal energy from the PHS sample during the clamping time of 3 seconds (the clamping time adopted in the model) to produce a desired temperature profile with the highest temperature at the specimen center, as seen in Figure 87. The center hole of the carrier prevented contact and limited cooling at the central region of the PHS sample, while the peripheral area conducted heat into the carrier blank.

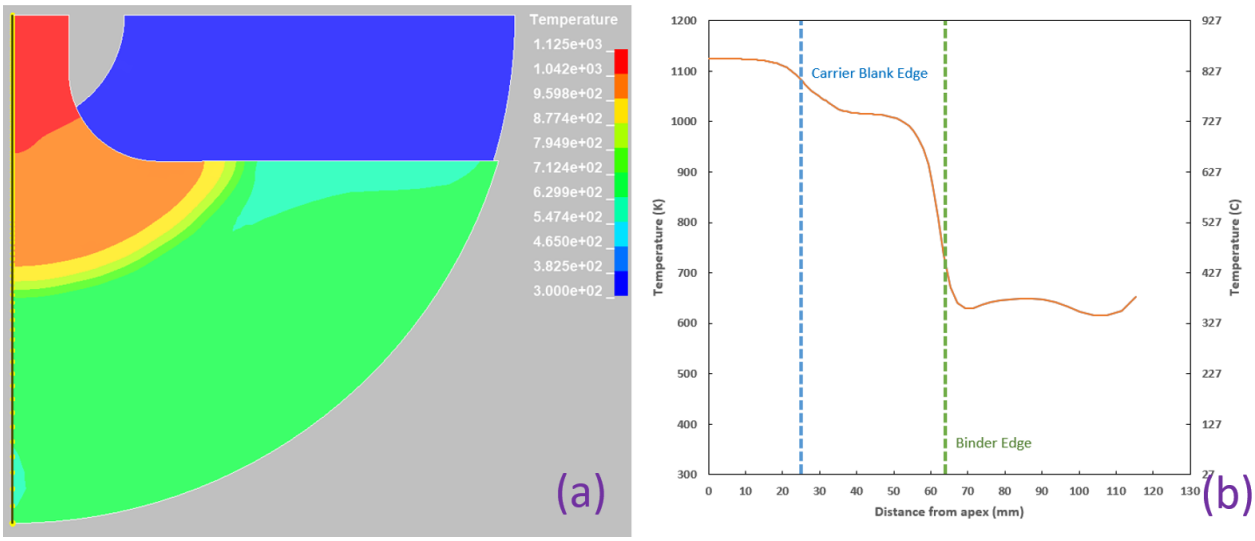

Figure 87: (a) Predicted temperature distribution within the 25.4 mm PHS sample after a clamping time of 3 seconds. (b) Temperature from the sample apex to its outer perimeter extracted from the vertical axis of symmetry.

Figure 88 shows the temperature profile of the carrier blank which increased in temperature at the contact area with the PHS sample. The elevated temperature contours corresponded to the outline of the PHS sample, thus demonstrating the significance of conduction heat transfer from PHS sample to the carrier blank. The area of the PHS sample that was clamped between binder and die

exhibited the lowest temperature in Figure 87, because the high clamping pressure produced a high conduction heat transfer rate (see Table 6). In contrast, the high thermal conductivity in the clamped area resulted in a corresponding high carrier blank temperature, as seen in Figure 88.

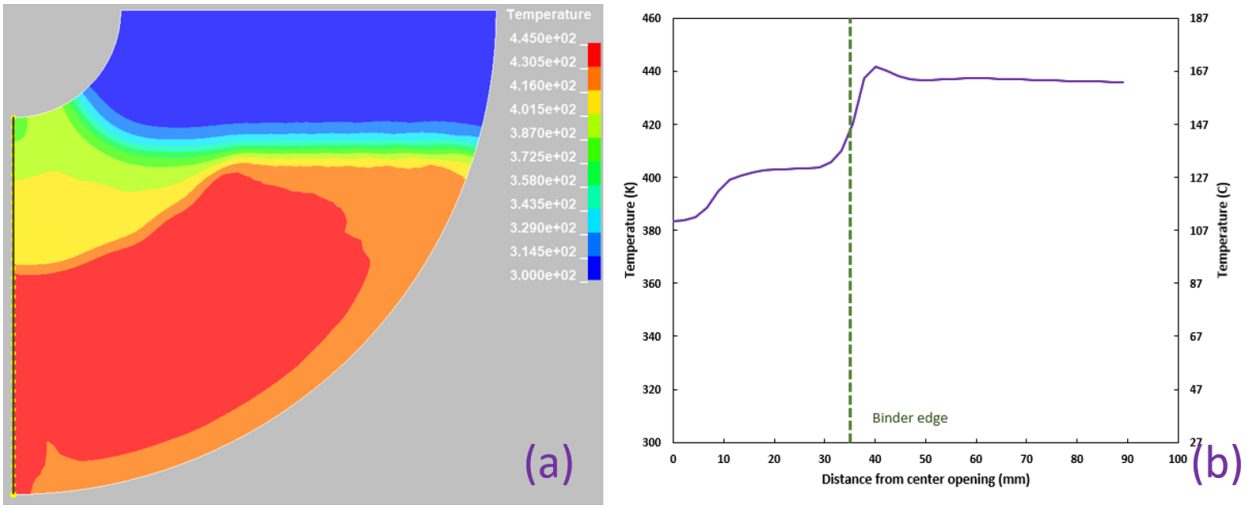

Figure 88: (a) Simulated temperature profile of the carrier blank (supporting a 25.4 mm PHS sample) after a clamping time of 3 seconds. (b) Temperature from the center hole edge to the outer perimeter extracted from the vertical axis of symmetry.

The effect of the clamping time duration is shown in Figure 89. As the clamping period increased, the temperatures in the clamped region as well as in the unsupported region of the blank outside of the punch were reduced. The cooling rate at the center of the blank was sufficiently slow that a 3 second clamping period did not significantly affect the temperature at the centre. In Figure 89, the higher center temperature of the case with clamped quenching compared to the case without it was unexpected. It was likely caused by a source of error from numerical data noise.

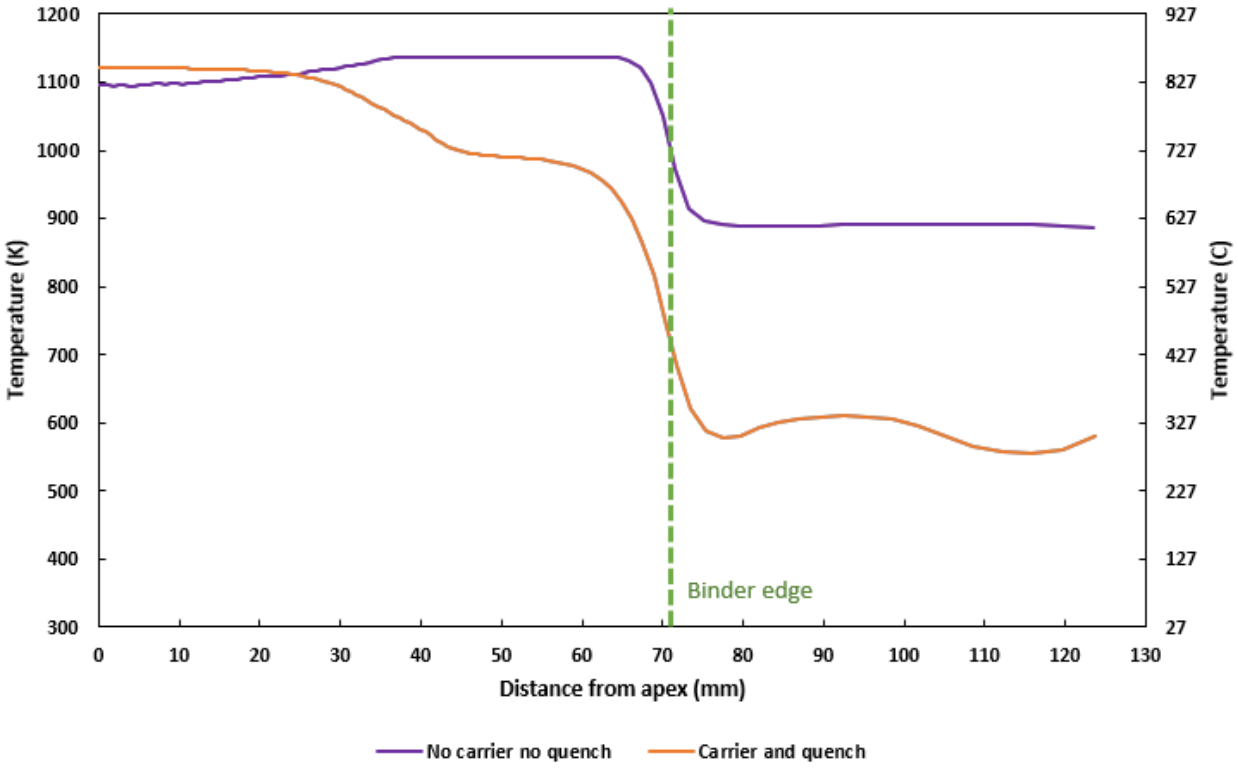

Figure 89: Impact of clamping time on PHS sample temperature distribution at the onset of necking (taken at the vertical axis of symmetry). Maximum punch speed: 100 mm/s.

6.2.2. Predicted Necking Location – Marciniak Test

Through friction reduction and temperature control of the sample, necking was predicted to initiate within the central region of each PHS sample geometry, taken for the purposes of this work as the region of strain localization seen in the contour plots of Figure 90. These locations of strain concentration corresponded to the observed necking locations at sample center for all gage widths in Figure 75 of Chapter 5.

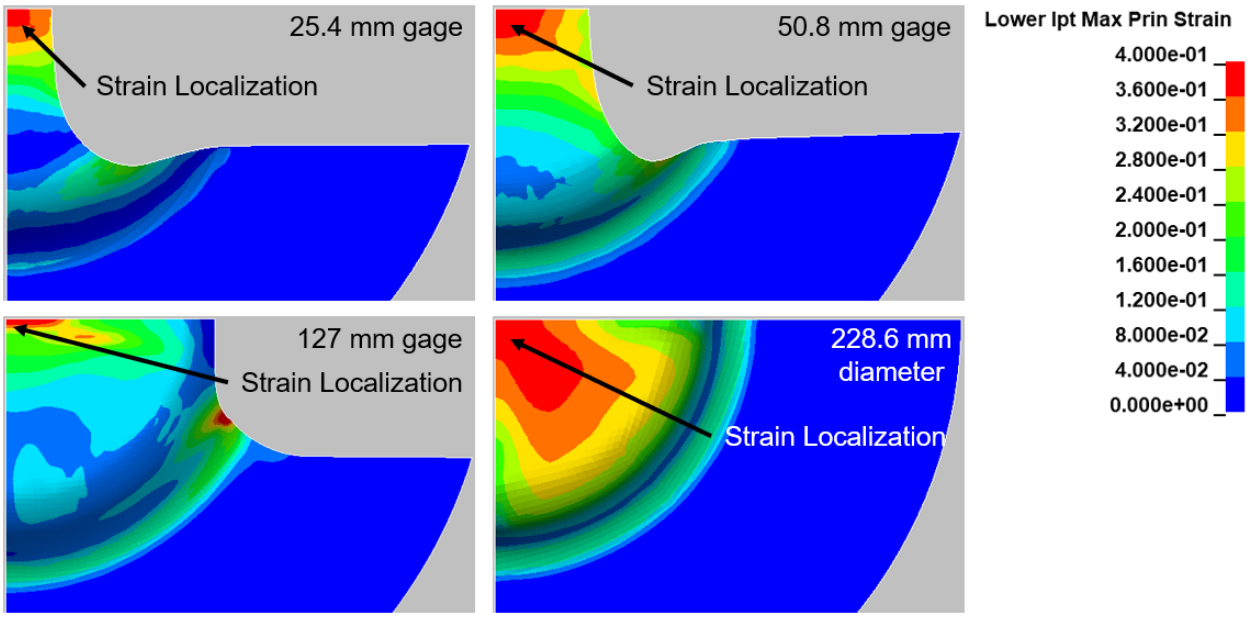

Figure 90: Major strain profile of PHS sample geometries at the onset of necking during the Marciniak test. The highest major strain is localized at the center of each sample geometry and represents the expected necking location.

6.2.3. Predicted Strain Paths – Marciniak Test

The predicted strain paths for the 25.4 mm, 50.8 mm, 101.6 mm, and 228.6 mm gage widths spanned the desired FLC range from uniaxial to equibiaxial deformation, as shown in Figure 91. Both the 25.4 mm and 50.8 mm samples were predicted to generate strain paths close to uniaxial deformation. According to Merklein and Lechler [6], the R-value of PHS was estimated to be 0.8, which was used to determine the uniaxial and biaxial strain boundaries according to equations (13) and (14) respectively.

$$Uniaxial\ strain\ boundary\text{: } \frac{e_2}{e_1} = -\frac{R}{1+R} \tag{13}$$

$$Biaxial\ strain\ boundary\text{: } \frac{e_2}{e_1} = 1 \tag{14}$$

Plane strain conditions, corresponding to the FLC0, were predicted to occur with the 101.6 mm gage width. The plotted strain paths were terminated at the respective major strain values corresponding to the onset of localization in the model. It is emphasized that this strain level did not represent a material forming limit since it was largely affected by numerical artefacts such as element size. The strain paths were mostly linear, which was expected for Marciniak test results. The flat top section of the punch only resulted in tensile force at the blank center and did not induce bending in the through-thickness direction. These predicted strain paths are similar to the measured strain paths from uniaxial to equibiaxial deformation in Chapter 5.

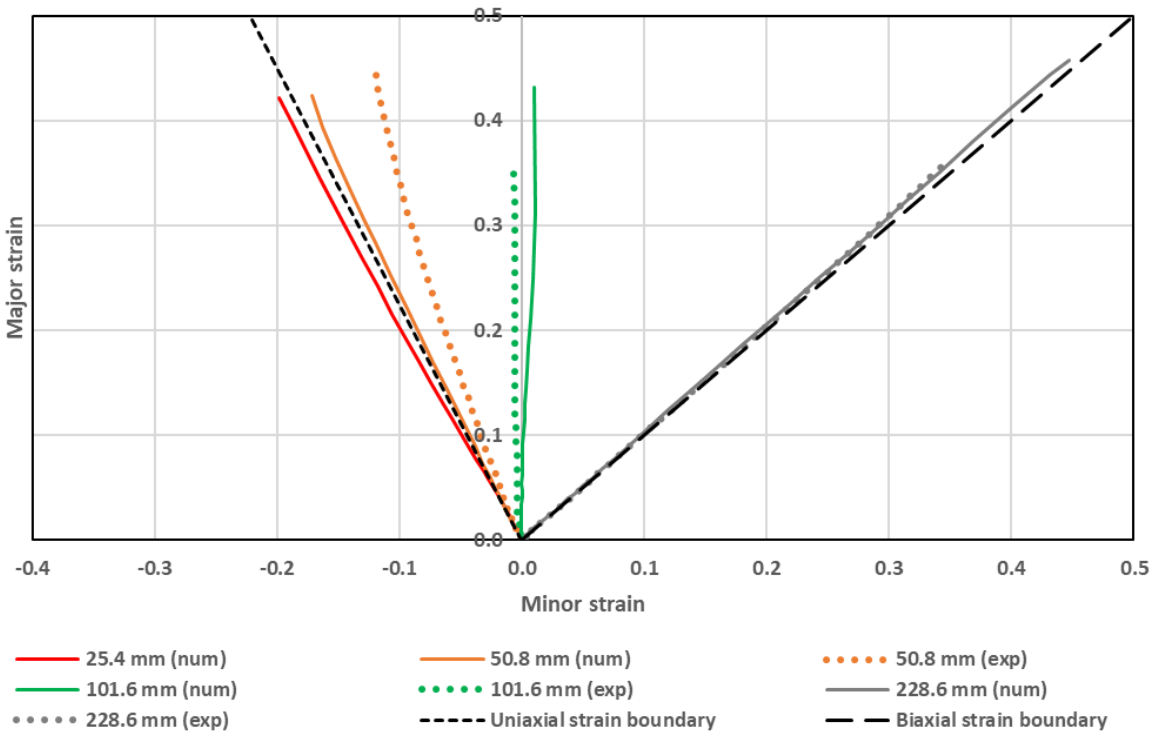

Figure 91: Simulated and experimental strain paths at the punch center using a Marciniak punch. Nominal punch speed: 60 mm/s. Clamping time: 3 seconds. R-value = 0.8

6.3. Hybrid Punch Test Predictions

The hybrid test used a modification of the Marciniak punch with a geometry that featured characteristics of the Nakazima test, such as a large shoulder radius, as well as those of the Marciniak test, such a flat top section.

6.3.1. Predicted Necking Location

Using the same simulation parameters as the Marciniak test, the hybrid punch geometry in Figure 48 replaced the Marciniak punch and featured a smaller flat top section to prevent contact with the

PHS sample during clamping. Thus, the benefit of center expansion through the carrier blank and the promotion of highest temperature at the PHS sample apex using a clamping time of 3 seconds still resulted in the predicted onset of necking to occur at the apex for each sample geometry, as shown in Figure 92. This outcome corresponded to the experimental observations in Section 5.3, in which strain localization at PHS sample center induced the onset of necking.

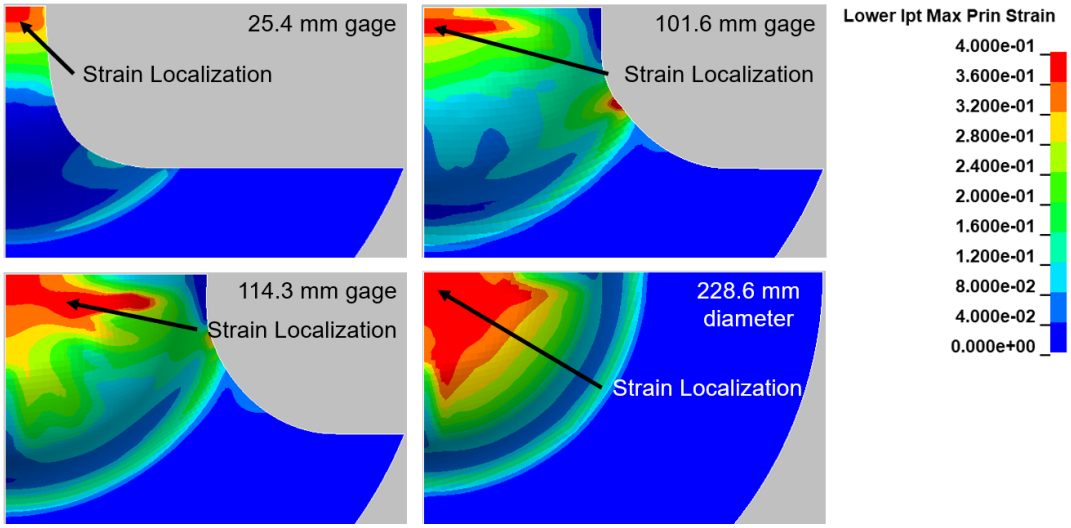

Figure 92: Major strain profile of PHS sample geometries at the onset of necking during the hybrid test. The highest major strain is localized near the apex of each sample geometry and represent the expected necking location.

6.3.2. Predicted Strain Paths

In Figure 93, the predicted strain paths spanned the entire FLC range from uniaxial to equibiaxial deformation. The increased curvature at the hybrid punch shoulder compared to the Marciniak punch caused the strain paths to become less linear. As a result, the hybrid punch was expected to cover the entire FLC range like the Marciniak punch while retaining some bending deformation

inherent to the hemispherical Nakazima punch. These predictions were confirmed by their corresponding experimental results with the hybrid Nakazima-Marciniak punch, in Figure 93.

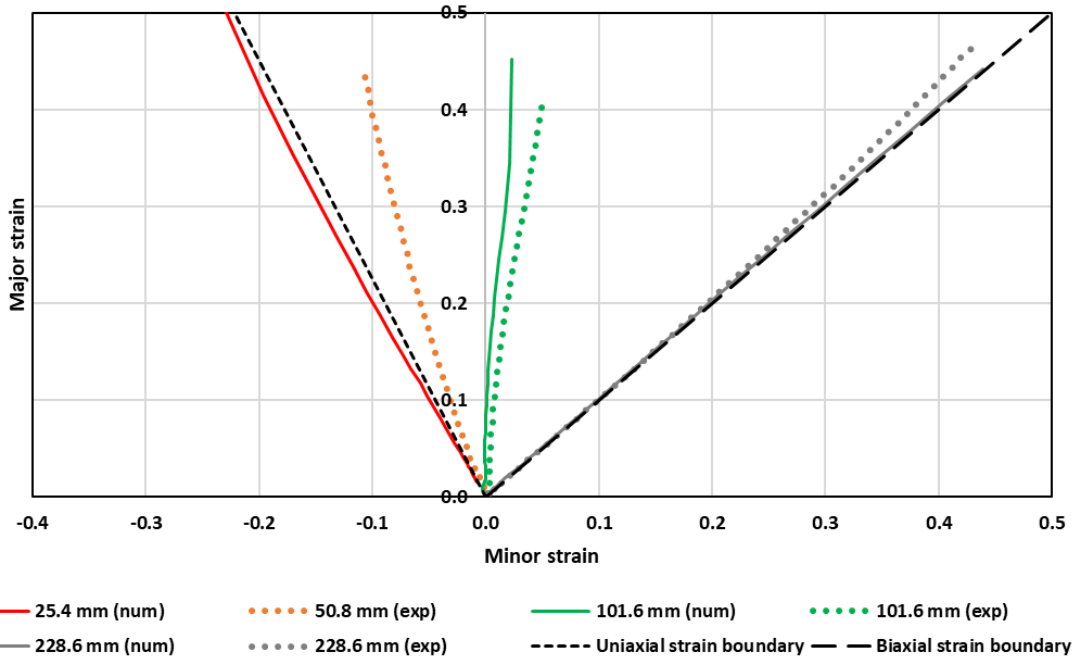

Figure 93: Predicted strain paths at the punch center using a Marciniak punch. Nominal punch speed: 60 mm/s. Clamping time: 3 seconds. R-value = 0.8

Conclusions

Friction characterization of Al-Si coated PHS under hot stamping conditions with the TCT:

1. The CoF of PHS1800-AS150 under die quenching conditions and a sliding speed of 20 mm/s ranged from 0.31 to 0.41 for contact pressures of 5 MPa to 30 MPa, respectively.
2. For PHS1800-AS150, a variation in sliding speed between 10 mm/s and 38 mm/s under a constant contact pressure of 15 MPa did not significantly affect the CoF, which ranged from 0.37 to 0.41 with overlapping 95% confidence intervals.
3. Repeated wear of friction cups against new PHS1800-AS150 specimens was assumed to represent tool wear under a limited range of production runs for up to 10 repeats tests. Beyond the first test, the average CoF and surface roughness of the worn friction cups remained constant.
4. At a constant sliding speed of 20 mm/s and a contact pressure of 30 MPa, PHS1800-AS150 featured the lowest average CoF (0.414) among the PHS variants. This was likely caused by its higher tensile strength of 1800 MPa compared to 1500 MPa for PHS1500.
5. The PHS1500-AS150 featured a lower average CoF (0.458) than the PHS1500-AS80 (0.475), which is attributed to its thicker Al-Si coating.

Formability characterization of Al-Si coated PHS under hot stamping conditions:

6. Due to the high level of friction and rapid quenching at the center of the PHS samples, necking within the Nakazima test occurred well away from the centre of the specimen, resulting in plane strain conditions for all gage widths.
7. The Marciniak test, performed under hot stamping conditions using a mild steel carrier blank with a center hole to prevent contact between the punch and blank, resulted in necking at the center of the specimen. Using a clamping quench time of 3 seconds prior to the forming stroke resulted in necking limit strains under strain states ranging from uniaxial to equibiaxial deformation. The resulting FLDs featured linear strain paths with necking limit major strains for PHS1800-AS150 above 0.35 for all strain states.
8. The hybrid Nakazima-Marciniak test produced a similar range of forming limit strains to the Marciniak test with slightly less linear strain paths.
9. In the Marciniak tests, both PHS1500 variants (AS80 and AS150) produced higher average necking limit strains than PHS1800 over their entire FLC range. In plane strain, PHS1500-AS80 and PHS1500-AS150 exhibited major necking limit strains of 0.43 and 0.45, respectively, compared to that of PHS1800 at 0.40. In equibiaxial strain, PHS1500-AS80 and PHS1500-AS150 both featured major/minor necking limit strains of 0.38 compared to that of PHS1800 at 0.36. The coating weight did not have a significant effect on the limit strain levels for the two PHS1500 variants.
10. During the Marciniak test forming stroke, the effective Von Mises strain rates at the necking locations increased as the nominal effective Von Mises strain increased for all

PHS gage widths. The cooling rate remained constant during the forming stroke for all gage widths and varied from 21.8°C/s to 24.5°C/s. Interestingly, the cooling rate was not affected by the PHS sample gage width.

11. Among the three formability tests, the Marciniak test produced the lowest necking limit strains. Therefore, the Marciniak test FLC is the most conservative limit strain locus for formability assessment.
12. An FEM model has been developed to predict the deformation behaviour of PHS1800 for each formability test and sample gage width. This FEM model accurately represented the direct hot stamping process for PHS.

References

[1] S. A. Pradeep, R. K. Iyer, H. Kazan, and S. Pilla, “Automotive Applications of Plastics: Past, Present, and Future,” in *Applied Plastics Engineering Handbook*, Elsevier, 2017, pp. 651–673. doi: 10.1016/B978-0-323-39040-8.00031-6.

[2] R. Roth, J. Clark, and A. Kelkar, “Automobile bodies: Can aluminum be an economical alternative to steel?,” *JOM*, vol. 53, no. 8, pp. 28–32, Aug. 2001, doi: 10.1007/s11837-001-0131-7.

[3] J. Hardell, E. Kassfeldt, and B. Prakash, “Friction and wear behaviour of high strength boron steel at elevated temperatures of up to 800 ◦C,” *Wear*, vol. 264, no. 9–10, p. p.788-799, 2008, doi: 10.1016/j.wear.2006.12.077.

[4] K. Kumar Dama, V. Suresh Babu, and R. N. Rao, “State of the Art on Automotive Lightweight Body-in-White Design,” *Materials Today: Proceedings*, vol. 5, no. 10, pp. 20966–20971, 2018, doi: 10.1016/j.matpr.2018.06.486.

[5] P. Chen and M. Koç, “Simulation of springback variation in forming of advanced high strength steels,” *Journal of Materials Processing Technology*, vol. 190, no. 1–3, pp. 189–198, Jul. 2007, doi: 10.1016/j.jmatprotec.2007.02.046.

[6] M. Merklein and J. Lechler, “Investigation of the thermo-mechanical properties of hot stamping steels,” *Journal of Materials Processing Technology*, vol. 177, no. 1–3, pp. 452–455, Jul. 2006, doi: 10.1016/j.jmatprotec.2006.03.233.

[7] Eriksson K, Lindgren S and Muskos P, “Hot stamping of 1800-2000 MPa steels,” in *7th Int. Conf. on Hot Sheet Metal Forming High-Performance Steel CHS2*, 2019th ed.Lulea: CHS2, 2019, pp. 447–454.

[8] Malek Naderi, “Hot Stamping of Ultra High Strength Steels,” Thesis for Master of Science, Westfälischen Technischen Hochschule Aachen, Teheran, Iran, 2007.

[9] ArcelorMittal, “Usibor® and Ductibor®,” *Steels for hot stamping - Usibor® and Ductibor®*. https://automotive.arcelormittal.com/products/flat/PHS/usibor_ductibor (accessed Apr. 07, 2021).

[10] “ArcelorMittal 3D car configurator.” ArcelorMittal. [Online]. Available: https://automotive.arcelormittal.com/s-in_motion_solutions/3D_solutions_catalogue#?mode=5&solutions=AA0+AB0+AC0+AW0+AE0+AF0+AG0+AH0+AI0+AL0+AM0+AN0+AO0+AP0+AQ0+AR0+AS0+AU0+BA0+BB0+BC0+BD0+BE0

[11] P. Hein and J. Wilsius, “Status and Innovation Trends in Hot Stamping of USIBOR 1500 P,” *steel research international*, vol. 79, no. 2, pp. 85–91, Feb. 2008, doi: 10.1002/srin.200806321.

[12] M. Maikranz-Valentin, U. Weidig, U. Schoof, H.-H. Becker, and K. Steinhoff, “Components with Optimised Properties due to Advanced Thermo-mechanical Process Strategies in Hot Sheet Metal Forming,” *steel research international*, vol. 79, no. 2, pp. 92–97, Feb. 2008, doi: 10.1002/srin.200806322.

[13] K. Mori and Y. Okuda, “Tailor die quenching in hot stamping for producing ultra-high strength steel formed parts having strength distribution,” *CIRP Annals*, vol. 59, no. 1, pp. 291–294, 2010, doi: 10.1016/j.cirp.2010.03.107.

[14] M. Naderi, M. Ketabchi, M. Abbasi, and W. Bleck, “Analysis of microstructure and mechanical properties of different high strength carbon steels after hot stamping,” *Journal of Materials Processing Technology*, vol. 211, no. 6, pp. 1117–1125, Jun. 2011, doi: 10.1016/j.jmatprotec.2011.01.015.

[15] H. Karbasian and A. E. Tekkaya, “A review on hot stamping,” *Journal of Materials Processing Technology*, vol. 210, no. 15, pp. 2103–2118, Nov. 2010, doi: 10.1016/j.jmatprotec.2010.07.019.

[16] S. Lu *et al.*, “Constitutive characterization of an 1800 MPa press hardening steel under hot stamping conditions,” *IOP Conf. Ser.: Mater. Sci. Eng.*, vol. 1157, no. 1, p. 012012, Jun. 2021, doi: 10.1088/1757-899X/1157/1/012012.

[17] Taylan Altan, “R&D Update: Hot-stamping boron-alloyed steels for automotive parts - Part I Process methods and uses,” *Stamping Journal*, Feb. 2007, [Online]. Available:

https://www.thefabricator.com/stampingjournal/article/stamping/hot-stamping-boron-alloyed-steels-for-automotive-parts

[18] M. Merklein, J. Lechler, and T. Stoehr, “CHARACTERIZATION OF TRIBOLOGICAL AND THERMAL PROPERTIES OF METALLIC COATINGS FOR HOT STAMPING BORON-MANGANESE STEELS,” p. 10, 2008.

[19] W. F. Hosford and R. M. Caddell, *Metal forming: mechanics and metallurgy*, 4. ed. Cambridge: Cambridge Univ. Press, 2014.

[20] P. Åkerström, “Modelling and simulation of hot stamping,” Doctoral Thesis, Lule°a University of Technology, Lule°a, Sweden, 2006.

[21] M.-G. Lee, S.-J. Kim, H. N. Han, and W. C. Jeong, “Application of hot press forming process to manufacture an automotive part and its finite element analysis considering phase transformation plasticity,” *International Journal of Mechanical Sciences*, vol. 51, no. 11–12, pp. 888–898, Nov. 2009, doi: 10.1016/j.ijmecsci.2009.09.030.

[22] K. Kusumi, J. Maki, and N. Nomura, “Formability and FEM Simulation of Steel Sheets in the Hot Stamping Process,” no. 103, p. 8, 2013.

[23] Z. W. Xing, J. Bao, and Y. Y. Yang, “Numerical simulation of hot stamping of quenchable boron steel,” *Materials Science and Engineering: A*, vol. 499, no. 1–2, pp. 28–31, Jan. 2009, doi: 10.1016/j.msea.2007.09.102.

[24] J. Noder and C. Butcher, “A comparative investigation into the influence of the constitutive model on the prediction of in-plane formability for Nakazima and Marciniak tests,” *International Journal of Mechanical Sciences*, vol. 163, p. 105138, Nov. 2019, doi: 10.1016/j.ijmecsci.2019.105138.

[25] International Standard, “ISO 12004-2 Metallic materials - Sheet and strip - Deterimination of forming-limit curves. Part 2: Determination of forming-limit curves in the laboratory.” Oct. 15, 2008.

[26] W. Volk and P. Hora, “New algorithm for a robust user-independent evaluation of beginning instability for the experimental FLC determination,” *Int J Mater Form*, vol. 4, no. 3, pp. 339–346, Sep. 2011, doi: 10.1007/s12289-010-1012-9.

[27] S. DiCecco, C. Butcher, M. Worswick, E. Boettcher, E. Chu, and C. Shi, "Determination of forming limit diagrams of AA6013-T6 aluminum alloy sheet using a time and position dependent localized necking criterion," *IOP Conf. Ser.: Mater. Sci. Eng.*, vol. 159, p. 012009, Nov. 2016, doi: 10.1088/1757-899X/159/1/012009.

[28] J. Min, T. B. Stoughton, J. E. Carsley, and J. Lin, "An improved curvature method of detecting the onset of localized necking in Marciniak tests and its extension to Nakazima tests," *International Journal of Mechanical Sciences*, vol. 123, pp. 238–252, Apr. 2017, doi: 10.1016/j.ijmecsci.2017.02.011.

[29] F. F. Li, M. W. Fu, J. P. Lin, and X. N. Wang, "Experimental and theoretical study on the hot forming limit of 22MnB5 steel," *Int J Adv Manuf Technol*, vol. 71, no. 1–4, pp. 297–306, Mar. 2014, doi: 10.1007/s00170-013-5468-x.

[30] Cao Y, "Investigation of 22MnB5 forming limits in hot stamping process using ductile fracture criteria," Master's thesis, Tongji University, 2011.

[31] Yoann Dahan, Yvan Chastel, Patrick Duroux, Philipp Hein, Elisabeth Massoni, and Joël Wilsius, "Formability investigations for the hot stamping process," *IDDRG*, vol. Porto, Portugal, p. 8, Jun. 2006.

[32] P. F. Bariani, S. Bruschi, A. Ghiotti, and A. Turetta, "Testing formability in the hot stamping of HSS," *CIRP Annals*, vol. 57, p. 4, 2008, doi: 10.1016/j.cirp.2008.03.049.

[33] M. F. Shi, "Strain Hardening and Forming Limits of Automotive Steels," in *E International*, in 950700. Detroit, Michigan: SAE Technical Paper Series, Feb. 1995, p. 9.

[34] D. Y. Shi, L. Ying, P. Hu, J. D. Lu, X. Zhao, and W. Q. Liu, "Experimental and numerical determination of thermal forming limit diagrams (TFLD) of high strength steel 22MnB5," presented at the THE 11TH INTERNATIONAL CONFERENCE ON NUMERICAL METHODS IN INDUSTRIAL FORMING PROCESSES: NUMIFORM 2013, Shenyang, China, 2013, pp. 406–413. doi: 10.1063/1.4806853.

[35] R. Zhang, Z. Shi, V. A. Yardley, and J. Lin, "Experimental studies of necking and fracture limits of boron steel sheet under hot stamping conditions," *Journal of Materials Processing Technology*, vol. 302, p. 117481, Apr. 2022, doi: 10.1016/j.jmatprotec.2021.117481.

[36] E. Kardoulaki, J. Lin, D. Balint, and D. Farrugia, “Investigation of the effects of thermal gradients present in Gleeble high-temperature tensile tests on the strain state for free cutting steel,” *The Journal of Strain Analysis for Engineering Design*, vol. 49, no. 7, pp. 521–532, Oct. 2014, doi: 10.1177/0309324714531950.

[37] J. Hardell, B. Prakash, and K. Steinhoff, “High Temperature Tribological Studies on Surface Engineered Tool Steel and High Strength Boron Steel,” *Steel research international*, vol. 80, no. 9, pp. 665–670, 2009, doi: 10.2374/SRI09SP067.

[38] J. Venema, J. Hazrati, D. T. A. Matthews, R. A. Stegeman, and A. H. van den Boogaard, “The effects of temperature on friction and wear mechanisms during direct press hardening of Al-Si coated ultra-high strength steel,” *Wear*, vol. 406–407, pp. 149–155, Jul. 2018, doi: 10.1016/j.wear.2018.04.006.

[39] A. Yanagida and A. Azushima, “Evaluation of coefficients of friction in hot stamping by hot flat drawing test,” *CIRP annals*, vol. 58, no. 1, pp. 247–250, 2009, doi: 10.1016/j.cirp.2009.03.091.

[40] L. Pelcastre, J. Hardell, C. Courbon, and B. Prakash, “Tribological behaviour of Al-Si-coated ultra-high-strength steel during interaction with tool steel at elevated temperatures: Influence of tool steel surface topography parameters on galling,” *Proceedings of the Institution of Mechanical Engineers. Part B, Journal of engineering manufacture*, vol. 229, no. 8, pp. 1373–1384, 2015, doi: 10.1177/0954405414535920.

[41] L. Wang, “Modelling of friction for high temperature extrusion of aluminium alloys,” PhD thesis, Harbin Institute of Technology, China, 2012. Accessed: Apr. 08, 2021. [Online]. Available: https://repository.tudelft.nl/islandora/object/uuid%3A6f76d5c3-5cc2-4cdf-a2af-d6cb1323e289

[42] J. A. Schey and M. C. Shaw, “Tribology in Metalworking: Friction, Lubrication and Wear,” *Journal of tribology*, vol. 106, no. 1, pp. 174–174, 1984, doi: 10.1115/1.3260859.

[43] M. Geiger, M. Merklein, and C. Hoff, “Basic Investigations on the Hot Stamping Steel 22MnB5,” *AMR*, vol. 6–8, pp. 795–804, May 2005, doi: 10.4028/www.scientific.net/AMR.6-8.795.

[44] ArcelorMittal, “Inspection Certificate EN 10204-3.1,” Chemical Analysis 90/I137301/0.98//, May 2017.

[45] C. M. Klassen, J. Emmert, and K. J. Daun, “Effect of coating thickness on the in-situ reflectance and surface roughness of Al-Si coated 22MnB5 steel,” *Surface and Coatings Technology*, vol. 414, p. 127100, May 2021, doi: 10.1016/j.surfcoat.2021.127100.

[46] M. E. Palmieri, F. R. Galetta, and L. Tricarico, “Study of Tailored Hot Stamping Process on Advanced High-Strength Steels,” *JMMP*, vol. 6, no. 1, p. 11, Jan. 2022, doi: 10.3390/jmmp6010011.

[47] Claire Fonseca, “Test Certificate.” Element Cambridge, Mar. 16, 2021.

[48] D19 Committee, “Test Method for Elements in Water by Inductively-Coupled Plasma Atomic Emission Spectroscopy,” ASTM International. doi: 10.1520/D1976-20.

[49] E01 Committee, “Test Methods for Determination of Carbon, Sulfur, Nitrogen, and Oxygen in Steel, Iron, Nickel, and Cobalt Alloys by Various Combustion and Fusion Techniques,” ASTM International. doi: 10.1520/E1019-18.

[50] A. Bardelcik, M. J. Worswick, and M. A. Wells, “The influence of martensite, bainite and ferrite on the as-quenched constitutive response of simultaneously quenched and deformed boron steel – Experiments and model,” *Materials & Design*, vol. 55, pp. 509–525, Mar. 2014, doi: 10.1016/j.matdes.2013.10.014.

[51] J. Noder, “Characterization and simulation of warm forming of 6xxx and 7xxx series aluminum alloys,” University of Waterloo, Waterloo, Ontario, Canada, 2017.

[52] J. A. Schey, *Tribology in metalworking: friction, lubrication, and wear*. Metals Park, Ohio: American Society for Metals, 1983.

[53] Ryan George, “Personal communication,” 2017.

[54] X. Cao, X. Zhou, H. Wang, Z. Luo, and J. Duan, “Microstructures and mechanical properties of laser offset welded 5052 aluminum to press-hardened steel,” *Journal of Materials Research and Technology*, vol. 9, no. 3, pp. 5378–5390, May 2020, doi: 10.1016/j.jmrt.2020.03.064.

[56] Z. Deng and J. P. McGuire, “Development of novel forming limit curve testing method,” *IOP Conf. Ser.: Mater. Sci. Eng.*, vol. 418, p. 012049, Sep. 2018, doi: 10.1088/1757-899X/418/1/012049.

[57] H. Li, L. He, G. Zhao, and L. Zhang, “Constitutive relationships of hot stamping boron steel B1500HS based on the modified Arrhenius and Johnson–Cook model,” *Materials Science and Engineering: A*, vol. 580, pp. 330–348, Sep. 2013, doi: 10.1016/j.msea.2013.05.023.

[58] M. Worswick, “ME725 Simulation of Forming and Impact Chapter 7: Contact and Friction,” Waterloo, Ontario, Canada.

[59] R. George, “Hot Forming of Boron Steels with Tailored Mechanical Properties,” Master’s thesis, University of Waterloo, Waterloo, Ontario, Canada, 2011.

[60] A. B. Shapiro, “Using LS-Dyna for Hot Stamping,” in *DYNAmore GmbH*, Livermore, CA, USA, 2009, p. 9.

[61] S. DiCecco, M. Di Ciano, C. Butcher, and M. Worswick, “Numerical and experimental investigation of the formability of AA6013-T6,” *J. Phys.: Conf. Ser.*, vol. 896, p. 012114, Sep. 2017, doi: 10.1088/1742-6596/896/1/012114.

[62] J. Min, T. B. Stoughton, J. E. Carsley, and J. Lin, “An improved curvature method of detecting the onset of localized necking in Marciniak tests and its extension to Nakazima tests,” *International Journal of Mechanical Sciences*, vol. 123, pp. 238–252, Apr. 2017, doi: 10.1016/j.ijmecsci.2017.02.011.

[63] J. Noder and C. Butcher, “NOVEL INSTABILITY FRAMEWORK TO PREDICT LOCAL FORMABILITY IN 3RD GEN AHSS B-PILLAR TECHNOLOGY DEMONSTRATOR,” presented at the Great Design in Steel 2022, May 18, 2022.

Appendix A

The VHT® Flameproof aerosol paint, when sprayed directly onto the test sample, created a fine mist of paint, resulting in speckles that were too fine for the DIC system to track. The direct fire tactic was modified with a longer engagement range to allow paint drops to spread apart in-flight. When the nozzle trigger was slightly pressed, larger paint drops formed at the start of a burst and travelled a shorter distance than faster/lighter paint drops. To increase the fraction of larger paint drops landing on target, the nozzle was angled at around 45° relative to the test sample surface, shown in Figure 94. An indirect fire tactic, shown in Figure 95, was also considered where the line of fire was horizontal relative to the sample surface. This method produced acceptable results in Nakazima dome tests where all geometries deformed in plane strain.

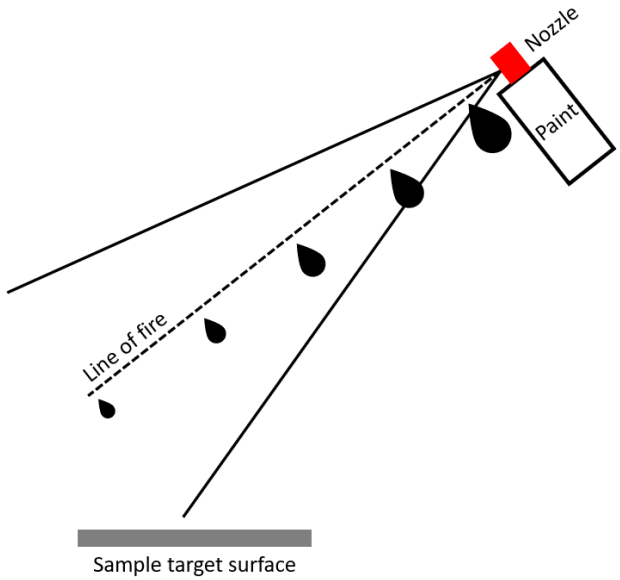

Figure 94: Direct fire tactic used for speckling Nakazima test samples. The line of fire is angled about 45° to the sample target surface.

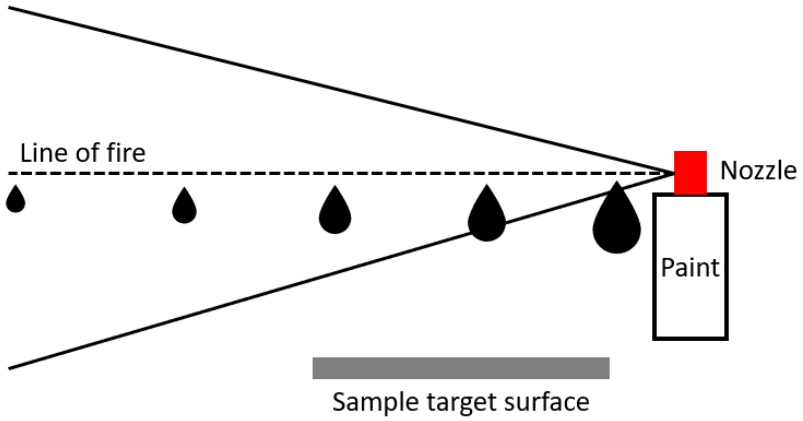

Figure 95: Indirect fire tactic with line of fire parallel to the sample target surface

On the other hand, this aerosol spray method caused excessive data noise in uniaxial and equibiaxial deformation modes during the Marciniak and Hybrid tests. The speckles were still too fine for the DIC cameras to track accurately, since small surface cracks in the pre-alloyed Al-Si coating formed near the necking location at the center of the blank at large strain levels. The cracks had a white appearance caused by the base metal's reflection which confounded the DIC software into identifying them as white speckles. This error caused the noise magnitude to be so high that it matched the magnitude of the recorded data. Therefore, the speckle size must be further increased to prevent this misidentification with surface cracks.

Several attempts were made to resolve the speckle size issue. By decreasing the engagement range in the indirect fire tactic, more large speckles reached the target surface due to their higher inertia and lower flight speed. Nonetheless, excessively large blobs of paint landing on target also became frequent and unavoidable. When a large blob of paint landed on a critical area such as the center of the sample, DIC data in this affected area became null, and the sample became unusable. This was usually not an issue with room temperature aerosol paint. The difference in viscosity and

presence of solid particles in the VHT Fireproof paint caused the fluid flow behavior to be different and unsuitable for speckling high temperature samples by aerosol spray.

Since the VHT Fireproof paint could form an even layer of paint using the direct fire tactic, a perforated stencil with 0.6 mm diameter holes, shown in Figure 96, was placed on the sample gage section to project the stencil pattern onto the sample. Due to the diverging spray pattern from the nozzle, the painted speckles using the stencil were slightly larger than the hole diameter. These speckles were large enough not to be confounded with surface cracks and produced usable data. However, the stencil holes became clogged with paint after each application. They were difficult to unclog despite several cleaning methods such as soaking in a solvent for a prolonged period and brushing with stiff bristles. Since the stencil could not be produced in large quantity, this method was deemed inefficient and unsuitable for the large quantity of samples.

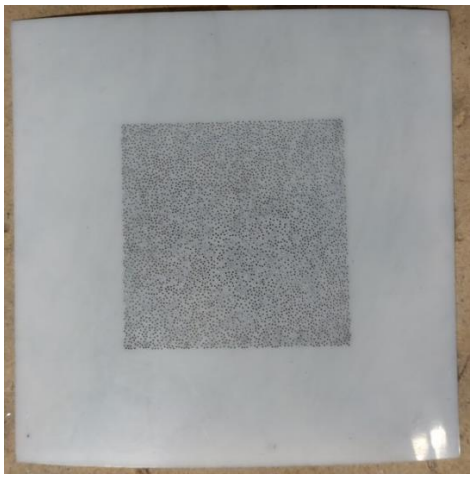

Figure 96: Speckling stencil with 0.6 mm diameter holes

A gravity fed Iwata Eclipse airbrush was also considered which could produce the desired speckle size with the right combination of nozzle aperture size and paint feed rate. A large nozzle aperture with a low paint feed rate created large speckles and evenly distributed them across the target. However, the VHT Fireproof paint was not optimized for use in an airbrush even if mixed with an enamel paint thinner to decrease its viscosity. In addition, solid particles in the paint jammed the airbrush gun after just a few bursts. Therefore, the airbrush was not used further with the VHT Fireproof paint.

A rubber stamp with a dot size of 0.66 mm made by Correlated Solutions, shown in Figure 97, was intended for 1 MP (1024 pixels) cameras such as the ones used for the current DIC measurements. Convex rods covered the surface of the stamp. To speckle the sample, paint was first thoroughly applied onto paper towels. Then, the rubber stamp was pressed onto the paint-soaked towels to coat only the tips of the convex rods. Finally, the stamp was pressed firmly onto the sample's gage section to create the desired speckles. This tactical speckling process was repeated three times per sample with a different orientation per application to diversify the location of the speckles across the target surface. The resulting speckles were large enough to avoid being confounded with surface cracks and were repeatable across all sample geometries.

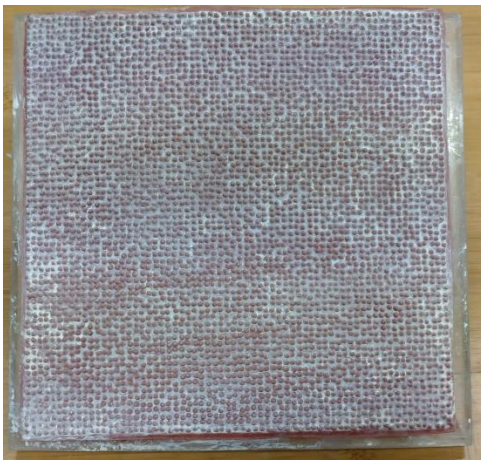

Figure 97: Tactical speckling rubber stamp with a dot size of 0.66 mm made by Correlated Solutions

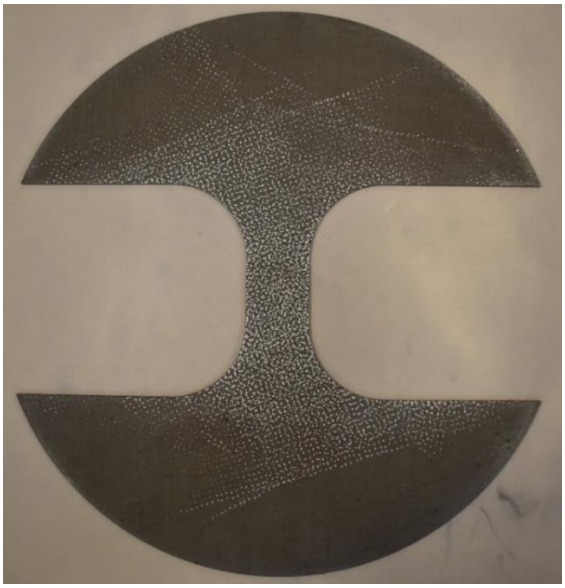

Figure 98: Pre-alloyed PHS1800 sample speckled using a rubber stamp with a dot size of 0.66 mm.

The large speckle size of the stamp required a larger subset size of 37. This in turn caused a larger step size of 9. To maintain an acceptable level of noise without excessive compromise on the resolution of measurements, the filter size was set to 11.

Appendix B - Recommendations

Friction characterization of Al-Si coated PHS under hot stamping conditions.

- A friction test method should be developed to prevent repetitive sliding across the same sample area (as in the TCT test).
- The developed friction test method should feature a large contact area to prevent excessive ploughing.
- The developed friction test method should enable accurate control of the sample transfer time from the furnace to the friction test platform.
- The developed friction test method should not require the sample to be a continuous strip of sheet metal. This would better represent the industrial transfer process by eliminating thermal conduction within the sample between the furnace and the friction test platform.

Formability characterization of Al-Si coated PHS under hot stamping conditions:

- An improved method for high temperature DIC speckles should be developed to minimize data noise and to enhance strain field resolution. The current high-temperature paint speckles cannot be accurately controlled by directly spraying from the aerosol paint can, so a rubber stamp with constant speckle size had to be used on the sample surface.
- A smaller speckle size should be combined with the existing large speckles to create speckle variation and to improve resolution of the strain field.